To the Graduate Council:

I am submitting herewith a dissertation written by Nathan Joseph Crawford entitled "Factors Affecting the Phase Separation of Liquid Crystals from Acrylate-based Polymer Matrices." I have examined the final paper copy of this dissertation for form and content and recommend that it be accepted in partial fulfillment of the requirements for the Doctor of Philosophy, with a major in Chemistry.

Mark D. Dadmun, Major Professor

We have read this dissertation
and recommend its acceptance:

Bin Zhao

Bin Hu

Peter Zhang

Accepted for the Council:

Vice Chancellor and Dean of
Graduate Studies

Thesis
2005b
.C73

FACTORS AFFECTING THE PHASE SEPARATION OF LIQUID CRYSTALS FROM ACRYLATE-BASED POLYMER MATRICES

A Dissertation

Presented for the

Doctor of Philosophy Degree

University of Tennessee, Knoxville

Nathan Joseph Crawford

August 2005

ACKNOWLEDGEMENTS

I wish to thank Professor Mark D. Dadmun for affording me the opportunity to work on a project that has broadened and deepened my understanding of science and technology. I also thank my committee members, Professors Bin Zhao, Bin Hu, and Peter Zhang, for their patience and input. I would also like to thank my colleagues, Charles O'Brien, Michael Arlen, Eric Eastwood, Gary Lynn, Kevin Rice, Steve Wargacki, Scott Fontana, Asif Rasheed, and Sudesh Kamath, for their advice and friendship. Special thanks are also given to my family and friends who have given me financial as well as moral support. Above all, I must thank my wife, Katrina. Without her steadfast love, emotional and financial support, I could never have accomplished this work.

ABSTRACT

The work presented in this dissertation covers the study of phase separation of small-molecule liquid crystals (LC's) from acrylate-based polymer matrices. These materials are used in the construction of polymer dispersed liquid crystals, or PDLC's, an emerging technology with applications ranging from privacy windows to photonic materials.

The first part of this study involves the determination of the effect of increasing polymer molecular weight on the solubility of the LC 4'-octyl-4-biphenyl carbonitrile, or 8CB, in poly(methyl methacrylate), or PMMA. Optical microscopy is used to determine the equilibrium phase diagrams for blends of 8CB and PMMA with weight-average polymer molecular weights ranging from 23,000-600,000 g/mol, and differential scanning calorimetry, DSC, is used to determine the fraction of 8CB that remains trapped in the polymer matrix, or the solubility limit of 8CB. Phase diagrams show what appears to be an upper limit to the effect of polymer molecular weight. The effect of polymer molecular weight on the phase behavior is quantified by extraction of the Flory-Huggins interaction parameter from fits of the microscopy data to the Flory-Huggins theory for polymer solutions. The solubility limit data also show a limit to the effect of polymer molecular weight, and when compared to solubility limit data from previous studies that use different polymer matrices, the data supports the independence of the solubility limit from polymer composition.

The second part of this work changes the emphasis of the study from the effect of polymer molecular weight to fluorination of the polymer matrix. Monomers of 2,2,2-

trifluoro ethyl methacrylate, TFEMA, and methyl methacrylate , MMA, are polymerized by atom transfer radical polymerization, or ATRP, to form copolymers with 8, 19, 25, 44, and 70% TFEMA content. The copolymers are blended with 8CB, and phase diagrams of the blends are determined by optical microscopy. As the TFEMA content of the copolymer increases, a corresponding increase in the region of immiscibility of 8CB is observed. In order to quantify the effect of increasing TFEMA content, the Flory-Huggins interaction parameters for each blend are determined from the fitting procedure used in the previous section.

The final part of this thesis employs time-resolved light scattering to study the phase separation kinetics of the LC blend E7 from a polymer matrix formed by polymerization-induced phase separation, or PIPS. The light scattering experiments start with syrups that consist of two different E7 fractions, 40 and 50% by mass. The syrups are cured by a green diode laser under four different cure beam intensities. The scattering profiles for the lowest cure beam intensity exhibit behavior that supports phase separation by a spinodal decomposition mechanism.

TABLE OF CONTENTS

Chapter **Page**

1 Polymer Dispersed Liquid Crystals: Introduction and Experimental Strategies.....1

1.1 Introduction.....1

1.2 Liquid Crystal Primer.....4

1.3 Matrix Construction Techniques.....10

1.4 Description of PDLC Phase Behavior.....14

1.5 Goals and Experimental Strategies.....34

2 Experimental Techniques.....38

2.1 Microscopy.....38

2.2 Differential Scanning Calorimetry.....43

2.3 Time-resolved Light Scattering.....48

2.4 Polymerizations.....54

3 Polymer Molecular Weight Effects on the Solubility of 8CB in PMMA Matrices.....62

3.1 Introduction.....62

3.2 Experimental.....64

3.3 Results.....75

3.4 Discussion.....86

3.5 Conclusions.....88

4 The Consequence of Matrix Fluorination on Liquid Crystal Solubility in Polymer Dispersed Liquid Crystals.....90

4.1 Introduction.....90

4.2 Experimental.....92

4.3 Results and Discussion.....99

4.4 Conclusions.....107

5 Time-resolved Light Scattering of Phase Separation in PDLC's Formed by Photo-polymerization Induced Phase Separation.....108

5.1 Introduction.....108

5.2 Experimental.....110

5.3 Results and Discussion.....114

5.4 Conclusions.....148

6 Conclusions and Future Work.....150

Bibliography.....154

Vita.....161

LIST OF TABLES

Table **Page**

2.1 ATRP results for P(MMA-co-TFEMA) synthesis, * copolymer synthesized by C. P. O'Brien.....61

3.1 List of sources, the number and weight average molecular weights and polydispersities (PDI) for the poly(methyl methacrylate) polymers used in this study.....65

3.2 Values for the polymer segment lengths, N_2, critical fraction, ϕ_c, and the critical interaction parameter, χ_c, extracted from the microscopy data; Effective segment size for N_2 determination ca. 10,000 g/mol.....78

5.1 Apparent diffusion coefficients, D_{app}, obtained from the analysis of the early stages of spinodal decomposition. Maximum scattering vectors, q_m, calculated from D_{app}, compared to experimental results.....124

LIST OF FIGURES

Figure **Page**

1.1 PDLC device in the "on" and "off" states.....3

1.2 Liquid crystal examples a. The LC molecule 8CB, b. the nematic phase, c. the smectic phase.....6

1.3 Stages of PIPS, a. Initial stage, b. Intermediate stage, c. Final stage.....12

1.4 A simple upper critical solution temperature, or UCST, phase diagram....15

1.5 Representation of the lattice model used by Flory-Huggins theory: A polymer chain (black, connected circles) surrounded by solvent (white circles).....17

1.6 Representation of the mixing process as pure components, Pure 1 and Pure 2, change from pure (1,1) and (2,2) contacts to (1,2) contacts upon mixing.....23

1.7 The variation of the free energy change, ΔG_m, with solution composition, φ, constant temperature.....25

1.8 UCST phase diagram a. Binodal line, b. Spinodal line, c. Critical point...27

1.9 Illustration of thermal quench in TIPS: A, completely miscible, B, shallow quench, C deep quench.....30

1.10 Visualization of PIPS process: A, the blend composition, changing phase diagrams with increasing polymerization times, t1 – t3.....33

2.1 Schematic of an optical microscope, a. light source, b. condenser annulus, c. polarizer, d. sample, e. phase plate, f. analyzer, g. observer.....39

2.2 Schematic of a heat flux DSC. S is the sample pan, and R is the reference pan.....45

2.3 Representation of a DSC thermograph, a. glass transition, b. endothermic event, c. exothermic event.....46

2.4 Representation of the scattering of light during a time-resolved light scattering experiment.....50

2.5 Schematic of the time-resolved light scattering instrument used in the measurement of the phase separation kinetics studies that occur during PIPS.....52

2.6 Reaction scheme for atom transfer radical addition, or ATRA.....55

2.7 Polymerization via atom transfer radical polymerization, or ATRP.....57

2.8 Initiation and propagation steps for poly(methyl methacrylate) as synthesized by ATRP.....58

3.1 Illustration of the first derivative of the Flory-Huggins free energy versus LC fraction that is used to determine theoretical coexistence curves. The two fractions, denoted by the primes, are the LC-poor and rich compositions at equilibrium.....69

3.2 Typical phase diagram for PMMA/8CB blends, PMMA M_w = 90,000 g/mol; (◆) Smectic to nematic transition, (■) Nematic to isotropic transition, (▲) Isotropic mixing transition.....76

3.3 Microscopy data for isotropic mixing of PMMA with 8CB for all PMMA weight average molecular weights, (◆, lower) 32,200 g/mol, (●) 67,200 g/mol, (◆, upper) 90,000 g/mol, (■) 335,000 g/mol, (▲) 600,000 g/mol.....77

3.4 Initial fits of microscopy data for the isotropic mixing transition to F-H; χ has no molecular weight dependence; (◆, lower) 32,200 g/mol, (●) 67,200 g/mol, (◆, upper) 90,000 g/mol, (■) 335,000 g/mol, (▲) 600,000 g/mol.....79

3.5 Fits of microscopy data for the isotropic mixing transitions to F-H, where χ scales with M_w; (◆, lower) 32,200 g/mol, (●) 67,200 g/mol, (◆, upper) 90,000 g/mol, (■) 335,000 g/mol, (▲) 600,000 g/mol.....80

3.6 Comparison of the scaling of extracted χ values at 60°C to mean-field prediction of $\chi \sim M_w^{-0.5}$.....82

3.7 Typical set of DSC thermograms for 90,000 g/mol PMMA blend arranged in order of decreasing LC content. Portion in brackets is the nematic-isotropic transition of 8CB. Integration for each blend is the value on the far right.....83

3.8 Typical DSC results for ΔH_{N-I} used to extrapolate β, PMMA M_w = 90,000 g/mol; x-intercept yields β, the solubility limit.....84

3.9 Comparison of solubility limits; (◆) from Benmouna et al for PS/8CB blends, (■) solubility limits from this study.....85

4.1 Chemical structures of monomers used in atom transfer radical polymerizations, (left to right) methyl methacrylate (MMA) and (2,2,2) trifluoroethyl methacrylate (TFEMA).....93

4.2 Typical phase diagram for 8CB/copolymer blends (8.3% TFEMA); (▲) Smectic to nematic transition, (◆) Nematic to isotropic transition, (■) Isotropic mixing transition.....100

4.3 Comparison of isotropic mixing transitions for all 8CB/copolymer blends; (◆) 8.3 % TFEMA, (■) 19% TFEMA, (▲) 25% TFEMA, (∗) 44% TFEMA, (●) 70% TFEMA.....101

4.4 Interaction parameters that result in the best fit to the microscopy results, (◆)$\chi_{8CB\text{-}TFEMA}$, (▲)$\chi_{MMA\text{-}TFEMA}$, (■)$\chi_{8CB\text{-}MMA}$.....103

4.5 Isotropic mixing data with fits (solid and dashed lines) to Flory-Huggins theory.....105

4.6 The total interaction parameters that are based on the Flory-Huggins fits to microscopy data plotted versus mole fraction of TFEMA in the copolymer calculated at 80°C.....106

5.1 Components of syrups used to form PDLC's; a.) N-vinyl pyrrolidone, b.) N-phenyl glycine, c.) Rose Bengal acetate ester, d.) dipentaeryhtritol dihydroxy pentaacrylate.....111

5.2 Reaction scheme for the photoinitiation of the acrylate monomer through the electron transfer from excited Rose Bengal (RB*) to the co-initiator N-phenyl glycine.....112

5.3 Scattering profiles for blends cured at 0.069 mW/cm2. a) 40% E7 30-915s; (b) 40% E7 1020-3245s; (c) 50% E7 7-1165s; (d) 50% E7 1519-4038s.....115

5.4 Plot of interdomain distance versus time for both LC compositions, (◆) 40% E7, (■) 50% E7.....119

5.5 Semilogarithmic plot of intensity versus time for different scattering vectors. Slopes of data in highlighted section are used to determine the growth rate function, R(q).....121

5.6 Growth rate divided by the square of the scattering vector versus the square of the scattering vector, (◆) 40% E7 and (■) 50% E7. Y-intercept gives the apparent mutual diffusion coefficient, D_{app}.....123

5.7 HRSEM micrographs of films from 50% E7 sample cured at 0.069mW/cm^2 for over 2hours; a) 10μm; (b) 1μm magnification.....126

5.8 Scattering profiles for PDLC syrups cured at 0.14 mW/cm^2. a) 40% E7 14-164s; b) 40% E7 264-316s; c) 50% E7 25-95s; d) 50% E7 105-215s...128

5.9 Scattering profiles for PDLC syrups cured at 0.214 mW/cm^2. a) 40% E7 14-214s; b) 40% E7 314-618s; c) 50% E7 58-103s.....130

5.10 Scattering profiles for PDLC syrups cured at 0.693 mW/cm^2. a) 40% E7 11-301s; b) 50% E7 15-405s.....132

5.11 Scattering profiles for fully cured 50% E7 PDLC films before LC removal.....136

5.12 HRSEM image of PDLC film cured at 0.11 mW/cm^2 (LC has been removed), a.)scale bar 10 μm b.) FFT of image in (a.), indicative of a random network c.) HRSEM image of PDLC film depicted in Figure 5.11 at 1μm length scale d.) Typical plot profile of image in (c.), average size of the voids approximately 145nm.....137

5.13 HRSEM image of PDLC film cured at 0.29 mW/cm^2 (LC has been removed), a.scale bar 10 μm b. FFT of image in (a.), indicative of a random network. c. HRSEM image of PDLC film depicted in Figure 5.12 at 1μm length scale d.) Typical plot profile of image in (c.), average size of the voids approximately 192 nm.....139

5.14 Debye-Bueche analysis of scattering data, (◆) 40% E7 I(0), (▲) 50% E7 I(0), (◇) 40% E7 correlation length, (△) 50% E7 correlation length. a. 0.14 mW/cm^2; b. 0.214 mW/cm^2; c) 0.693 mW/cm^2.....143

LIST OF ABBREVIATIONS

8CB	Liquid crystal 4′-octyl-4-biphenyl carbonitrile
ATRA	Atom Transfer Radical Addition
ATRP	Atom Transfer Radical Polymerization
DB	Debye-Bueche
DSC	Differential Scanning Calorimetry
E7	Eutectic liquid crystal mixture
FFT	Fast Fourier Transform
F-H	Flory-Huggins
GPC	Gel Permeation Chromatography
^{1}H-NMR	Proton Nuclear Magnetic Resonance
HRSEM	High-resolution Scanning Electron Microscopy
LC	Liquid Crystal
LCD	Liquid Crystal Display
MMA	Methyl methacrylate
M-S	Maier-Saupe
OM	Optical Microscopy
OZ	Ornstein-Zernicke
PDI	Polydispersity Index
PDLC	Polymer Dispersed Liquid Crystal
PDSC	Phenoxy benzene-4,4′-disulfonyl chloride
PIPS	Polymerization Induced Phase Separation
PMMA	Poly(methyl methacrylate)
P(MMA-co-TFEMA)	Poly(methyl methacrylate-co-2,2,2-trifluoroethyl methacrylate)
SEM	Scanning Electron Microscopy
SIPS	Solvent Induced Phase Separation
TFEMA	2,2,2-trifluoroethyl methacrylate
TIPS	Temperature Induced Phase Separation
TRLS	Time-resolved Light Scattering

CHAPTER 1

Polymer Dispersed Liquid Crystals: Introduction and Experimental Strategies

1.1

Introduction

As telecommunication and computing have advanced the need for new optically active materials remains an important concern, especially for options that minimize power consumption as well as weight. Liquid crystals (LC's) have offered a successful option to this dilemma in recent years. The liquid crystal display or LCD, for example, has become ubiquitous in the manufacture of such mobile devices as personal digital assistants, notebook computers, and flat-panel televisions. Indeed the use of LC's in the displays is projected to become a $7 billion industry by 2005.[1,2]

The use of LC's, however, is not limited to use in displays. In the past decade one class of LC/polymer composites has shown much promise in expanding the role of these small molecules to include variable light valves, privacy windows, or even laser resonators.[3-7] These composites, called polymer-dispersed liquid crystals or PDLC's, consist of LC droplets within a polymer matrix.[3,4] The matrix can be made from either linear polymer chains or a cross-linked gel. In both cases the polymer acts as an optically isotropic medium while the birefringent LC makes the composite optically active. The polymer matrix by its flexibility gives the PDLC mechanical strength.[3-5] Additionally the use of a polymer matrix means the PDLC can be easily coated as a film onto a conducting substrate for the manufacture of electro-optical devices.

The basic operation, as shown in Figure 1, begins with the scattering or "off" state. At this point the alignment of the LC varies from droplet to droplet.[3-5] The

differing alignments mean the refractive index varies from one droplet to the next and cause scattering of light propagating through the film.[3,4] When a voltage is applied, the "on" state, the LC's change their alignment to the direction of the field, the refractive index of the LC matches that of the matrix, and the PDLC becomes transparent.

When considering the basic operation of a PDLC, questions arise as to what factors would affect the performance of the device.[3,6,8] The first question to address is one of refractive index. The "on" state of the PDLC requires a polymer matrix that has a refractive index as close to that of the aligned LC as possible, as mismatches between the two leads to such problems as haziness. From Figure 1.1 one can also see a need to control LC solubility in the matrix.[3,6] If the LC remains dissolved in the matrix, it will not be available to form droplets for efficient scattering. Additionally, loss of LC to the matrix drives up the manufacturing cost due to waste.[3] Another question to be answered is the interaction between the LC molecules and the droplet walls formed by the matrix. Since LC molecules possess some degree of polarity, alignment of the LC to the walls of the droplet can be relatively strong.[9,10] This interaction, called anchoring, leads to increases in the voltage needed to change alignment as well as a slowing of the response time of the LC to the applied field. Lastly, the technique used to construct the PDLC controls the size, shape, and distribution of the droplets may also affect the performance of device.[3,4] Irregular droplets can cause undesirable defects in the LC phase while droplets that are too large cause increased switching times. In the case of a distribution of droplet sizes a broad size distribution causes irregularities in scattering, an unwanted effect in PDLC's such as holographic diffraction gratings.[3-6]

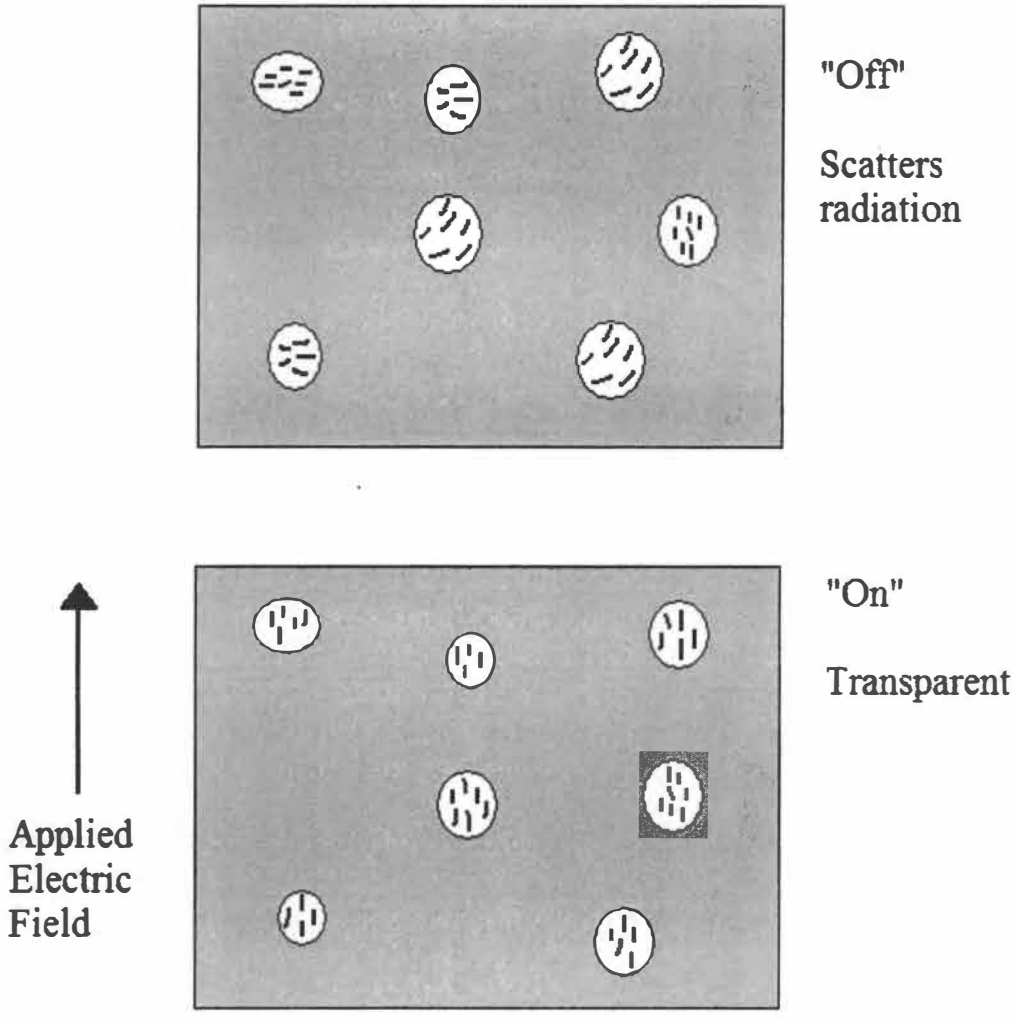


Figure 1.1 PDLC device in the "on" and "off" states

1.2

Liquid Crystal Primer

The study of liquid crystals (LC's) has filled many texts over the years and could stand alone as a field of study in condensed matter physics. Therefore, this section is written to provide the reader with some important background pertaining to the properties and theoretical descriptions of LC's relevant to this work.

Although others like Otto Lehmann[11] had previously observed similar phase behavior in other substances, the discovery of liquid crystals is credited to the Austrian botanist Friedrich Reinitzer in 1888. Reinitzer was working to determine the role of cholesterol in plants when he observed what appeared to be two different melting points in a cholesterol-like substance. The discovery of this behavior led to the development of new, synthetic liquid crystals as well as insights into the structural properties that cause the mesomorphic behavior of these compounds.

As time passed, the unique phase behavior of liquid crystals found practical applications. In the late 1960's[11] researchers used liquid crystals to make a display that changed from opaque to transparent with the application of an electric field. The technology that came from this work laid the foundation for future developments that have given the world the modern liquid crystal display, or LCD.

The difference between the liquid crystalline phase and the normal liquid phase is one of order. In a normal isotropic fluid there are no long-range correlations[10] between the constituent molecules. In contrast to the liquid phase is that of a crystal where atoms or molecules have 3-D positional and orientational order.[3,10] Liquid crystalline phases

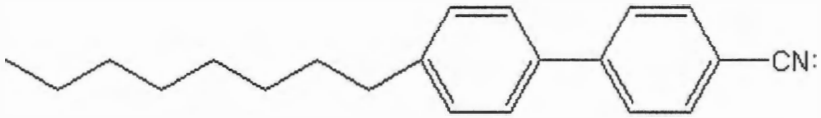
fall between these two extremes. They contain orientational order as well as varying degrees of positional order but still retain the ability to diffuse within a given mesophase.

Liquid crystal molecules, such as 4′-octyl-4-biphenyl carbonitrile (8CB) shown in Figure 1.2, 2a., are often rod-shaped organic compounds consisting of a rigid core, polar "head", and non-polar "tail". The core often consists of 2 or more 1,4-disubstituted phenyl rings that impart an anisotropic shape to the molecule. The "head" is usually a dipolar moiety [3] such as the nitrile group found in 8CB, and the flexible hydrocarbon "tail" serves as a non-polar extension of the core.

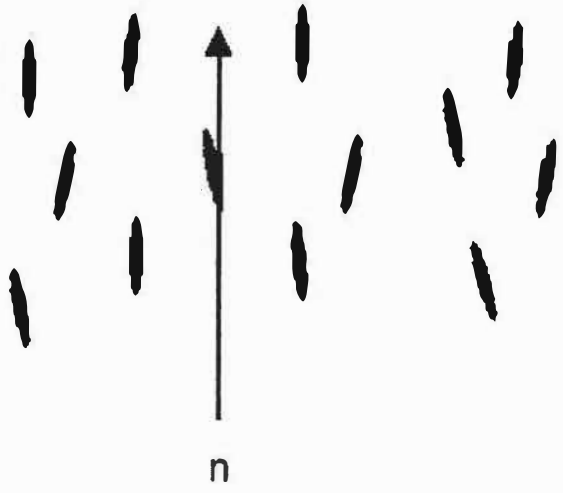
The anisotropic structure as well as the polarity of the LC molecule affects both the intermolecular correlations and the macroscopic properties of the liquid crystalline phase. The orientation of the LC molecules, whether in the nematic or smectic phase, In addition to affecting the arrangement of the LC molecules, the molecular structure is also responsible for the unique optical properties. For example, when polarized light passes through a LC mesophase, the light undergoes a change in polarization state. The reason for this change is that the light experiences two different refractive indexes, one along and one perpendicular to the long-axis of the molecule. As a result, the LC is said to exhibit double refraction or, more commonly, birefringence.

Due to the numerous mesophases exhibited by LC's, the discussion of their phase behavior is limited to the two encountered in this thesis, the nematic and smectic. A schematic representation of the two phases can be found in 2 b. and c. The nematic phase is characterized by a lack of positional order, but the LC molecules are aligned along a vector called the director, denoted n. The smectic phase, on the other hand, shows both

1.2 a.



1.2 b.



1.2 c.

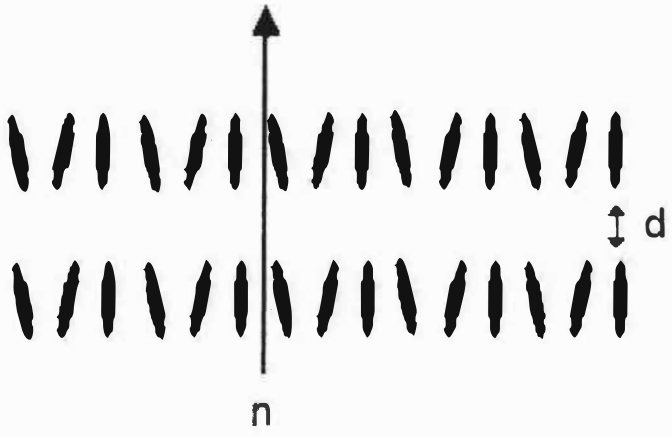


Figure 1.2 Liquid crystal examples a. the LC molecule 8CB, b. the nematic phase, c. the smectic phase

directional and positional order with the LC molecules forming oriented "sheets" separated by a distance, d.

In either phase an important value used in the thermodynamic descriptions is the degree of order in the system given by the order parameter[3,9,10], S. However, all of the LC molecules within a given mesophase, as shown in the figure, are not exactly parallel to the director but lie at an angle, θ, to n. The determination of S, therefore, must be able to account for the average distribution of θ for millions of molecules. A simple method to define S is to take the average of a function that describes the angle of the LC molecules. This relationship is given in equation (E 1.1) below. This equation, though,

$$S = \langle 3/2 \cos^2\theta - 1/2 \rangle \qquad \text{(E 1.1)}$$

is too simplistic and is more accurately expressed in terms of the average of the integration over both the orientational distribution function[3,9,10], $f(\theta)$, as well as the azimuthal angle, ϕ, that is orthogonal to the director for all LC molecules. The new expression for S is given in equation (E 1.2). From this equation we can see that

$$S = \int_0^{\pi} f(\theta) (3/2 \cos^2\theta - 1/2) \sin\theta d\theta \int_0^{2\pi} d\phi \qquad \text{(E 1.2)}$$

perfect orientation of every LC molecule relative to the director, $\theta = 0$, results in $S = 1$.[9] When the orientation is completely random, as in the isotropic phase, the distribution function, $f(\theta)$, becomes constant due to the equal probability of the LC molecules pointing in all directions. Since $f(\theta)$ is now a constant, equation (E 1.2) becomes zero. For intermediate values of θ, between 0 and 90 degrees, the LC phase possesses less orientation, and the order parameter gives values less than one.[3,9,10]

To apply the definition of the order parameter given in (E 1.2) to the behavior of LC molecules in the nematic and smectic phases, we need a means to predict the change in order parameter with temperature. Different methods have been employed to accomplish this task, but one approach, the Maier-Saupe theory,[3,9,10] has proven to be a particularly practical starting point. The heart of Maier-Saupe theory, or M-S theory, is a mean-field thermodynamic description[3,9,10] of the simplest anisotropic phase, the nematic. In other words, the theory requires a thermodynamic potential for only a single LC molecule in the nematic phase that is then used to determine the average potential for all of the LC molecules that are present.

In order to simplify the derivations for the statistical relationships, M-S theory makes several assumptions.[9,10] The first step is assuming no permanent dipoles within a given molecule. This condition means that the interactions between molecules are predominantly dispersion forces. Secondly, the LC's are assumed to possess uniaxial symmetry[3,9,10] so the potential energy between pairs depends on the angular dependence of the pairs long axes. Lastly, the orientational order parameter is introduced as a linear component.[9] These assumptions are the basis of Maier-Saupe expression for the potential energy,U, given in equation (E 1.3) for a LC molecule, i. Here U is a function of the

$$U_i(\theta_i) = -(A/V^2)\, S\, (3/2 \cos^2 \theta_i - 1/2) \qquad \text{(E 1.3)}$$

angle θ between of the LC molecule to the director, A is a temperature independent constant, V is the volume, and S is the orientaional order parameter. The first assumption leads to the inverse square volume term because the forces between the LC molecule and its neighbors vary as distance to the minus sixth.[10] The last term in (E 1.3) comes from

the second condition for the axial angular dependence while the order parameter, S, embodies the last of the assumptions.[9,10]

Once the potential is established a probability function, given in equation (E 1.4), can be used to determine the temperature dependence of S through the Boltzmann constant, k_B, and temperature, T. The partition function, Z,[3,10] is expressed by equation (E 1.5)

$$P(\theta) = 1/Z\, e^{-U_i(\theta_i)/k_B T} \qquad \text{(E 1.4)}$$

$$Z = \int_0^{\pi} e^{-U_i(\theta_i)/k_B T} \sin\theta_i \, d\theta_i \int_0^{2\pi} d\phi_i \qquad \text{(E 1.5)}$$

The probability function in (E 1.4) replaces the function $f(\theta)$ found in (E 1.2), and the order parameter becomes the equation (E 1.6).

$$S = 1/Z \left\{\int_0^{\pi} (3/2 \cos^2\theta - 1/2)\, e^{-U_i(\theta_i)/k_B T} \sin\theta d\theta \int_0^{2\pi} d\phi\right\} \qquad \text{(E 1.6)}$$

In describing the smectic phase M-S theory is employed again this time with important additions made by McMillan.[3] Since smectic LC's form sheets separated by a distance, d, a density amplitude in the form of another order parameter, σ, is introduced in the potential energy expression by the relationship found in equation (E 1.4) where z_i gives the position of the molecule, i. Another factor, α, accounts for the strength

$$\sigma = \langle \cos(2\pi z_i/d)(3/2 \cos^2\theta_i - 1/2)\rangle \qquad \text{(E 1.7)}$$

of short-range intermolecular interactions.[3,10] When these factors are incorporated into the potential energy, $U(\theta)$ becomes equation (E 1.8). Derivation of the probability

$$U_i(\theta_i, z_i) = -U_0[S + \alpha\sigma \cos(2\pi z_i/d)]\,(3/2 \cos^2\theta_i - 1/2) \qquad \text{(E 1.8)}$$

and partition functions proceeds just as in the nematic phase.

1.3

Matrix Construction Techniques

The polymer used as the matrix material must meet a variety of criteria to ensure an effective PDLC. The first, as mentioned earlier, is finding a polymer with a suitable refractive index.[3,4,8] Typically, the refractive index of the matrix should be low enough to be transparent when the proposed device is "on". Therefore, polymers with a tendency towards crystallization, i.e. poly(ethylene),[12] are avoided since the crystalline portions of would scatter light regardless of LC orientation. Another variable in PDLC construction is the solubility of the LC in the matrix. In this case there is a two-fold reason why the choice of polymer should give the lowest possible miscibility. For one, the scattering efficiency of the PDLC is greatly reduced if the LC is prevented from forming LC-rich domains, and second is the increased cost from waste.[3] Lastly, the chemical composition of the polymer should be chosen so as not to react with the liquid crystals, as well as to limit interactions between the LC molecules and the droplet walls (i.e. anchoring) that could effect the response of the LC to electric fields.

Construction of PDLC's follows two different strategies, emulsion methods and phase-separation methods. Emulsion methods, used in Fergason's original patents,[3,4,13] involve emulsifying the LC with the polymer matrix material in water. The emulsion is coated onto a conducting substrate and allowed to dry. This technique is not often employed to form devices due to film shrinkage from drying as the changes in droplet size and shape causes undesirable changes in the performance of the PDLC.[3,4,5]

Phase-separation methods can be separated into three different classes to be discussed separately. The first class of phase-separation methods is called solvent-

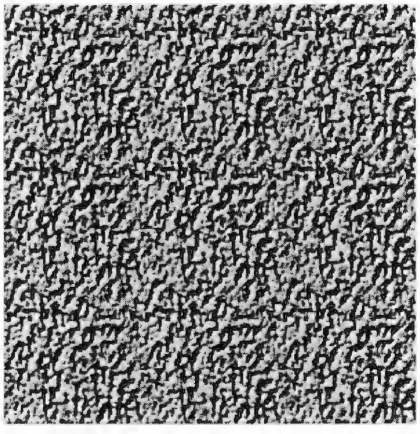
induced phase separation or SIPS.[3,4] PDLC preparation by SIPS proceeds by dissolving the polymer and LC in an appropriate solvent, casting the mixture on the desired substrate, and removing the solvent by air-drying or vacuum. This technique, although very simple to perform, suffers from the same disadvantages as the emulsion methods.

Temperature-induced phase separation, TIPS,[3,4] is usually accomplished first by forming a film using SIPS. The film is then heated until the two components become completely mixed. Subsequent cooling of the film causes the LC to phase separate from the polymer matrix. The phase separation in this case depends on blend composition, polymer molecular weight, and the depth of the temperature quench used. The advantage of this technique over SIPS alone is the ability to control droplet morphology by adjusting the cooling rate. However, constructing PDLC's in this way limits the temperatures at which they can be used because droplet shrinkage upon cooling distorts the droplet shape.[3,4,6] This droplet distortion can adversely effect the switching times and voltages of the LC.

The last of the phase separation techniques has become the most popular PDLC construction method, see Figure 1.3 a-c. Polymerization-induced phase separation, or PIPS,[3-6] begins by blending the LC with un-reacted monomer and initiator, if required, to form a homogeneous syrup 1.3 a. When the polymerization begins, the increasing size of the polymer chains become the driving force behind phase separation. The blend during these intermediate times, as illustrated in 3b, begins to form domains rich in either polymer or LC. The final stage of PIPS, 3c, sees the separation of the LC into droplets.

1.3 a.

1.3 b.



1.3 c.

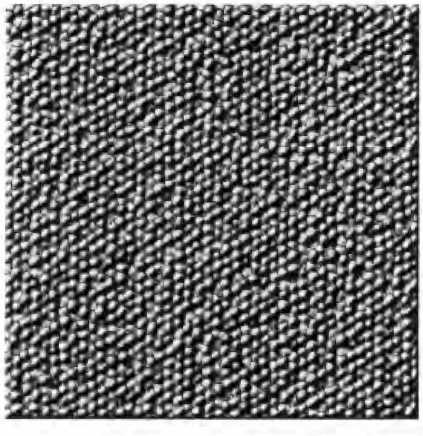


Figure 1.3 Stages of PIPS, a. Initial stage, b. Intermediate stage, c. Final stage

The final size, shape, and distribution of the LC droplets formed during PIPS vary widely depending on initial conditions as well as the polymerization technique. Initial conditions such as temperature or LC content have been shown to significantly affect the phase separation of the LC.[3-6] These variables not only define the starting point of the blend phase behavior before matrix formation but can also affect polymerization rates. The polymerization techniques used in PIPS take advantage of many different reaction chemistries. However, the polymerization schemes can be classified into two main categories, chain and step-growth polymerizations.[13]

For chain polymerizations the reactions require initiators to react with a monomer to give reactive centers. The reactive centers react with other monomers in a propagation process that builds the polymer matrix. The highly reactive propagating species produce polymer matrices of large molecular weights very early during the polymerization.[13] This process just described encompasses one of the most widely used reaction schemes, free-radical polymerization of vinyl monomers.[5,6] The other class of polymerizations, step-growth,[13] includes condensation polymers, such as epoxies, and differs from chain reactions because monomers have to add together to form dimers, then trimers, and so on. This stepwise formation of the matrix means high molecular weight polymers are formed much later in the polymerization reaction than chain polymerization techniques.

The final variable to consider in PIPS is the formation of cross-links within the polymer matrix.[3-6, 13] Cross-linking occurs in both polymerization classes and requires the presence of monomers that possess multiple reaction sites, two or more for chain polymerizations or three or more for step-growth. The cross-links join the linear portions of the matrix to form a gel. As the number of cross-links within the matrix increase, the

elastic forces that act on the LC droplets also increase, and thus, the droplet shape becomes deformed.[3,4]

1.4

Descriptions of PDLC Phase Behavior

In order to control the formation, morphology, and distribution of the LC droplets, answers are needed for some of the following questions:[3-6]

What compositions ensure phase separation?

What temperature range does the PDLC maintain a stable phase-separated state?

How soluble is the LC in the host matrix?

How does the phase behavior change during polymerization?

What are the possible mechanisms for phase separation?

Leaving these questions unanswered can lead to problems in controlling LC droplet morphology as well as the amount of LC available for proper device operation. Therefore, understanding the phase behavior of PDLC's, either under equilibrium or non-equilibrium conditions, has been the subject of continuing interest for almost two decades.

The early works of Ballauf, Dorgan, and Soane[14,15] are concerned with the equilibrium phase behavior of different LC's blended with poly(styrene). Phase diagrams of these blends show upper critical solution temperature, or UCST, behavior, depicted in Figure 1.4. The distinguishing feature[16-18] of this type of phase diagram is the concave boundary between the single and phase-separated states of the blend when the mixing temperatures are plotted versus the volume fraction of one of the blend components.

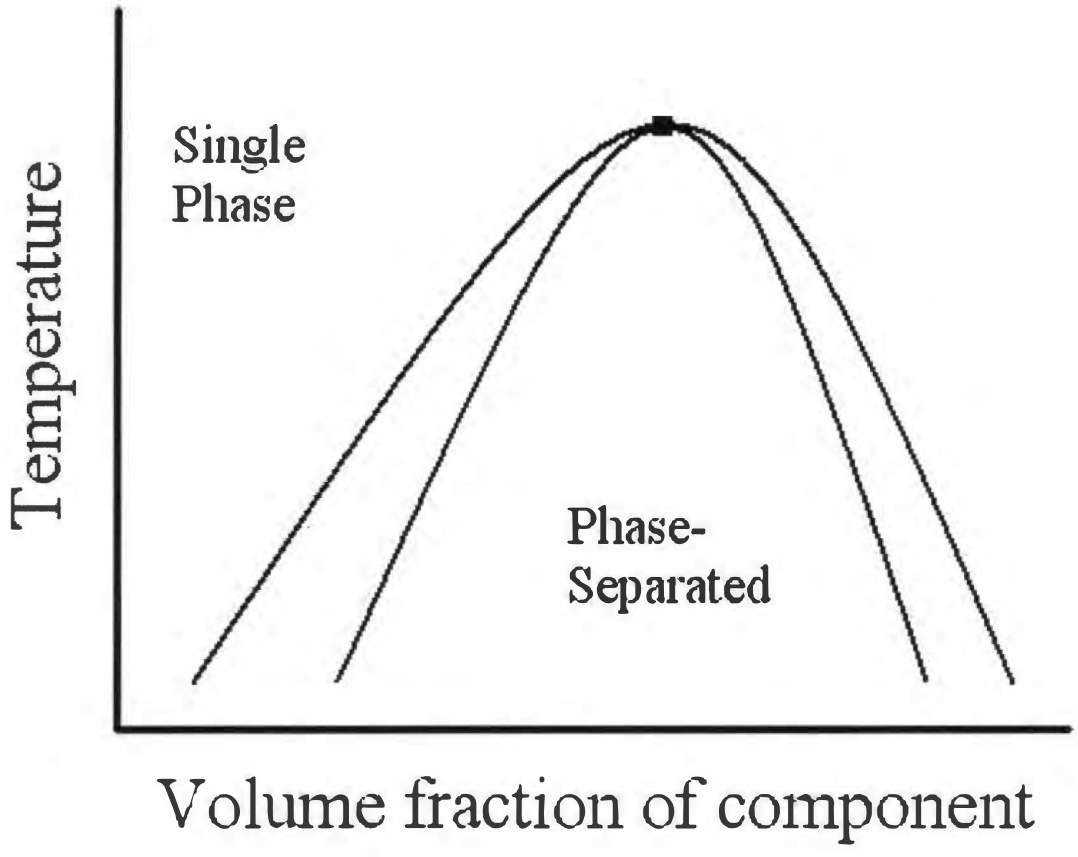


Figure 1.4 A simple upper critical solution temperature, or UCST, phase diagram

UCST behavior has been shown to be a hallmark of PDLC's, a fact confirmed later in experimental studies by Ahn, Chiu, Smith, Benmouna et al, and others.[19-24] The presence of a UCST represents an important step in being able to determine the phase boundaries for a given LC/polymer blend, however, the need to monitor both the changes in the phase behavior and make predictions about the phase behavior in untested systems requires a thermodynamic framework.

The most practical choice of thermodynamic description for PDLC's has been the lattice model found in Flory-Huggins (F-H) theory for polymer solutions. Independently developed by Flory and Huggins in the late 1940's[16-18] F-H theory uses a lattice model based on ideal solution theory and captures the essential features of UCST behavior. In this model the polymer is divided into segments arranged on a two-dimensional lattice,[16,17] as shown by the filled, connected dots in Figure 1.5, along with the solvent molecules, shown as the white circles. Polymers, unlike small-molecule solvents, do not have the ability to arrange themselves in just any random fashion. The bonds between the monomers coupled with the fact that monomers can not overlap reduces the number of configurations available to the polymer chain relative to mixtures of small molecules.[16,17,18]

The other variation from ideal solution theory to consider for polymer solutions is the difference in molecular size.[16-18] In the context of ideal solution theories, such as Raoult's law,[17] the size of both the solute and the solvent molecules are assumed to possess roughly equal molar volumes. This condition, when applied to a lattice model

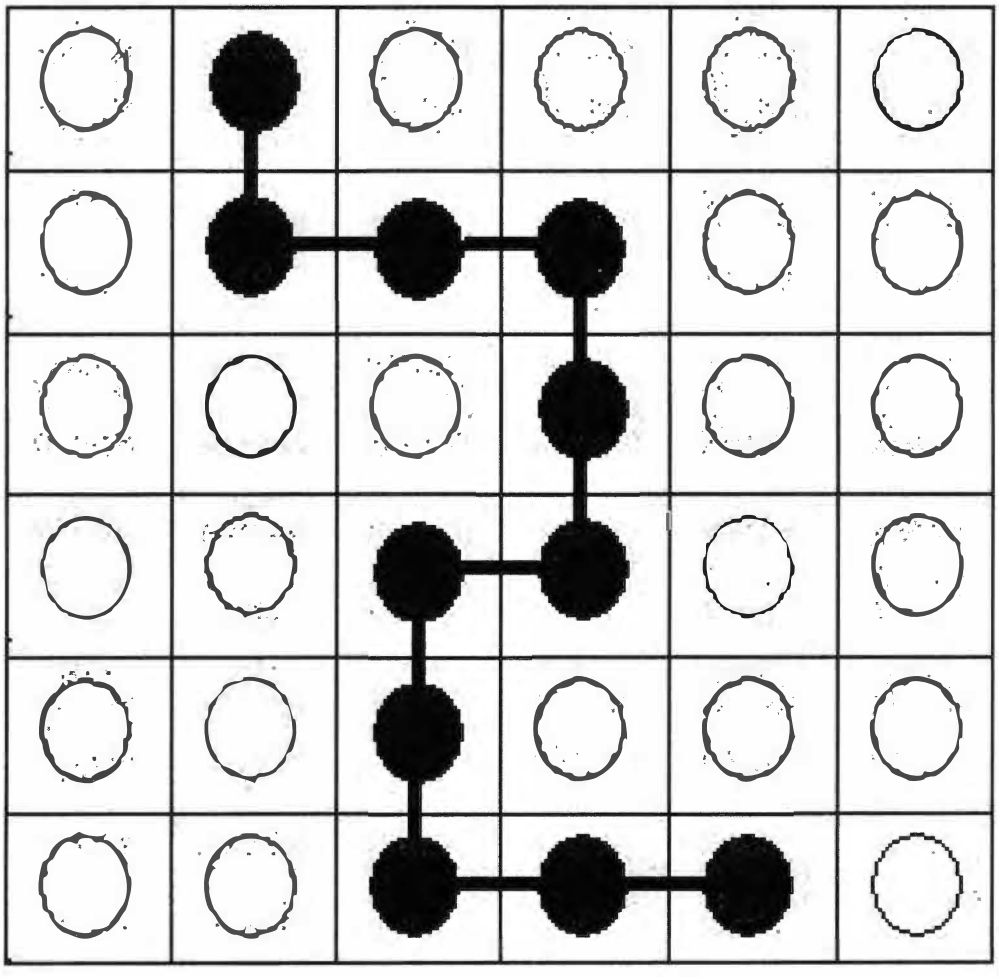


Figure 1.5 Representation of the lattice model used by Flory-Huggins theory: A polymer chain (black, connected circles) surrounded by solvent (white circles)

that describes an ideal solution, means that each solvent molecule is interchangeable[16,17] with each solute molecule on the lattice. However, since a single polymer molecule takes up a much larger volume than a given solvent molecule, the lattice sites can no longer be determined from mole fractions alone. Rather, the size of the lattice sites is set to the volume occupied by the solvent molecule. The polymer is then subdivided into r segments, each occupying the same volume as a single solvent molecule.

The change in free energy for any process begins with the general expression found in equation (E 1.9).[16-18] The first term, the enthalpy change, ΔH, is defined by

$$\Delta G = \Delta H - T\Delta S \qquad \text{(E 1.9)}$$

intermolecular interactions, and the second term characterizes the change in disorder, or change in entropy, ΔS. The description of the UCST phase diagram shown in figure 4 requires using the F-H lattice model to define the free energy of mixing, ΔG_m,[16,17] given in equation (E 1.9).

Defining the entropy of mixing, S_m, for F-H theory can be accomplished by examining, first, the entropy of mixing for two small-molecule components on the lattice before adapting the definition to describe polymer molecules in a solvent.[16,17] When discussing the change of disorder in a solution, the relationship of the total number of configurations must be made for the different components. For mixtures of small molecules, both components are free to arrange themselves in any fashion so long as two molecules do not occupy the same lattice site.[16-18] This relationship takes the total moles of solvent and solute molecules, n_{total}, along with the moles of the respective components,

n_{solute} and $n_{solvent}$, to give the total number of configurations, Ω, shown in equation (E 1.10), that solute and solvent can be arranged on the lattice.[16] Applying the

$$\Omega = n_{total}! / (n_{solute}! \, n_{solvent}!) \qquad \text{(E 1.10)}$$

Boltzmann relation to Ω yields the equation for the entropy of mixing, equation (E 1.11) which becomes (E 1.12) by Stirling's approximation of the factorials.[16,18] In these

$$S_m = k \ln \Omega \qquad \text{(E 1.11)}$$

$$S_m = - k (n_{solute} \ln x_{solute} + n_{solvent} \ln x_{solvent}) \qquad \text{(E 1.12)}$$

equations k is the Boltzmann constant, the n-values are the same as in (E 1.7), and the x-values are the mole fractions.[16] The change in entropy upon mixing of the two components results from the difference in entropy between the pure components, $S_{solvent}$ and S_{solute}, and the new mixed state, see equation (E 1.13).[16] However, since we are

$$\Delta S_m = S_m - S_{solvent} - S_{solute} \qquad \text{(E 1.13)}$$

only concerned with the entropy change that arises from the mixing process, that is, there are no pure components present, (E 1.12) is identical to (E 1.13) and is given by equation (E 1.14).[16]

$$\Delta S_m = - k (n_{solute} \ln x_{solute} + n_{solvent} \ln x_{solvent}) \qquad \text{(E 1.14)}$$

The definition for ΔS_m for polymer solutions follows the same reasoning that produced (E 1.14), however, we can no longer use the moles of both solution components to determine the number of configurations available to the entire solution. Instead, the expression for ΔS_m must account for the fact that the polymer segments are connected to one another.

To account for polymer connectivity in the expression of Ω for the solution we start by considering the placement of the (i + 1)th polymer chain with number of segments, r, onto a lattice that already contains i polymer molecules.[16-18] In this case we assume that the lattice has a total number of lattice sites, N, given in equation (E 1.15) below, where N_1 is the number of solvent molecules and N_2 is the number of polymer molecules.[16] Since the lattice already contains i polymer molecules, and the first

$$N = N_1 + rN_2 \qquad \text{(E 1.15)}$$

segment of the (i + 1)th polymer can be placed on any of the (N – ri) remaining sites. For the second segment, though, the number of sites available is limited to those in the immediate vicinity of the first segment. Therefore, a coordination number, z,[16] is introduced to define the number of lattice sites surrounding the first segment, and the number of those sites that are available for the second segment is given by equation (E 1.16). For the third segment, the coordination number is reduced in order to prevent

$$\text{Sites for second segment} = z(N - ri)/N \qquad \text{(E 1.16)}$$

the overlap with the second segment, thus the number of available sites is given by (E 1.17).[16] As for the placement of the remainder of the segments in the (i + 1)th chain, the

$$\text{Sites for third segment} = (z-1)(N-ri)/N \qquad \text{(E 1.17)}$$

expression for the number of sites remains unchanged, and the number of ways the (i + 1)th chain can be arranged, or ω_{i+1}, on the lattice is given by equation (E 1.18).[16]

$$\omega_{i+1} = z(z-1)^{r-2}N[(N-ri)/N)]^r \qquad \text{(E 1.18)}$$

With the number of configurations for the (i + 1)th molecule defined, we can express the number of configurations for the ith polymer chain in equation (E 1.19).

$$\omega_i = z(z-1)^{r-2}N[(N-r(i-1))/N)]^r \qquad \text{(E 1.19)}$$

In the final expression of Ω, we focus mainly on the ways all of the polymer chains can be arranged on the lattice.[16-18] This approach is still valid because the solvent molecules are not constrained by the same connectivity issues affecting the polymer chains, and they occupy the lattice sites that are left after all the placement of the polymers. As a result, Ω for the all of the polymer chains is given by equation (E 1.20).[16]

$$\Omega = 1/N_2!(\prod_{i=1}^{N_2} \omega_i) \qquad \text{(E 1.20)}$$

With substitutions made for ω_i, converting (E 1.21) to factorials, and applying Stirling's approximation, the entropy of mixing, S_m, is expressed as equation (E 1.21). The entropy

$$S_m = k\{ N_2 [\ln z + (r-2) \ln (z-1) +(1-r) +\ln r] - N_2 \ln (rN_2/N) - N_1\ln(N_1/N)\} \qquad \text{(E 1.21)}$$

change on mixing for the solution is the same as in (E 1.13), but the pure components are expressed as S_1 for pure solvent and S_2 for pure polymer. Unlike (E 1.13), however, the entropy for the pure polymer is the same as the first term in (E 1.21). Therefore, the entropy change, ΔS_m, becomes the equation (E 1.22).[16] Since the solution in F-H is

$$\Delta S_m = -k[N_1\ln(N_1/N) + N_2 \ln (rN_2/N)] \qquad \text{(E 1.22)}$$

defined as a lattice with N-number of sites, the total number of sites, N, is related to the moles of solvent as well as polymer.[16-18] The volume of each lattice site equals that of the solvent molecule. Therefore, the amount of the two solution components can be conveniently expressed as volume fractions,[16-18] shown in equation (E 1.23) where i = 1 is for the solvent and i = 2 is for the polymer. The change in entropy on mixing

$$\phi_i = r_iN_i/ N \qquad \text{(E 1.23)}$$

is now given by equation (E 1.24) where R is the ideal gas constant.[16-18]

$$\Delta S_m/NR = - [(\phi_1/r_1)\ln \phi_1 + (\phi_2/r_2)\ln \phi_2] \qquad \text{(E 1.24)}$$

As in the discussion of the entropy change, the enthalpy change on mixing, ΔH_m,[16-18] is formulated by first considering the change in interaction energy, Δw, that occurs when small molecules mix. To more clearly illustrate this situation, we consider the mixing of pure component 1 with pure component 2 depicted in Figure 1.6.[16] In the pure states, Pure 1 and Pure 2, the energy that results from intermolecular interactions arise from only 1,1 and 2,2 contacts, but when the components mix, the interactions, along with the energies, change due to the formation of 1,2 contacts. Equation (E 1.26) gives Δw where w_{12}, w_{11}, and w_{22} are solvent/polymer, solvent/solvent, and segment/segment interaction energies respectively.[16] The pairwise interaction[16-18]

$$\Delta w = 2w_{12} - w_{11} - w_{22} \qquad \text{(E 1.26)}$$

between 1,2 pairs is ½ Δw. ΔH_m can now be given by incorporating Δw along with the specifics of the lattice. Now ΔH_m becomes the relation in equation (E 1.27) where z is the lattice coordination number for nearest neighbors, N is the total number of lattice sites, R is the constant given earlier, T is the absolute temperature, and the ϕ's are the

$$\Delta H_m = ½ \, z \, NRT \, \phi_1\phi_2 \, \Delta w \qquad \text{(E 1.27)}$$

volume fractions. At this point the terms ½ z Δw embody the interactions between the different solution components that occur during mixing. These interactions are combined into a single interaction parameter, χ.[16,17] The final form of ΔH_m, therefore, is given by equation (E 1.28). The final expression for the free energy of mixing[16,17] in (E 1.10) is

$$\Delta H_m /NRT = \chi\phi_1\phi_2 \qquad \text{(E 1.28)}$$

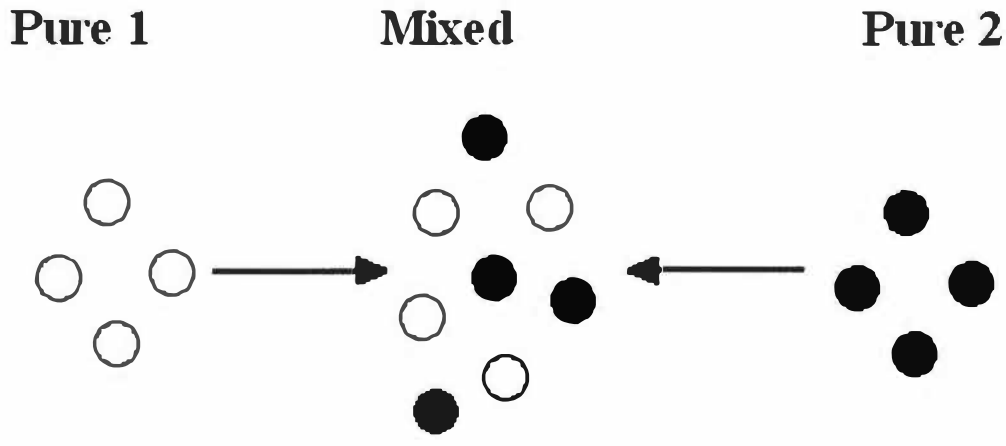


Figure 1.6. Representation of the mixing process as pure components, Pure 1 and Pure 2, change from pure (1,1) and (2,2) contacts to (1,2) contacts upon mixing

formulated by combining (E 1.10) and (E 1.13). This equation is shown in (E 1.29).

$$\Delta G_m/NRT = [-(\phi_1/r_1)\ln\phi_1 - (\phi_2/r_2)\ln\phi_2 + \chi\phi_1\phi_2] \qquad \text{(E 1.29)}$$

Equation (E 1.14) represents the basic thermodynamic description for mixing in polymer blends. From the free energy expression of F-H theory two important questions arise. How can the ΔG_m describe the UCST phase diagram, and what does the description say about phase stability?

In order to use (E 1.14) to describe the UCST recall first the example given in figure 1.4. The phase diagram exhibits three different regions, the area outside the curve being completely mixed and two different regions within the phase-separated region. An effective way to visualize the changes in ΔG_m can be found in Figure 1.7 where the free energy change is allowed to vary with solution composition, φ, at a constant temperature.[16,17] $\Delta G_m(\phi)$ is shown to decrease steadily until reaching a free energy minimum marked A where the energy begins to turn upward towards a local maximum. After the maximum is reached the free energy begins to decrease towards another minimum marked B and afterward begins to increase again. If the solution at this constant temperature lies between the minima, the higher free energy causes the solution components to favor separation. The minima are connected by the tangent line in the figure which corresponds to the change in chemical potential, $\Delta\mu$, in equation (E 1.30).

$$\Delta\mu = (\partial\Delta G_m/\partial\phi)_{T,P} \qquad \text{(E 1.30)}$$

Since A and B fall on the same line, the chemical potential is equal for both phases. As a result, the two compositions become the equilibrium values that form part of the boundary between complete miscibility and phase separation. When the temperature is

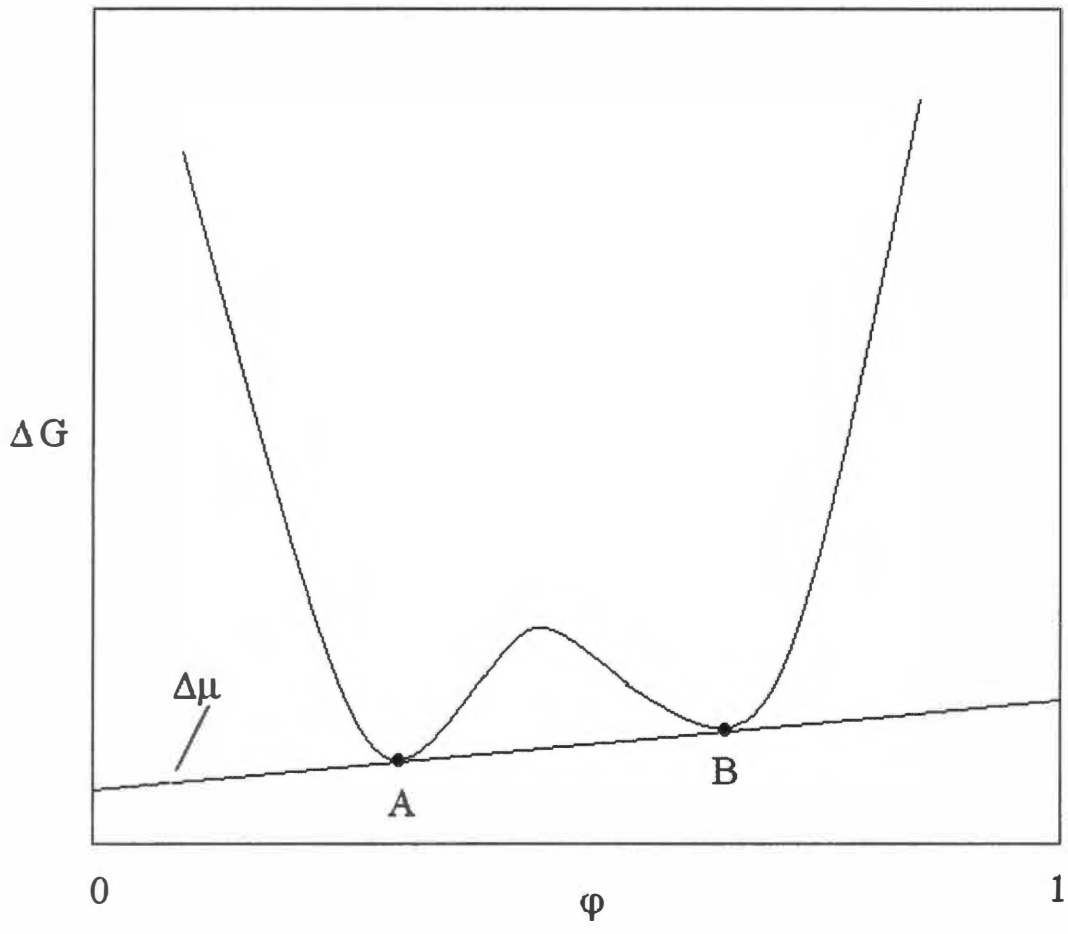


Figure 1.7 The variation of the free energy change, ΔG_m, with solution composition, φ, constant temperature

changed, different equilibrium compositions are obtained that complete the boundary shown in the phase diagram. This boundary is known as the binodal or coexistence curve[16,17] and is shown in a more detailed UCST phase diagram in Figure 1.8 as 8a. As for the separate regions under the binodal, the free energy diagram predicts these as well. The two regions, corresponding to the thermodynamic stability to the concentration fluctuations leading to phase separation, are described by the change in curvature, $(\partial^2 \Delta G_m / \partial \varphi^2)$, in Figure 1.7. For example, if the composition lies relatively close to point A, the positive curvature in the free energy means the blend is resistant to small composition fluctuations.[16,17] For phase separation to occur in this region, the solution must overcome some activation energy, and, therefore, this area is referred to as the metastable region[16,17] of the phase diagram. The second region occurs when the curvature becomes negative, the area close to the local maximum. Under these conditions the solution is no longer resistant to composition fluctuations, has become completely unstable,[17] and begins to phase separate. The boundary between the two different regions corresponds to zero curvature. This boundary is known as the spinodal curve, labeled 8b in Figure 1.8. The final feature of the phase diagram is the critical point of the solution, 8c in the phase diagram. The critical point[16,17] represents the convergence of the equilibrium values to a single composition. In terms of the free energy change the critical point corresponds to $(\partial^3 \Delta G_m / \partial \varphi^3)$ equal to zero.

With the connection of ΔG_m to the essential features of the phase diagram (E 1.14) is ready to be applied to the UCST behavior in PDLC's, however, to obtain a complete description of the free energy contributions one must also consider the phase of

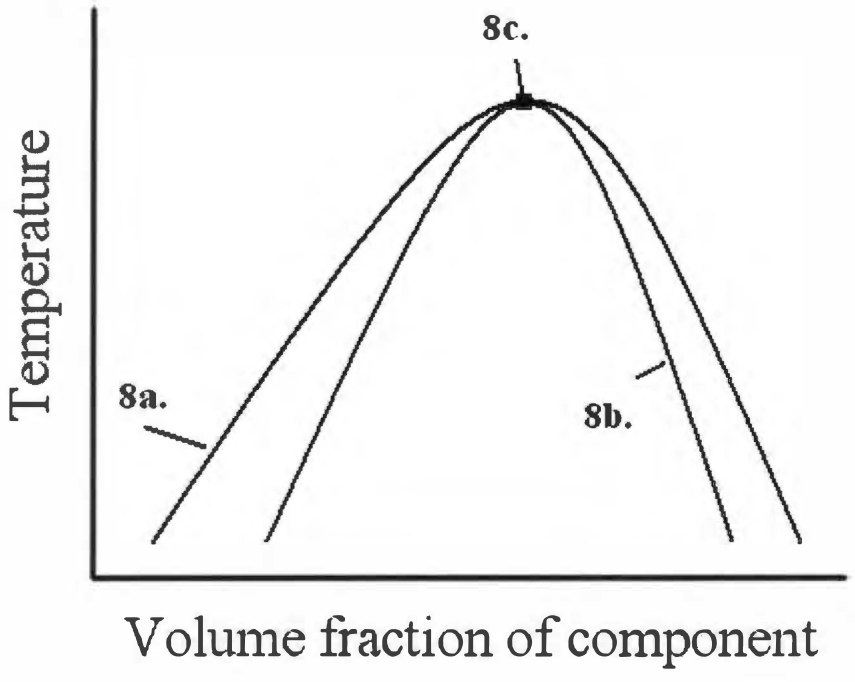


Figure 1.8 UCST phase diagram a. Binodal line, b. Spinodal line, c. Critical point

the LC. This issue has been addressed by several authors mentioned previously. Dorgan and Soane[15] use a modified version of F-H theory that includes an anisotropic contribution from Ronca for the LC. This early technique provides some of the UCST features, but fails when compared to experimental results. By far the most successful approach, though, comes from the theoretical and experimental work of Benmouna et al.[23] In their method the free energy, f, is expressed as the sum of two contributions, isotropic mixing, f_i, and anisotropic contributions, f_a, from the LC, see equation (E 1.31).

$$f = f_i + f_a \qquad \text{(E 1.31)}$$

The isotropic mixing term comes directly from the free energy expression from F-H while the anisotropic term uses either the Maier-Saupe theory if the LC is nematic or McMillan theory if a smectic LC is present. This approach not only captures the UCST behavior but also provides very good agreement with optical microscopy results for the coexistence curve of poly(styrene)/8CB blends.

When considering phase separation in any polymer blend, the thermodynamics make up only one part of the whole process. Indeed, even though the conditions of the blend might favor phase separation the actual separation will not take place if limited by kinetic factors.[25] The importance of kinetics of phase separation in the construction of PDLC's is no less crucial as the final properties of the resulting device depend on how the LC is separated from the matrix.[3-6]

For polymer matrices consisting of non-crosslinked polymers, such as those used during TIPS, kinetic descriptions of the phase separation are the same as those used in other polymer blends.[3,4] The first point to discuss in regards to phase separation is the connection to the initial thermodynamics of the system. Recall from the introduction to

phase stability given previously the phase diagram in Figure 1.8. In the beginning the blend is kept at a temperature where the LC is completely mixed with the polymer. If the blend undergoes a rapid temperature drop into either the metastable or unstable regions of the phase diagram, the blend will begin to separate into LC-rich and polymer-rich phases.[16-18, 25] When the temperature drop, also called a thermal quench,[17] is performed at different blend compositions, the depth of the quench can be used to control which region of the phase diagram phase separation takes place. An illustration of how thermal quenches work is given in Figure 1.9. The phase diagram in this figure is the same as the one given in Figure 1.7. Starting at point A the blend is completely mixed. The first temperature drop, from A to B, represents a relatively shallow quench into the metastable region. However, if the quench is much deeper, A to C, the phase separation takes place in the unstable region.

After thermal quenching takes place the details of the phase separation process are controlled by the flux, j, or the movement of the solution components as they form polymer-rich and solvent-rich domains.[25] The flux of a given component, i, in an ideal solution is given by Fick's law shown in equation (E 1.32). In this equation, D is

$$j_i = -D\phi_i \nabla \mu_i \qquad \text{(E 1.32)}$$

the diffusion coefficient, ϕ is the volume fraction of the component i, and $\nabla \mu_i$ is the chemical potential gradient. The driving force in this case arises from the chemical potential gradient. This means the inequality in μ's that occurs in unstable regions of the phase diagram drive the phase separation process, and under equilibrium where μ is equal everywhere the movement of material between stable phases reaches equilibrium.

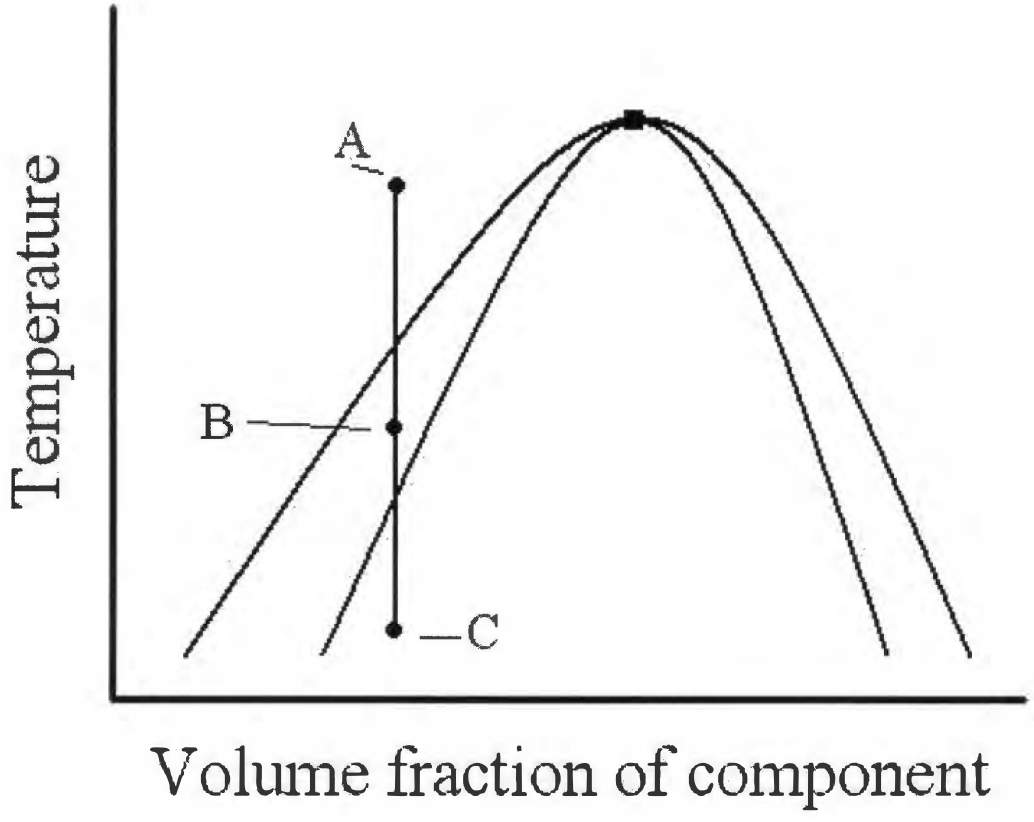


Figure 1.9 Illustration of thermal quench in TIPS: A, completely miscible, B, shallow quench, C deep quench

The mechanisms for phase separation depend on the quench depth. For shallow quenches just past the binodal line the blend resides in the metastable region of the phase diagram. For the separation of the components to occur in this region a certain amount of a given species must come together to form a nucleus of a critical size.[25] Once formed the nucleus continues to grow with time. As a result the mechanism just described is called nucleation and growth. Deep quenches past the spinodal line mean the formerly miscible blend becomes globally unstable. At this point minute composition fluctuations that normally would not result in phase separation under metastable conditions are enough to induce segregation, and over time the fluctuations are amplified. The solution begins to phase separate globally into interconnected domains. With time the interconnected structure is driven by interfacial tension to break up into spherical droplets. This mechanism, referred to as spinodal decomposition (SD),[16] occurs in distinct stages over time and is discussed in more detail in chapter five. Both phase separation mechanisms have been observed in PDLC's formed by TIPS. In a study performed by Kim and Kyu[26] results from light scattering experiments on blends of poly(styrene) and the eutectic liquid crystal mixture E7 show how quench depth affected the growth of phase separated LC. Shallow temperature quenches exhibit evidence of the nucleation and growth that produced LC droplets with a broad distribution of sizes. The deeper quenches exhibited behavior supporting spinodal decomposition, however, the earliest stage of SD was not observed.

Phase separation in blends undergoing PIPS has an added dimension to consider, the formation of a polymer matrix during polymerization.[3-6] The single phase diagram used previously can no longer be used because of the continually increasing polymer

molecular weight. In order to visualize the changing thermodynamic environment that affects the starting point for phase separation an idealized version of the PIPS process is shown in Figure 1.10. The figure shows the blend composition, A, as polymerization proceeds isothermally from time t1 to t3. At t1 the matrix has not grown large enough to thrust A into a region favoring phase separation of the LC. When t2 is reached, the matrix has grown forcing the phase diagram upward and outward, thereby placing A within the metastable region. Lastly, A is thrust deeply into the unstable region of the new phase diagram as the polymer matrix grows even larger. From this illustration one can see that PIPS creates a highly complex path for the blend to follow for phase separation. The starting composition and the polymerization rate control how quickly A crosses the binodal line. Additionally, if the polymerization includes a cross-linking agent, the resulting matrix can affect the LC's ability to phase separate.

Understanding the complex nature of the PIPS environment has been the subject of several studies that focus on thermodynamics as well as phase separation kinetics. The early work of Lin and Taylor[27], for example, combine F-H theory with the polymerization kinetics of Stockmeyer for cross-linked matrices formed by condensation reactions, i.e. epoxies. From this work they show the evolution of the phase diagrams occurring in a similar fashion to the idealized process shown in the previous figure. Later, Serbutovietz, Taylor, Kloosterboer and others[28,29] also use F-H to model the thermodynamic changes that occur during PIPS, but they change the reaction kinetics to reflect free radical polymerization as well as incorporate Flory-Rehner theory to account for the network elasticity contribution to the free energy from cross-linking. The adaptation of the thermodynamic approaches to the study of phase separation kinetics has

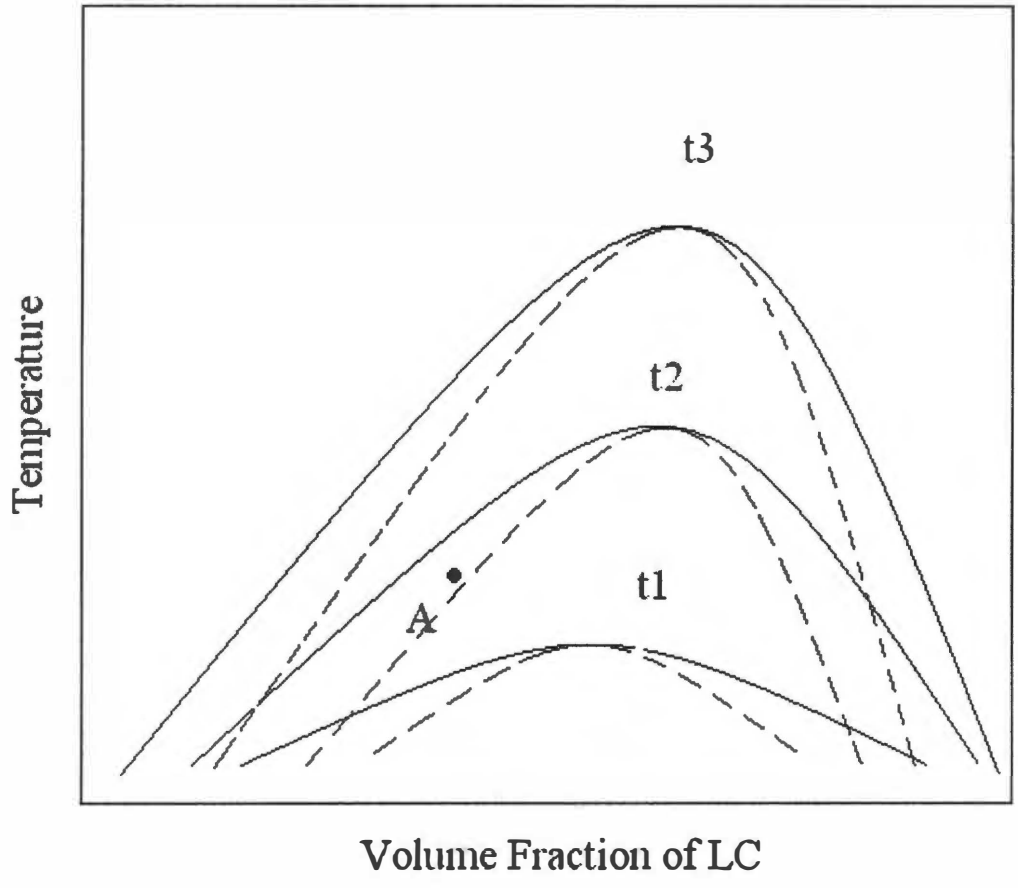


Figure 1.10 Visualization of PIPS process: A, the blend composition, changing phase diagrams with increasing polymerization times, t1 – t3

been important in understanding the complex scattering behavior of blends undergoing PIPS. The work performed by Chan, Rey, Kyu, Chiu, Nwabunma, and others[30-34] expand the thermodynamic models through the incorporation of time-dependent models for the diffusion of the solution components during phase separation. The results of the calculations successfully reproduce many of the experimental results for LC morphologies produced by SD and NG, however, the phase separation is not shown to proceed as in the thermally quenched blends of TIPS. Instead, a delay is observed between the growth of the polymer matrix and the onset of phase separation.[30-34] In addition to the delay, the cross-linked matrices change droplet morphology, and the resulting vitrification of the matrix prevents further phase separation of the LC.

1.5

Goals and Experimental Strategies

A constant theme in the material presented thus far is the vital role of the polymer matrix in the phase behavior of PDLC's. Whether the issue is dealing with the fundamental properties that affect LC solubility or the phase separation of the LC during matrix formation, small changes in matrix choice and construction method can dramatically affect LC droplet morphology, hence, PDLC device performance.

From the discussion of F-H theory in the previous section the molecular weight of the polymer strongly affects LC solubility through the entropy of mixing. Although previous work such as that performed by Benmouna et al[25] on poly(styrene)/8CB blends and the experimental/theoretical works that followed have laid the foundation for application of F-H to PDLC's, this area still requires further study. For one, such a study is lacking for acrylate-based matrices as well as to polymer molecular weights that do not

exceed 2 x 10^5 g/mole. Another issue becomes quantifying the changes in LC solubility. Therefore, the goal of chapter three involves determining the effect of polymer molecular weight in poly(methyl methacrylate), or PMMA, blended with 8CB. Our strategy employs optical microscopy to determine the phase diagrams of the blends with PMMA weights ranging from 25,000 to 660,000 g/mole. The microscopy data, used in conjunction with F-H theory, allows for the extraction of the interaction parameter χ.

Another important parameter determined in Chapter 3 is known as the solubility limit of the LC in the polymer matrix. This quantity, originally determined by Smith,[20-24] accounts for the fraction of LC that remains trapped in the matrix, a common characteristic of all PDLC's that can decrease the optical performance as well as increase the cost of PDLC device construction. The technique that is used to determine the solubility limit involves a procedure developed by Smith and co-workers[20-22] where the LC nematic-isotropic transition is measured by differential scanning calorimetry, or DSC. By determining the decrease in this transition enthalpy with decreasing LC content, this method gives the fraction of LC remaining in the matrix. Many studies have used this method to determine the solubility limits for different polymer/LC blends including an important work by Benmouna that suggests the value is independent of the chemical composition of the matrix.[23]

LC solubility can also be affected by changing the chemical make-up of the polymer used in PDLC construction. If unfavorable interactions between the LC and the matrix exist, a greater fraction of LC separates from the matrix.[32] The presence of such interactions can also improve PDLC device efficiency by reducing the anchoring strength of the LC to the droplet walls.[3,4,10,35] The result is a more efficient use of LC both in

terms of cost and device performance. Fluorinated polymer matrices have been used in the construction of PDLC devices, however, the thermodynamics of these blends is not well understood. Chapter four explores LC solubility changes in blends consisting of 8CB and a fluorinated copolymer, poly(2,2,2-trifluoroethyl methacrylate-co-methyl methacrylate), with increasing 2,2,2-trifluoroethyl methacrylate content. Like chapter three, optical microscopy is used to determine the phase diagrams, and F-H theory is again used to extract interaction parameters.

PDLC's constructed by PIPS initiated by photopolymerization are becoming a popular choice for the construction of electro-optical devices for photonics applications. Studies of blends undergoing PIPS by photopolymerization have by and large consisted of a "before and after" approach where the LC is removed after curing of the matrix so the voids left behind can be measured by microscopy or scattering techniques.[36,37] Measuring the phase separation kinetics *in situ* requires the use of techniques that are able to capture the phase separation as it occurs. A practical choice in this respect is time-resolved light scattering since the laser used can access length scales smaller than those accessible by conventional optical microscopy as well as capture the changes in phase behavior over the course of polymerization. Light scattering has been used to monitor the phase separation of LC from PDLC's cured by ultraviolet radiation,[32] but due to problems in filtering the stray light the measurements could only be made by turning off the UV source first. In chapter five the problems of removing stray light from time-resolved light scattering is addressed by using PDLC syrups obtained from colleagues at Wright-Patterson Air Force Base that undergo curing in the presence of a green laser as the narrow wavelength of the cure laser creates the possibility of easier filtering. Thus

experiments can be conducted with the goal of determining the effect of increasing LC content as well as how changes in polymerization rate by differing cure beam intensity change the phase separation of the LC.

CHAPTER 2

Experimental Techniques

2.1

Microscopy

The need to observe the actual changes in PDLC phase behavior and morphology during processing is of vital importance in understanding the effect of changing conditions such as temperature, polymer molecular weight, matrix composition, etc on the resultant composite. Observations such as these require a technique capable of capturing real images on length scales too small for the unaided eye. As a result, optical microscopy, or OM, has become a highly valuable tool in PDLC research.

Microscopy's value, as stated above, lies in its ability to form real images of specific regions of a given sample.[38-40] Image acquisition is achieved by the interaction of either light or electrons[38] with the bulk of the sample or surface under study. The images produced in this manner can reveal fine detail about the morphology[38-40], i.e. LC droplet size or shape in PDLC's,[4] as well as how the structure changes from region to region. This capability contrasts with the structural information provided by scattering techniques[38] that average the interactions of the light passing through the sample over the entire sample volume that is illuminated by the radiation.

OM uses visible light that either passes through the sample, called transmission, or is reflected off the surface, [38-40] however, in this discussion only transmission OM is considered due to its prevalence in the determination of phase diagrams for PDLC's. A typical schematic of a transmission optical microscope can be seen in Figure 2.1. The

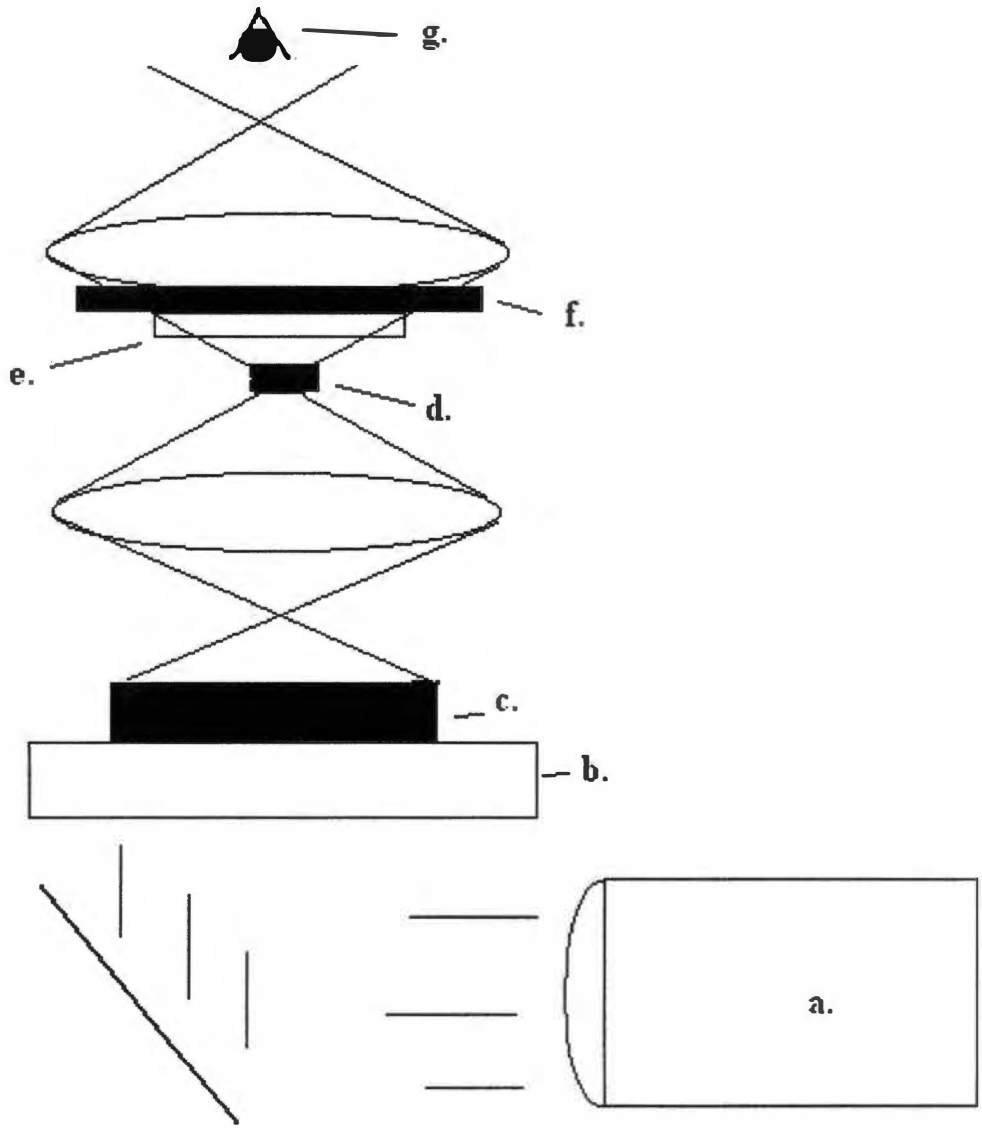


Figure 2.1 Schematic of an optical microscope, a. light source, b. condenser annulus, c. polarizer, d. sample, e. phase plate, f. analyzer, g. observer

microscope consists of a light source, 2.1 a., which provides a beam of light that usually passes through what is called a substage condenser lens. The light then passes through the sample, 2.1 d., where the surface image passes through the objective lens that magnifies the image. Finally, the image passes from the objective to either an eyepiece or camera where the image can be perceived by the observer, 2.1g.

An important concept in the formation of images by optical microscopy is the contrast.[38-40] The contrast results from the intensity difference between specific features in sample and overall transmitted light. This intensity difference is produced by different interactions that occur within the sample, such as absorption, brightness, birefringence, color variation, fluorescence, etc.[38-40] Although many contrast enhancement techniques have been developed to exploit the differences between the features and the bulk of a sample, our optical microscopy studies use only two techniques.

The first contrast enhancement technique, known as crossed-polarizer mode,[39,40] uses the two polarizers in figure 2.1 c. and f. Illumination from the source passes through the first polarizer, 2.1 c., which plane-polarizes the light. As before the light interacts with the sample, however, instead of passing on to the observer, the light must travel through the second polarizer, called the analyzer, 2.1 f., which is set perpendicular to the first. If the sample being viewed is isotropic, the perpendicular setting of the two polarizers cause the image to appear dark.[39,40] For anisotropic materials, such as LC's in either the nematic or smectic phases, the result is much different. Recall from the discussion of LC's from Chapter 1 the concept of birefringence.[3,4,9-11] In birefringent LC's incoming light experiences different refractive indices that convert the incoming light into two perpendicularly polarized components. The result is a change in the

polarization of the illumination between the sample and the second polarizer to an angle between 0° and 90°. Since the changed plane-polarized light is in a plane of intermediate angle to the two polarizers, the sample appears bright.[39,40]

The second contrast enhancement technique, phase contrast mode,[38-40] is employed when the sample contains two or more components whose refractive indices are very similar. This condition creates difficulty when trying to resolve the different phases that might exist because the observer is unable to distinguish little if any detail. Phase contrast overcomes this difficulty by using two optical components,[39,40] a condenser annulus placed in front of the light source, see Fig. 2.1 b., as well as a phase plate located between the sample and the objective lens, Fig. 2.1 e. The phase plate changes the small differences in refractive index of the two components into amplitude changes in intensity. The result of the amplitude changes is an increase in the observable contrast between the different components in the sample.

The use of OM in the modes described has been crucial in the determination of PDLC phase diagrams. The experiments are carried out by placing the microscope slide with the PDLC sample on a heating stage. The temperature is then gradually increased in order to observe the anisotropic textures of LC-rich domains at lower temperatures under cross-polarized mode or the mixing of the isotropic LC with the polymer matrix at higher temperatures under phase contrast. The successful use of this technique is exemplified by the studies of Ahn and Kim[19] in establishing the phase diagrams of poly(methyl methacrylate)/7CB and poly(styrene)/7CB blends, Benmouna et al[23] for poly(styrene)/8CB blends, Maschke et al[41] for cured and uncured propoxylated

glycerotriacrylate/5CB blends, and more recently by Gogibus et al[42] for poly(siloxane)/5CB blends.

Although optical microscopy provides a very useful method to determine various aspects of PDLC structure, there are limitations to the information it can provide. Of primary concern is the inability of OM to resolve objects smaller than ~0.5 μm.[38] Such a limitation makes the study of PDLC's with very small LC droplets very difficult. For example, in holographic diffraction gratings the fast matrix formation that occurs during PIPS often produces LC droplets on the order of 50 to 200 nm.[36] A change in microscopy technique becomes necessary, and scanning electron microscopy, or SEM,[38] is the most common choice.

SEM contrasts with OM in several different ways and requires different sample preparation techniques.[38] Rather than a light source, SEM uses a beam of electrons emitted from a probe that scans just above the surface of the sample. The electrons are produced from high voltage applied to a filament under high vacuum, focused by magnetic lenses, and penetrate the specimen.[38] Interaction with the sample material produces three separate signals that are used to produce the image as well as some compositional data.[38] The signal that produces the image originates from low-energy secondary electrons emitted from the top few nm of the sample. The amount of secondary electrons, hence the signal, changes with variations in surface features, i.e. holes or peaks. The signal variation translates into the surface features captured in the resulting image. The second signal comes from "backscattered" electrons that are elastically scattered by the atomic nuclei in the sample. Backscattered electrons are not only used to enhance image contrast but also give surface composition. Sample

preparation techniques require much more care than solvent-casting methods alone.[38] Of great importance is the removal of the LC from the film as the vacuum conditions within the SEM could cause the LC to evaporate and potentially damage the instrument.[36]

In the present work SEM is used, not as the primary, but as a complimentary technique for the time-resolved light scattering results of the PIPS studies in Chapter 5. After the PDLC syrups are fully cured they are sent to Wright-Patterson Air Force Base in Dayton, Ohio. There high-resolution SEM for each sample is performed courtesy of Dr. T.J. Bunning's research team, and the results are returned to us. The SEM images are analyzed by taking measurements of the voids left after LC removal. The average size of the voids as well as the fast Fourier transforms (FFT's) of the images are determined by using an image analysis program, ImageJ, a JAVA-based version of NIHImage.[43]

2.2

Differential Scanning Calorimetry

In Chapter 3, the study of polymer molecular weight effects on the phase behavior of 8CB/PMMA blends requires the determination of the phase diagrams and another parameter, the solubility limit. The solubility limit, referred to as β, corresponds to the amount of LC that remains dissolved in the polymer matrix at equilibrium and is determined by differential scanning calorimetry, or DSC.

DSC[44,45] is used to indirectly study both thermodynamic and kinetic events that occur within a given sample. The measurement of these events is accomplished by measuring the differences in heat flow between the substance under study and a reference sample as a function of temperature over the course of a programmed temperature change.

The instrumentation for DSC's falls into one of two categories. The first category, called power compensated DSC,[44,45] places the sample and reference materials into separate, insulated vessels. The two materials are heated so that the temperatures in each vessel are identical throughout the heating program. The difference in the power supplied to the sample, as compared to the reference, is converted to a signal that is recorded by the instrument.[45] Since the signal is directly proportional to the power difference, the amount of heat that is either absorbed or released can be determined by analyzing the input power, in mW, as a function of temperature. The second category of instrumentation is known as heat flux DSC[44,45] and describes the instrument used in our study of the solubility limit. Unlike the power compensated instrument, heat flux DSC does not separate the sample and the reference materials. Rather, the materials are placed in pans, usually made of aluminum, and heated on a thermo-electric disk. The difference in heat flow between the two pans is measured by thermocouples that are kept in contact with the pans, as depicted in the schematic shown in Figure 2.2. The heat flow is recorded in terms of a power differential, also in mW, between the two thermocouples and plotted as a function of temperature.[44,45]

An illustration of how some of the thermodynamic or kinetic events appear in a typical thermograph is depicted in Figure 2.3 a-c.[45] The step-like feature shown in 2.3 a. shows the change in heat flow when the sample undergoes a glass transition from glassy to rubbery behavior. The trough, shown in 2.3 b., represents an endothermic event. Such an event is observed when the sample absorbs heat from processes like melting or, in the case of liquid crystals, transitions from one mesophase to another.[3,4]

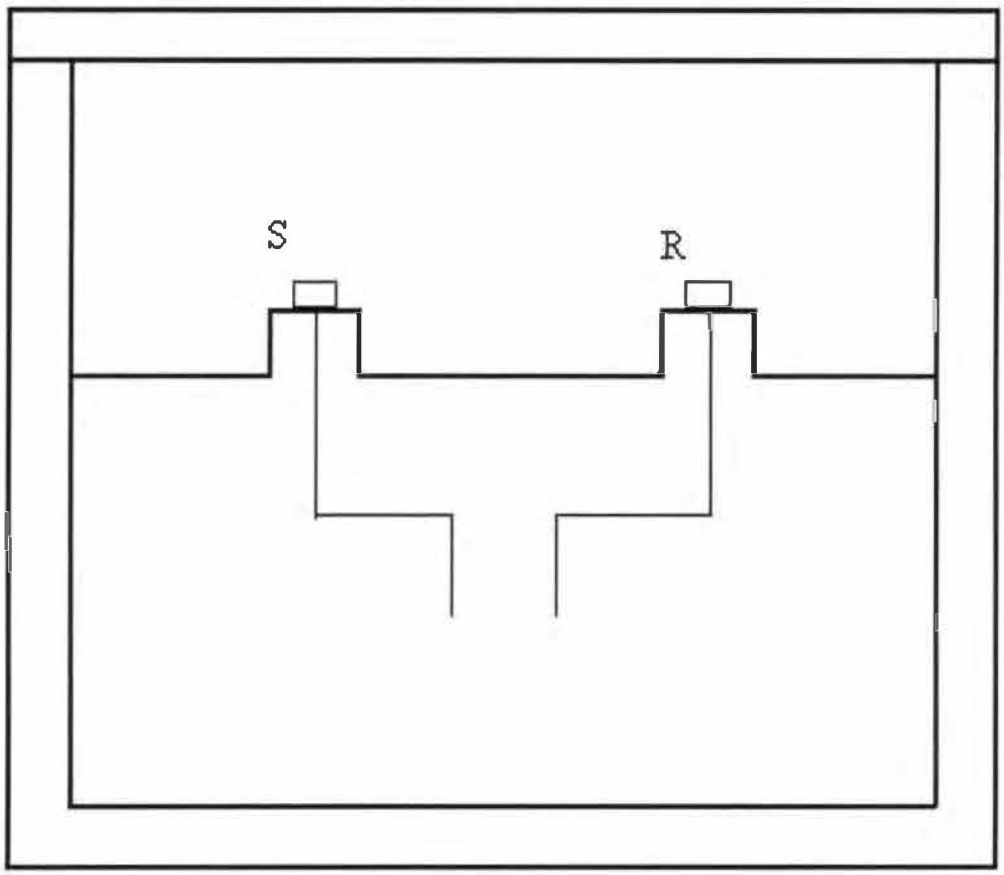


Figure 2.2 Schematic of a heat flux DSC. S is the sample pan, and R is the reference pan.

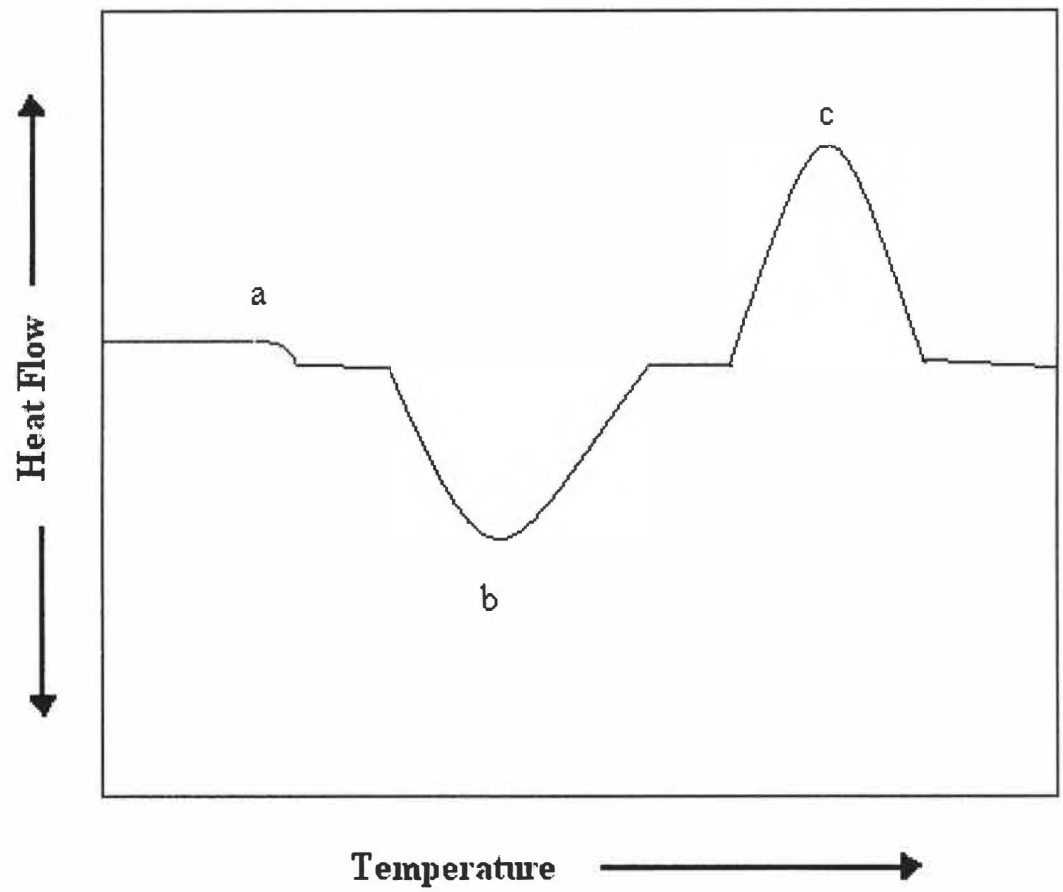


Figure 2.3 Representation of a DSC thermograph, a. glass transition, b. endothermic event, c. exothermic event.

The peak in the thermograph, 2.3 c., shows the affect of an exothermic event.[45] The increase of heat can come from many different processes that include curing reactions, crystallization, or thermal decomposition of the sample.[45]

Once the temperature program has ended, the changes in the heat flow can be analyzed in the context of the thermodynamic and/or kinetic events that take place within the sample.[45] For the glass transition the midpoint of the "step" in the thermograph is defined as the glass transition temperature.[45] For the endothermic and exothermic events shown in the figure the integration of each curve yields the amount of heat that is associated with the transition. Since the mass of the sample is known in the experiment, the heat can be used to determine the enthalpy change, ΔH, of the event.[44,45] In this way DSC can be used, for instance, to quantify the amount of crystallinity in a polymer sample,[45] the heat evolved during polymerizations, or the energy of first-order phase transitions.

In PDLC research, DSC has been used to determine the fraction of the LC that always remains trapped in the polymer matrix, or the solubility limit, β. The determination of β, in this case, is accomplished through the measurement of the LC's nematic to isotropic transition enthalpy, $\Delta H_{N\text{-}I}$. Smith and others[20-22] observe a linear decrease in the measured $\Delta H_{N\text{-}I}$ with decreasing LC content. Since only the phase-separated LC contributes to $\Delta H_{N\text{-}I}$, β can be determined via the lever rule[21,22] when the $\Delta H_{N\text{-}I}$ of the PDLC is normalized to that of the pure LC.

2.3

Time-resolved Light Scattering

The final chapter of this thesis studies the effect of LC content and cure beam intensity on the kinetics for the phase separation of the LC during photo-polymerization induced phase separation. In order to accomplish this task, an experimental technique that can monitor changes the growth of LC domains with time is required, and as a result, time-resolved light scattering is chosen.

The scattering of light is described in the following way. As the radiation propagates through a given medium, the electrons within the medium oscillate and scatter light.[46,47] If the medium is completely homogeneous on the length scale of the wavelength of the radiation, the scattered light experiences equal constructive and destructive interference, and as a result, the medium appears transparent. For media that contain inhomogeneities on length scales on the order of the wavelength of the propagating light, the scattered radiation undergoes constructive, rather than destructive, interference and, when viewed, appears opaque.[46,47]

For polymer blends that are undergoing phase separation, the inhomogeneities responsible for scattering are created by the growth of concentration fluctuations that are driven by chemical potential gradients.[46] The concentration fluctuations cause the dielectric constant within the blend to vary, and the light passing through the blend is scattered efficiently. The intensity of the scattered light in the forward direction is proportional to the variations in the dielectric constant according to the relationship given in equation (E 2.1)[46] where λ is the wavelength of the light, τ is the scattering volume,

$$I \propto (\pi^2/\lambda^4)\, \tau \langle \delta\varepsilon^2 \rangle \qquad \text{(E 2.1)}$$

and $<\delta\varepsilon^2>$ is the average square of the dielectric constant fluctuation.

The basic time-resolved light scattering experiment monitors the change in scattering intensity with time, as depicted in Figure 2.4.[46] In the figure I_0 is the intensity of the incident radiation, D is the detector that is used to detect the radiation, k_i is the wave vector of the incident beam, k_f is the wave vector of the scattered radiation that reaches the detector, and θ is the scattering angle between k_f and k_i. The incident beam, propagating as the vector $\mathbf{k_i}$, is scattered in all directions by the phase-separating LC, including the scattering vector, $\mathbf{k_f}$, recorded at the detector. The vectors, $\mathbf{k_i}$ and $\mathbf{k_f}$, are related to each other by the wave vector **q**, shown in equation (E 2.2). The wave vector

$$\mathbf{q} = \mathbf{k_f} - \mathbf{k_i} \qquad \text{(E 2.2)}$$

in (E 2.2) is related to the scattering angle and wavelength of the incident radiation given in equation (E 2.3). Since q has units of inverse length, the scattering that is measured at

$$|\mathbf{q}| = (4\pi/\lambda)\sin(\theta/2) \qquad \text{(E 2.3)}$$

a given angle provides a measurement of the size of the phase-separated domains.[46,47] The scattered intensity also depends on the shape, distribution of the domain sizes, and the correlation of the domains to each other in the volume that is being probed during the experiment. As a result, the intensity, I, must be expressed as a function of wave vector and time through a correlation function, S(q,t), called the form factor, and a proportionality constant unique to the specific experiment, K, shown in equation (E 2.4).[46]

$$I(q,t) = K\,S(q,t) \qquad \text{(E 2.4)}$$

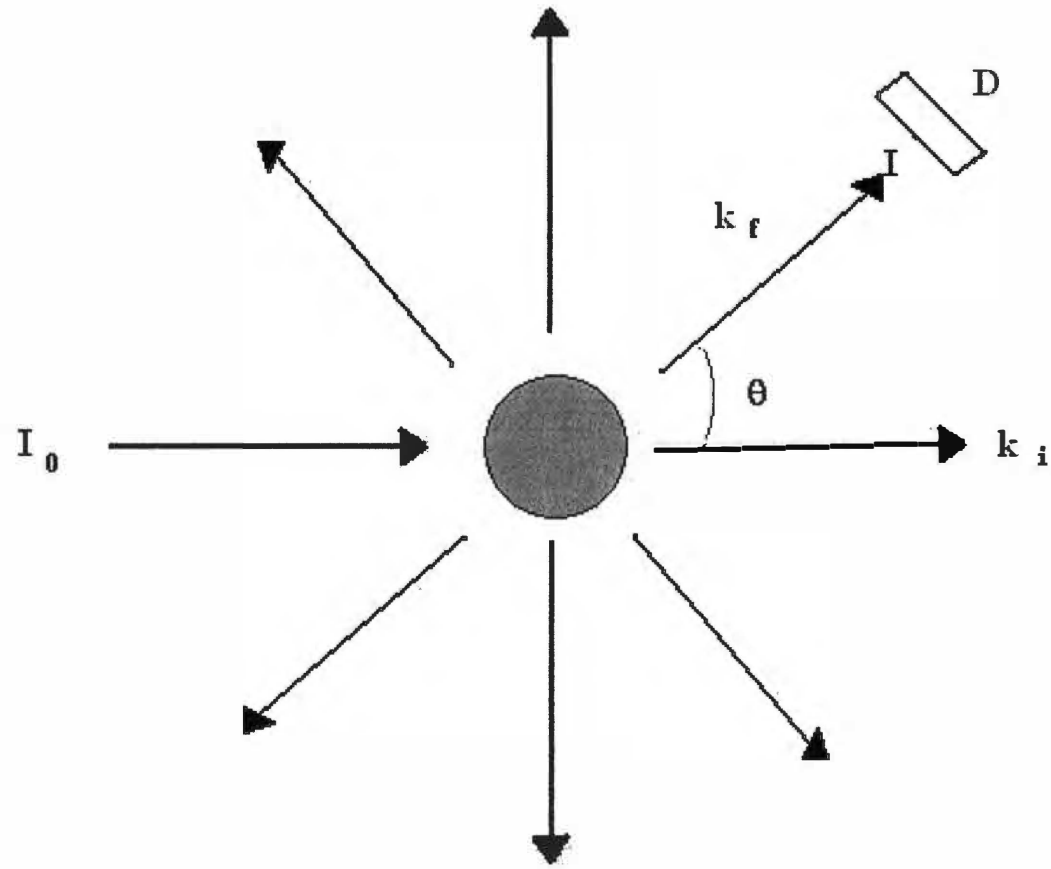


Figure 2.4 Representation of the scattering of light during a time-resolved light scattering experiment

Time-resolved light scattering has been employed by several different groups to study the phase separation of LC's under different conditions. In the early studies of Maugey and Navard,[48] time-resolved light scattering experiments of UV-cured PDLC's exhibit maxima in the scattering intensity with the formation of LC droplets. Using this study as a foundation, other authors have also used time-resolved light scattering, coupled with theoretical and microscopy techniques,[49-53] to study the growth of LC droplets in PDLC's with linear and cross-linked polymer matrices.

Time-resolved light scattering experiments are performed using an instrument based on the one employed by Sato and Han[54] to study phase separation kinetics in poly(styrene)/poly(vinyl methyl ether) blends, see Figure 2.5. The probe beam originates from a 20mW He-Ne laser that passes through a pinhole to a lens that focuses the beam on the sample, held perpendicular to the beam. Scattered light from the sample is collected by collimation lenses, passed through a red Kodak wratten filter to remove stray green light, and focused onto a 512 pixel photodiode array detector (Princeton Instruments, RY-512). Control of the angle for the collimation lenses and detector is provided by a goniometer. Data from the detector is collected every 0.1 s by a controller (Princeton Instruments, ST-120) connected to a PC. Control of exposure times for the scattering experiments as well as the number of spectra recorded is accomplished by the PC running WinSpec v. 1.0.

Determination of the scattering angles that are measured by the photodiode array is carried out in the following manner. First, the detector is aligned such that, when the goniometer arm is set to zero degrees, direct illumination of the HeNe laser on the

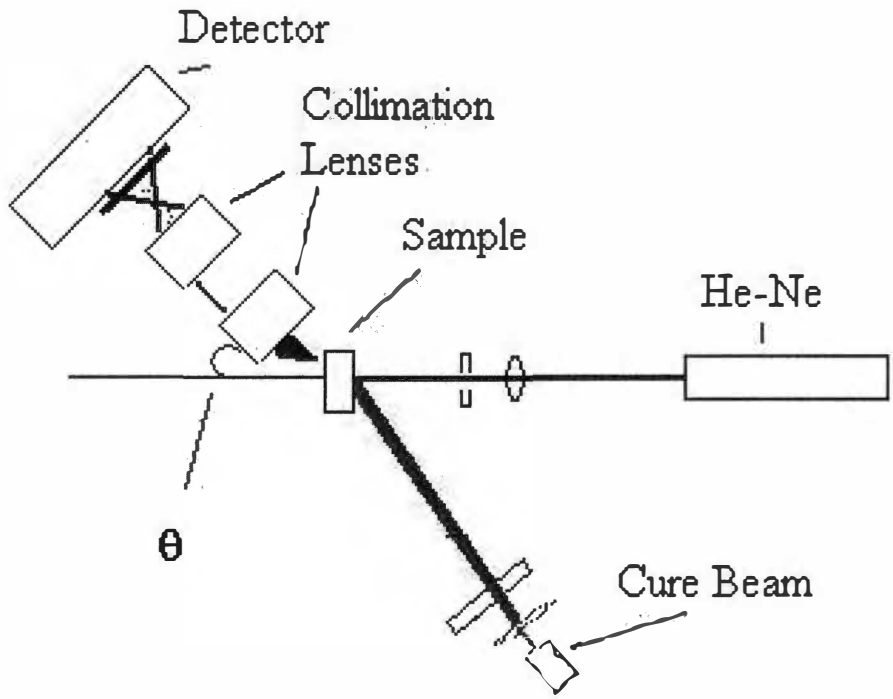


Figure 2.5 Schematic of the time-resolved light scattering instrument used in the measurement of the phase separation kinetics studies that occur during PIPS

detector through the optical train. Rotation of the goniometer moves the array across the HeNe beam until the angle of the arm places the beam on the last pixel, in this case 32.37°. During the rotation the angle of the arm, θ, along with the pixel number, X, illuminated by the laser are recorded periodically to determine the angle as a function of pixel number, $\theta(X)$. With $\theta(X)$ we are able to assign scattering angles to every pixel in the array. The angles are related to the wave vector, q, by equation (E 2.3).

The cure beam is produced by a 3mW green diode laser (532nm, B &W Tek, Inc.) passed through a narrow band pass interference filter (532nm, Edmund Industrial Optics). In order to ensure the uniform illumination of the sample we employ two different optical elements. The first element is a diffusion plate placed between the beam emerging from the band pass filter and the sample. Due to the attenuation of the cure beam, however, the diffusion plate is only used for the lowest cure intensity, 0.069 mW/cm^2. For the higher cure beam intensities, 0.14-0.69 mW/cm^2, the diffusion plate is replaced by a double concave lens (focal length -30mm) located between the diode laser and the bandpass filter. The cure beam is defocused to provide complete sample illumination, and the intensity at the sample is controlled by adjusting the distance of the diode laser to the lens. Cure beam intensities at the sample are measured by a digital light meter (Lutron LX-101A) held at the sample holder. The meter gives the power of the light from the cure beam in units of illuminance, or lumens/m^2. The lumen is related to the power by the conversion 588.746 lumens/W.

2.4

Polymerizations

Whenever possible, our study uses polymers that are commercially available, however, all of the polymers in Chapter 4 require their polymerizations in lab. The polymerization of acrylate monomers can be easily accomplished through a variety of free-radical reactions, but the reaction scheme that is used in this work is atom transfer radical polymerization, or ATRP.

ATRP is based on the small-molecule reaction that is known as atom transfer radical addition, ATRA,[55] see Figure 2.6. ATRA forms carbon-carbon bonds by using a transition metal catalyst, M_t^n, that abstracts a halogen, X in the figure, from an organic halide, R-X. The result is the production of the radical, R·, and the oxidized transition metal halide, $M_t^{n+1}X$. The radical can then initiate the reaction with the alkene, as shown at the bottom of the figure, to form the intermediate product. The intermediate reacts with $M_t^{n+1}X$ to form the final product, a new organic halide, and regenerate the transition metal catalyst, M_t^n. The transfer of the halide via the redox of the transition metal catalyst serves to mediate the reaction between R· and the alkene. The works of Matyjewski and others[55-58] use the controlled production of free radicals in ATRA and extend the process to the polymerization of vinyl monomers.

As with all free-radical polymerizations, ATRP consists of three different reactions that occur throughout the process, initiation, propagation, and termination,[13,55] shown in Figure 2.7. The initiation reaction begins with the formation of radicals from the organic halide, R-X, via the same process in Figure 2.6. The second reaction, propagation, occurs when radicals produced during the initiation process react with

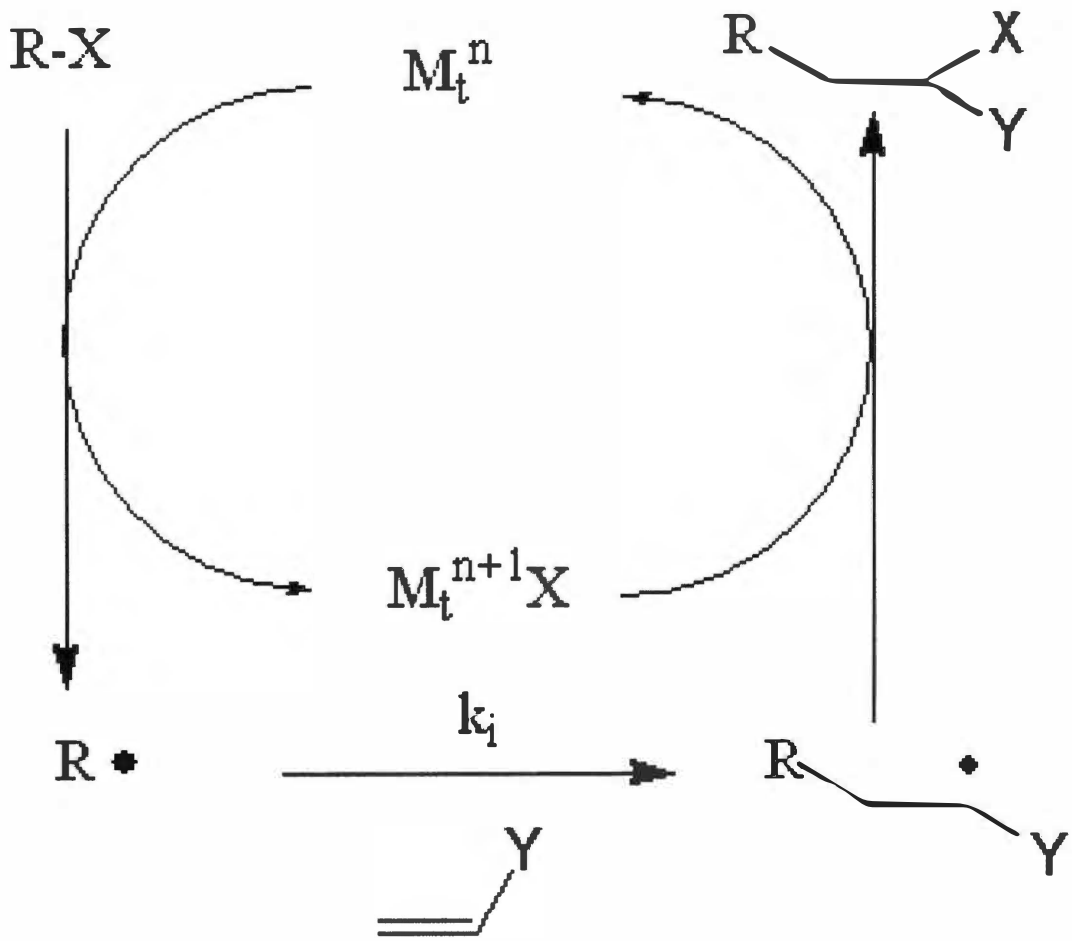


Figure 2.6 Reaction scheme for atom transfer radical addition, or ATRA

monomer, labeled M, to give the radical $P_1\cdot$. The subsequent reaction of $P_1\cdot$ with more monomer results in the growth of polymer chains, as shown by the reaction of $P_n\cdot$ with M in Figure 2.7. The final reactions to consider in the polymerization scheme result in the termination of the growing polymer chains. Disproportionation reactions[13] result from the abstraction of a H from polymer chain P_m by P_n, and combination reactions[13] occur when the two polymer chains bond to one another, forming a single chain, P_{n+m}.

If uncontrolled, the termination reactions can significantly broaden the distribution of polymer molecular weights,[55] but, since ATRP controls the production of free radicals in both the initiation and propagation steps, the loss of chains to the termination reactions is decreased significantly. As a result, ATRP can produce polymers with much narrower molecular weight distributions as compared to traditional free radical methods.

Random copolymers of methyl methacrylate (MMA) and 2,2,2-trifluoroethyl methacrylate (TFEMA) are synthesized via ATRP. The initiator that is employed in our reactions is phenoxy benzene-4,4′-disulfonyl chloride, or PDSC. The transition metal complex used as the catalyst is Cu(I)chloride complexed with 2,2′-bipyridine (bpy). An example of the initiation and propagation steps for the polymerization of MMAis shown in Figure 2.8. The molar ratios for a typical polymerization are 1 : 2 : 6 for PDSC : Cu(I) chloride : bpy[57] and 900 : 1 for the total monomer : PDSC ratio. All polymerizations are carried out in the bulk contained in a two-neck round-bottom flask.

The polymerizations, with the exception of the 19% TFEMA copolymer, are carried out in bulk with unfiltered monomers in a 150 mL, 2-neck round-bottom flask,

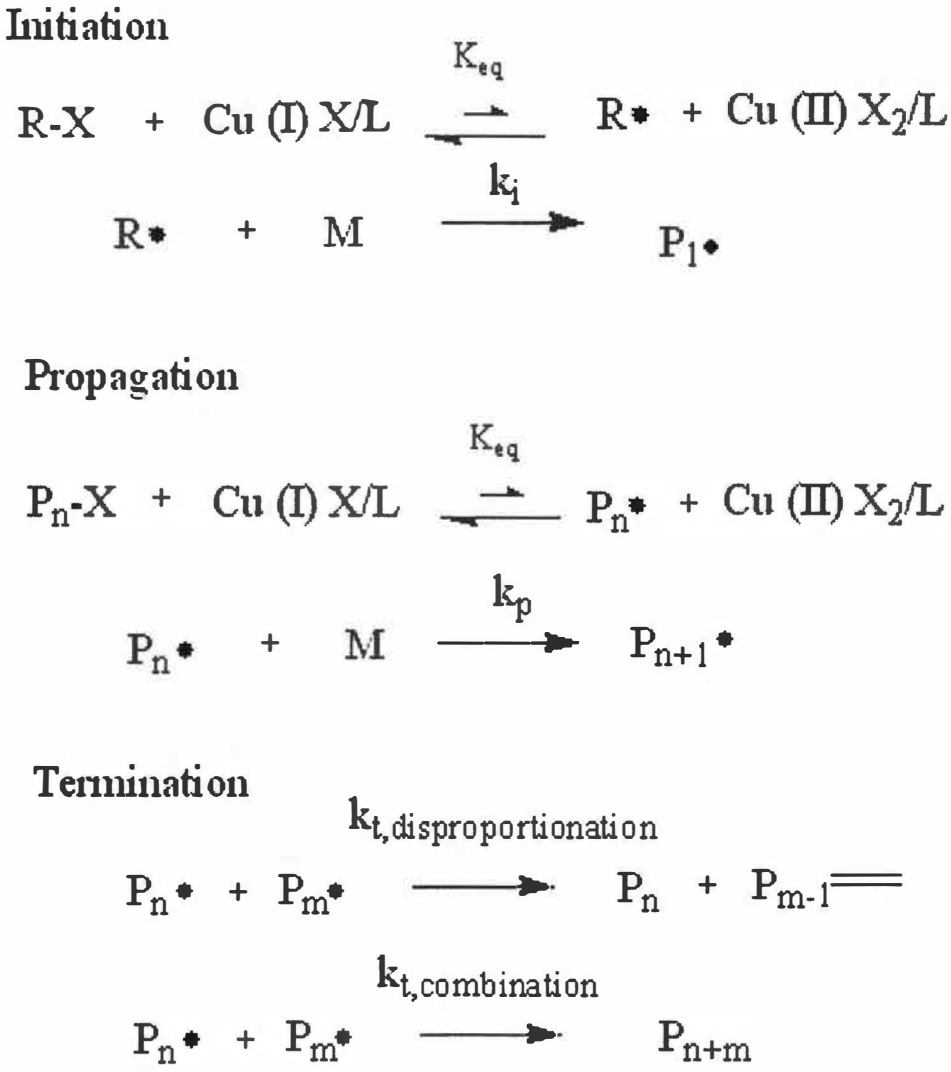


Figure 2.7 Polymerization via atom transfer radical polymerization, or ATRP

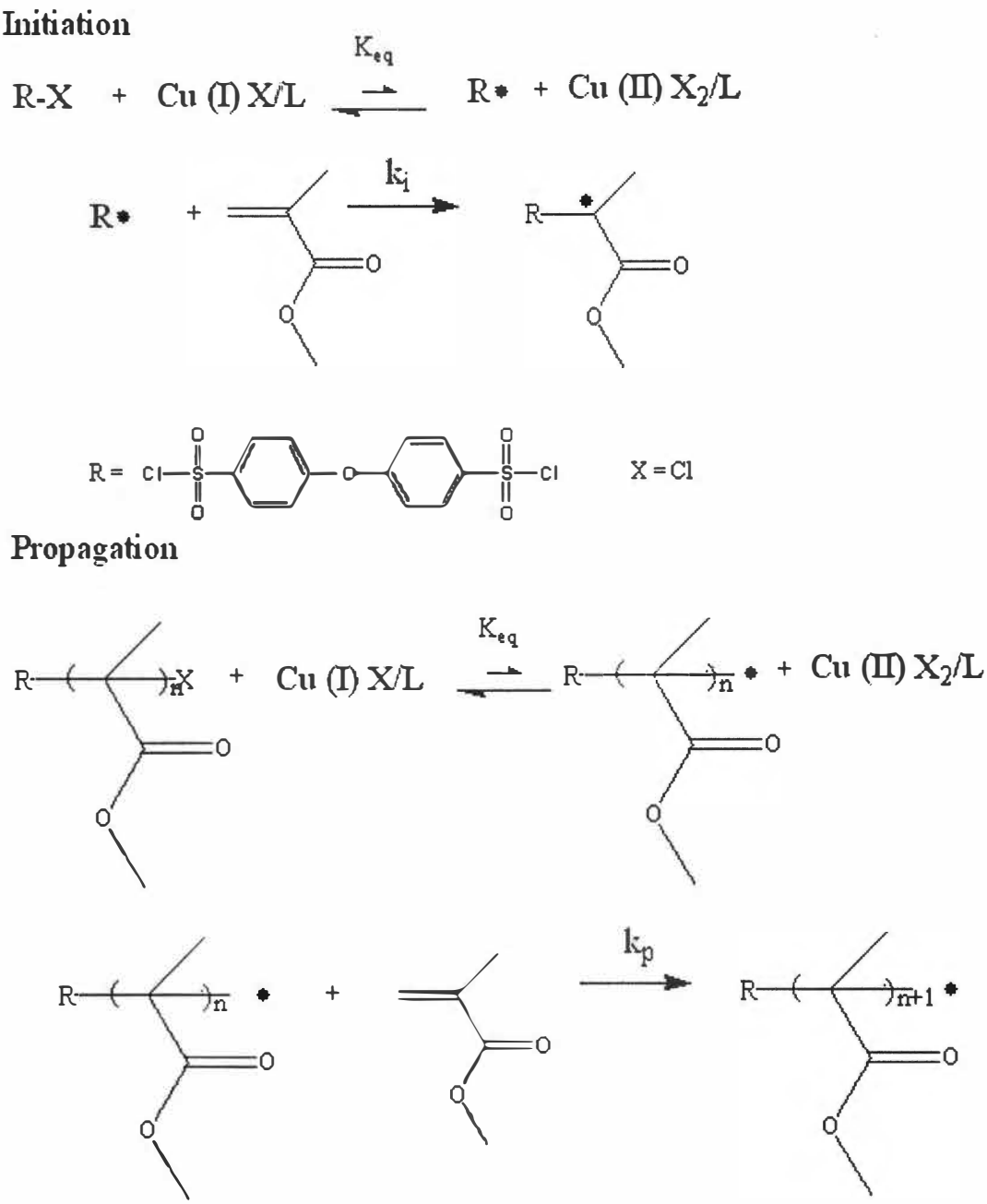


Figure 2.8 Initiation and propagation steps for poly(methyl methacrylate) as synthesized by ATRP

equipped with a magnetic stirrer and condenser, under a gentle flow of Ar gas. Before starting the reaction, the contents of the flask are de-gassed by freezing with liquid nitrogen and applying a vacuum. The contents are allowed to thaw under Ar flow, and the freezing/thawing process is repeated two more times. The reaction vessel is then placed in an oil bath that is heated to 95°C and allowed to react, with stirring, for eight hours. Over the course of the reaction, the contents of the flask undergo a color change, from green to brown, an indication that the catalyst is performing properly.[58] When the eight hour period has elapsed, the reaction is quenched by precipitating the contents of the flask into cold methanol. As a final note, when the fraction of TFEMA in the copolymer is increased (44 % or higher), nanopure water must be added to the methanol to improve recovery of the copolymer.

Characterization of copolymer composition is carried out on a Bruker AC300MHz ^{1}H-NMR[59] and is accomplished by dissolving the sample in $CDCl_3$. The methoxy peak for the MMA at 3.6 ppm and the $-CH_2-$ in TFEMA at 4.2 ppm is used to determine the %MMA using equation (E 2.5).[60] In this equation the A's are the area

$$\%MMA = (A_{MMA}/3)/[(A_{MMA}/3)+(A_{TFEMA}/2)] \quad (E\ 2.5)$$

under the peaks, and the %TFEMA is determined by simply subtracting the %MMA from 100%.

Molecular weights and polydispersity indexes (PDI's) for all polymers are determined by gel permeation chromatography (GPC) at room temperature (25 °C) and use a Waters 600E GPC that is equipped with a Waters 410 differential refractometer as the detector. The GPC is equipped with either Waters Styragel (HR-1, HR-3, HR-5E) or Polymer Labs Plgel 5μm mixed D columns and are calibrated using polystyrene

standards. GPC samples are prepared by dissolving the polymers in tetrahydrofuran (THF) to yield 0.2% by weight solutions. Samples are injected in 250μl quantities into the GPC with a 1 mL/min flow rate and THF as the mobile phase. The results of copolymer characterization can be found in Table 2.1.

Table 2.1 ATRP results for P(MMA-co-TFEMA) synthesis, * copolymer synthesized by C. P. O'Brien

% TFEMA	Moles of MMA ($1x10^{-2}$)	Moles of TFEMA ($1x10^{-2}$)	Moles of PDSC ($1x10^{-2}$)	Moles of CuCl ($1x10^{-2}$)	Moles of Bpy ($1x10^{-2}$)	% Yield	M_w ($1x10^4$)	PDI
8.3	9.35	0.491	0.0109	0.0219	0.0657	69.3	12.5	1.4
19	*	*	*	*	*	*	7.99	1.36
25.3	9.35	2.81	0.0163	0.0326	0.0976	68	8.01	1.39
44.3	5.61	2.81	0.00935	0.0187	0.0561	40.2	4.99	1.35
70.1	7.02	3.02	0.0165	0.033	0.0989	49.2	8.47	1.61

CHAPTER 3

Polymer Molecular Weight Effects on the Solubility of 8CB in PMMA Matrices

3.1

Introduction

In Chapter 1, a great deal of importance is placed on the solubility of the LC in the polymer matrix. This concern is well-founded since the ability of the LC to separate from the polymer matrix affects the efficiency and optical properties of the PDLC. One factor that is fundamentally important to the understanding of LC solubility is the effect of the polymer molecular weight on the PDLC phase behavior. Although experimental studies have laid the foundation for the current understanding of the role of polymer molecular weight on LC solubility, the number of these studies remain limited.[8,12,13]

Recent work by Gogibus and others[42] observe changes in the phase behavior of poly(siloxane) blends where increases in polymer molecular weight from 26,000 to 60,000 g/mol enlarge the immiscibility region of the phase diagram as well as the Flory-Huggins interaction parameter, χ. A more complete study on the effect of molecular weight on polymer/LC phase behavior is presented by Benmouna et al[23] on linear poly(styrene)/8CB blends with polymer molecular weights ranging from 4,000 – 200,000 g/mol. Determination of phase diagrams by optical microscopy show dramatic decreases in LC solubility as the poly(styrene) (PS) size increased. Calorimetry is also used in these studies to measure the change in the enthalpy of the 8CB liquid crystal phase transitions, which are used to determine the solubility limits for the LC in these mixtures. The solubility limits in this study indicating a "plateau" with increased PS molecular

weight, rather than a continual decrease. Moreover, when combined with similar data using poly(methyl methacrylate) (PMMA) as the matrix [19] it appears that the plateau in the solubility limits is independent of polymer structure.

There still remain significant questions regarding the importance of the polymer molecular weight on the phase behavior of polymer/LC blends. Although previous authors have studied the effect of polymer molecular weight on LC blends, the range of polymer molecular weights in these studies has been limited to a maximum of 2×10^5 g/mol. Since the phase behavior can still be dramatically altered by doubling or tripling polymer molecular weight beyond 100,000 g/mol,[61] any further studies of polymer/LC blends need to include molecular weights above 200,000 g/mol. Another issue concerns the arbitrary choices regarding the interaction parameter, χ, that the authors are forced to make when applying F-H theory to microscopy results. Therefore, the question is whether refinements can be made to the previous F-H approach that reflects some of the current understanding of polymer molecular weight effects on χ. Finally, the universal behavior proposed by Benmouna for solubility limits has been proposed to be independent of polymer composition in hydrocarbon-based polymer matrices as well as hold for molecular weights beyond 200,000 g/mol.[23] The confirmation of this behavior in polymer matrices with comparable molecular weight ranges but different compositions represents a useful tool in predicting solubility limits for untested polymer matrices.

The work presented in this chapter seeks to address these issues. Optical microscopy is used to determine the equilibrium phase diagrams of the LC 4′-octyl-4-biphenyl carbonitrile, 8CB, blended with linear poly(methyl methacrylate), PMMA. The weight average polymer molecular weight ranges from 32,000k – 600,000k g/mole. The

microscopy data is analyzed using Flory-Huggins theory, where the interaction parameter, χ, is extracted, which quantifies the miscibility of the LC in each polymer. Finally, the solubility limits are determined from DSC measurements for the polymer/LC blends studied to compare to previous results.

3.2

Experimental

Materials

All samples examined by microscopy and DSC consist of poly(methyl methacrylate) (PMMA) and a small molecule liquid crystal 4′-octyl-4-biphenyl carbonitrile (8CB). 8CB and PMMA (sold as $M_w \sim 120k$, 350k, 996k g/mol) are purchased from Aldrich Chemical Co and used as received. The lower molecular weight PMMA, 23k and 50k, are synthesized via atom transfer radical polymerization, ATRP in the bulk using phenoxy benzene-4,4′-disulfonyl chloride as the initiator and Cu(I) chloride complexed with 2,2′-bipyridine as the catalyst.[58] A list of the weight and number average molecular weights as well as the polydisperisities can be found in Table 3.1.

The blends are made by dissolving the desired weights of 8CB and PMMA in dichloromethane to give a 50 % by mass solution followed by casting onto a Teflon sheet. After drying for 24 hours at 60° C under vacuum slices from the films are used to make the microscopy and DSC samples.

Table 3.1. List of sources, the number and weight average molecular weights and polydispersities (PDI) for the poly(methyl methacrylate) polymers used in this study

Source	M_w	M_n	PDI
ATRP	32200	23200	1.39
	67200	54200	1.24
Aldrich	92700	62000	1.5
	335400	230200	1.46
	614900	258500	2.38

Microscopy

Determination of the equilibrium phase diagrams is accomplished by optical microscopy with an Olympus BH-2 microscope. The microscope is equipped with a cross-polarizer for the LC transitions as well as phase-contrast optics to detect the isotropic mixing. The samples cut from the films are mounted on clean glass slides with a Kapton spacer (~25μm) covered by a glass cover slip. A Mettler FP82HT heating stage with a Mettler FP90 Central Processor controls the temperature of the sample at a rate of 1°C/min.

Determination of Theoretical Phase Diagrams

Recall from the discussion of PDLC phase behavior, also in Chapter 1, that the free energy density of polymer/LC blends, see equation (E 3.1), is described as the sum of two components.[23] The first, f_i, defines the isotropic component due to the mixing,

$$f = f_i + f_a \qquad \text{(E 3.1)}$$

and the second, f_a, describes contributions from the anisotropic behavior of the LC when below the nematic-isotropic or nematic-smectic transition temperatures. Isotropic mixing of the LC with the polymer, f_i, is given by the Flory-Huggins theory, FH, for polymer solutions while the anisotropic free energy contributions from the coexistence of the polymer with LC in either the nematic or smectic phases, f_a, comes from Maier-Saupe-McMillan theory. It should be noted that the microscopy results presented here are primarily concerned with the mixing of the LC and polymer above N-I. Therefore, our calculations need not include the calculation of f_a from Maier-Saupe-McMillan theory. Once the relationship for the free energy density is established the chemical potentials can be calculated, see equations (E 3.2) and (E 3.3), where the subscripts denote the

solution component, $F = N_t f$ and the total number of lattice sites in the system, $N_t = N_1 n_1 + N_2 n_2$ ($N_x \equiv$ degree of polymerization, $n_x \equiv$ number of molecules). Expressing the

$$\mu_1 = (\partial F/\partial n_1)_{n2,T,P} \quad \text{(E 3.2)}$$

$$\mu_2 = (\partial F/\partial n_2)_{n1T,P} \quad \text{(E 3.3)}$$

chemical potentials in terms of volume fraction requires two assumptions (i) each LC/polymer segment occupies a single lattice site, and (ii) the blend is incompressible. Thus, if we define our volume fractions as $\phi_1 = N_1 n_1 / N_t$ and $\phi_2 = N_2 n_2 / N_t$, then the chemical potentials are given by equations (E 3.4) and (E 3.5). When the system

$$\mu_1/N_1 = f - \phi_2(\partial f/\partial \phi_2) \quad \text{(E 3.4)}$$

$$\mu_2/N_2 = f - \phi_1(\partial f/\partial \phi_1) \quad \text{(E 3.5)}$$

reaches equilibrium, any coexisting phases have the same chemical potential. For example, two phases that are either rich or poor in component 1, denoted by primes in equation (E 3.6), have the same chemical potential. By inserting the relationship

$$\mu_1' = \mu_1'' \quad \text{(E 3.6)}$$

from (E 3.4) into (E 3.6), the equality of the first derivatives of the free energy with respect to composition at equilibrium is established by equation (E 3.7). The formulation

$$(\partial f/\partial \phi_2)' = (\partial f/\partial \phi_2)'' \quad \text{(E 3.7)}$$

of (E 3.7) means that the thermodynamic description from F-H can be used to determine coexistence curves for comparison to the optical microscopy results.

The isotropic free energy density for the LC/polymer blends comes from F-H, equation (E 3.8) where k_B is the Boltzmann constant, and χ is the F-H interaction

parameter. The first two terms in (E 3.8) represent the entropy of mixing while the final term yields the enthalpy of mixing. In F-H theory the coexistence curve is determined

$$f/ k_BT = \phi_1/N_1 \ln\phi_1 + \phi_2/N_2 \ln\phi_2 + \chi\, \phi_1\phi_2 \qquad \text{(E 3.8)}$$

from the first derivative of the free energy, which corresponds to the chemical potential, given in (E 3.9).

$$\partial f/\partial\phi_1 = (\ln\phi_1 + 1)/N_1 - (\ln\phi_2 + 1)/N_2 + \chi(\phi_1 - \phi_2) \quad \text{(E 3.9)}$$

An example of the construction of the coexistence curves from (E 3.9) is depicted in Figure 3.1 where (E 3.9) is plotted as a function of the LC volume fraction, ϕ_1, for a single temperature. The LC fractions that are marked with the primes are connected by a tie line, and the areas of the top and bottom portions of the curve, shown as the shaded portions of the graph, are determined. If the two phases are at equilibrium, the sum of the areas should equal zero. In practice, though, a sum of zero area can not be exactly determined but is approached through an iterative process of choosing several different compositions, integrating the areas, and finding the result that is closest to zero. Before using (E 3.9), however, we must determine the effective segment lengths for N_1 and N_2 as well as the interaction parameter, χ.

Determining the effective segment lengths, N_1 and N_2, for both the LC and the polymer is accomplished in the following manner.[23,62] Since the LC defines the volume of the lattice sites, the segment length of the LC, N_1, is given a value of 1. The segment length of the polymer, N_2, can be found by first obtaining a good fit of Flory-Huggins theory to a single set of microscopy data, in this case for the 90k g/mol PMMA. The fraction of the LC that corresponds to maximum temperature from the phase diagram,

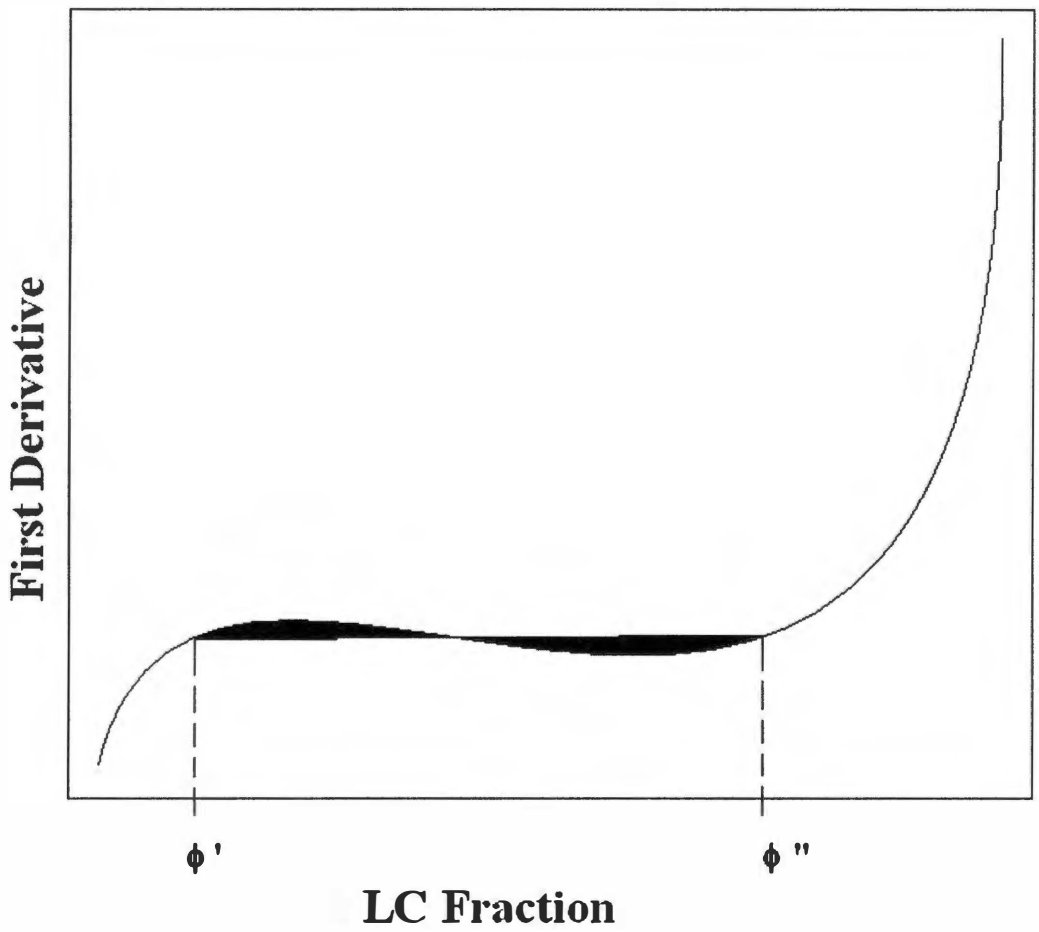


Figure 3.1 Illustration of the first derivative of the Flory-Huggins free energy versus LC fraction that is used to determine theoretical coexistence curves. The two fractions, denoted by the primes, are the LC-poor and rich compositions at equilibrium.

ϕ_{max}, is taken to be the critical LC fraction, $\phi_{critical}$, so that $\phi_{max} \approx \phi_{critical}$. Estimation of N_2 is accomplished by using the relationship $\phi_{critical} = N_2^{1/2}/(N_2^{1/2} + N_1^{1/2})$ from Flory-Huggins theory. The value for N_2 is then used to determine the polymer segment size by dividing the M_n value for the polymer by N_2. The polymer segment size is found to be approximately 10,000 g/mol, a size that is on the order of that in previous studies.[23]

Included in our analysis of the phase behavior is the need to quantify the changes in LC solubility by extracting the interaction parameter, χ. The link between χ and solubility can be seen by expanding the interaction parameter of the enthalpy term in (E 3.8), given in (E 3.10).[17-18] The enthalpy of mixing, ΔH_m, in this case is described by

$$\Delta H_m/N = \tfrac{1}{2}\, z\Delta W\phi_1\phi_2 \qquad \text{(E 3.10)}$$

the exchange energy between neighbors, ΔW, occupying N lattice sites where z gives the coordination number of the nearest neighbors and the volume fractions of the two components are given by the ϕ's. Since the mixing of the two components requires overcoming the energetic barrier to mixing, the solubility is linked to the energy, ΔW, and the number of nearest neighbors, z. F-H theory equates χ to the energy changes outlined above.

The determination of χ in our fitting procedure starts with the simple relationship that is shown in equation (E 3.11). Here A and B are adjustable parameters while T is

$$\chi = A + B/T \qquad \text{(E 3.11)}$$

the absolute temperature. In polymer/LC blends the phase behavior typically exhibits an upper critical solution temperature, UCST where the $A < 0$, $B > 0$.[16] For the A and B parameters we begin by first calculating χ_c from the critical region using the DP for the polymer and the LC, see equation (E 3.12). At this point a choice must be made for A.

$$\chi_c = (N_1^{-1/2} + N_2^{-1/2})^2/2 \qquad \text{(E 3.12)}$$

We base our choice on the previous study of Benmouna et al[23] for polystyrene with a molecular weight of 200,000 g/mol, A = -4.5. The calculation of B proceeds from (E 3.11) using the critical values of χ as well as temperature, T, from microscopy results. In all the fits covered by our experiments we keep B as a constant while A is allowed to vary.

The justification for our choices of A and B is made clearer through a physical explanation of χ. The original view of F-H ascribes χ to a purely enthalpic role to mixing, however, such a limitation renders F-H incapable of even a qualitative description of the phase behavior.[18] Attempts to correct the original theory can be found in the pioneering works of Flory, Prigogine, and others[18, 62-68] where χ is corrected by imposing empirical composition dependences on the parameter. However, the purely compositional approach creates difficulties when trying to link χ with physically meaningful quantities. The solution to this problem comes from the work of Koningsveld and Kleintjens[65] who describe χ as a free energy parameter that is split into two different contributions. The term B is attributed to the enthalpic contributions arising from the exchange energy from inter-/intra-molecular contacts. The entropic term, A, accounts for all other sources of non-combinatorial entropy such as the change in molecular packing that must occur before solution components mix. Since the chemical composition of the matrix remains the same throughout our experiments the exchange energies between 8CB and the PMMA segments should not vary significantly, hence B is held constant in our calculations. Since the chemical composition of the matrix remains the same throughout our experiments the exchange energies between 8CB and the PMMA segments should

remain the same, hence B is held constant in our calculations. A is allowed to vary, as changing the PMMA molecular weight alters the number of polymer segments that in turn may alter such factors as the packing of the PMMA and LC's, which would alter the way the solution components pack, altering the non-combinatorial entropy contribution to the mixing. Thus, in accounting for the molecular weight dependence of χ, the value of A is allowed to vary with molecular weight. This analysis allows a more thorough interpretation of the important parameters that influence the thermodynamics of polymer/LC mixtures.

Solubility Limits

In the original works by Smith and co-workers, differential scanning calorimetry (DSC) studies of PDLC's find that complete separation of the LC from the polymer matrix never occurs. Rather, a percentage of the LC remains trapped within the polymer matrix and acts like a plasticizer. The consequence of the trapped LC is a reduction in the phase-separated LC, a condition that not only affects the potential cost of the PDLC but also the final morphology of the LC droplets. As a result, the determination of the amount of trapped LC becomes a fundamentally important parameter to the construction of PDLC's.

Smith and Vaz[21] show experimentally that the fraction of the phase-separated LC, α, can be determined by measuring the transition enthalpy from the integration of the nematic-isotropic phase transition that is measured during the DSC experiment (per unit mass) at the nematic-isotropic transition of the pure LC, or $\Delta H_{N\text{-}I}$. The fraction, α, is defined by the simple relationship in equation (E 3.13), where $m_{LC,droplets}$ is the mass of the phase-separated LC in the droplets and $m_{LC,\,total}$ is the total mass of the LC in the

$$\alpha \equiv m_{LC,droplets} / m_{LC,\,total} \qquad \text{(E 3.13)}$$

PDLC. The authors relate α to $\Delta H_{N\text{-}I}$ of the PDLC by equation (E 3.14).

$$\alpha = (1 + m_p/m_{LC,\,total})\, P(x) \qquad \text{(E 3.14)}$$

Here m_p is the mass of the polymer in the PDLC, x is the LC concentration, and P(x) is the ratio of the $\Delta H_{N\text{-}I}$ for the PDLC to that of the pure LC, as shown in equation (E 3.15).

$$P(x) = \Delta H_{N\text{-}I,PDLC} / \Delta H_{N\text{-}I,\,LC} \qquad \text{(E 3.15)}$$

Since $\Delta H_{N\text{-}I}$ shows a linear decrease with LC content, Smith[21] is able to show experimentally that P(x) decreases linearly. The authors[20-22] relate P(x) to the LC that remains trapped in the polymer matrix by assuming the following:

1. Only the phase-separated LC contributes to the measured $\Delta H_{N\text{-}I}$.
2. There is a maximum mass of LC that can be absorbed by a given polymer matrix.

The first assumption means that when all of the LC is trapped in the matrix $\Delta H_{N\text{-}I}$ would equal zero and, hence, P(x) would also be zero. As for the second assumption, the maximum mass of the trapped LC means that the polymer matrix is completely saturated at a fraction, β, of the total LC content. Since β is the maximum amount of LC that can be absorbed by the polymer, it defines the limit of LC solubility in the polymer matrix and is called the solubility limit. As a result of these assumptions, P(x) is related to the total fraction of the LC, x, and the solubility limit, β, by equation (E 3.16).

$$P(x) = (x - \beta)/(1 - \beta) \qquad \text{(E 3.16)}$$

Although the experimental DSC evidence makes a strong case for the legitimacy of β, Smith adds further support by developing a thermodynamic basis for the solubility

limit.[22] F-H theory, in this case, provides the theoretical means to determine the polymer composition in the LC-rich, ϕ_{LC}, and polymer-rich, ϕ_{Pol}, phases. By using the ratios of the total volume of the PDLC, V_{total}, to that occupied by the LC and the polymer in the PDLC, V_{LC} and V_{Pol}, Smith is able to derive an analogous relationship to P(x), called $\Pi(\phi)$, for the F-H compositions, see equations (E 3.17) and (E 3.18). Since the

$$\Pi(\phi)_{LC} \equiv V_{LC}/V_{total} = (\phi_{Pol} - \phi)/(\phi_{Pol} - \phi_{LC}) \qquad \text{(E 3.17)}$$

$$\Pi(\phi)_{Pol} \equiv V_{Pol}/V_{total} = 1 - \Pi(\phi)_{LC} = (\phi - \phi_{LC})/(\phi_{Pol} - \phi_{LC}) \qquad \text{(E 3.18)}$$

densities of the LC and the polymer matrix are often very similar, the volume fractions that are used in the calculation of $\Pi(\phi)$ can be directly compared to the mass fractions that are used in P(x). As a result, Smith is able to calculate both α and β, and when the theoretical results are compared to the experimental data, good agreement between the two is observed.

In order to test the proposed universal behavior of β for hydrocarbon polymers, DSC measurements are obtained using a Mettler-Toledo 821e. Samples from the same films that are used in the microscopy experiments are made by placing 4-10mg of the blend into 40μL aluminum DSC pans. The samples were heated from 25 - 70°C at a rate of 1°C/min and are repeatedly analyzed until each sample shows a consistent reading at least three times. ΔH_{N-I} of 8CB for all samples is obtained by integrating the N-I transition in the DSC thermogram[20-22] and normalizing ΔH_{N-I} to the total sample mass. The normalized ΔH_{N-I} is plotted versus the weight fraction of 8CB in the sample, and the extrapolation of the normalized ΔH_{N-I} to zero determines the solubility limit, β, of 8CB.

3.3

Results

A typical example of the experimentally determined phase diagrams for the PMMA/8CB blends is shown in Figure 3.2 for PMMA with a molecular weight of 92,000. The smectic-nematic as well as the nematic-isotropic transitions for 8CB appear at approximately 32°C and 41°C respectively for all blends in this study. The isotropic mixing transition is shown by the upper set of data points in each graph. Comparison of the isotropic mixing data for all PMMA molecular weights studied can be found in Figure 3.3. A steady increase in the mixing temperatures is observed with increasing molecular weight for 32k to 90k, however, between 90k and 600k the change in mixing temperatures becomes minimal.

Flory-Huggins theory is fit to the microscopy data as described in the experimental section, and these fits are shown in Figures 3.4 and 3.5. Figure 3.4 shows the result where χ is determined for the 95,000 g/mol sample and then the coexistence curves of all other blends are calculated using Flory-Huggins theory accounting for the change in molecular weight but with the same χ. Figure 3.5 displays the fits when the B portion of χ is held constant but A changes with molecular weight. The χ_c values that are used to create the theoretical coexistence curves are presented in Table 3.2. Note the lack of agreement between the data and the theoretical coexistence curves in Figure 3.4 for all molecular weights other than 90,000. Clearly a χ that is independent of molecular weight does not accurately describe this system. Figure 3.5, however, presents the fits to Flory-Huggins theory, where χ is allowed to vary with molecular weight.[69-71] The rationale for

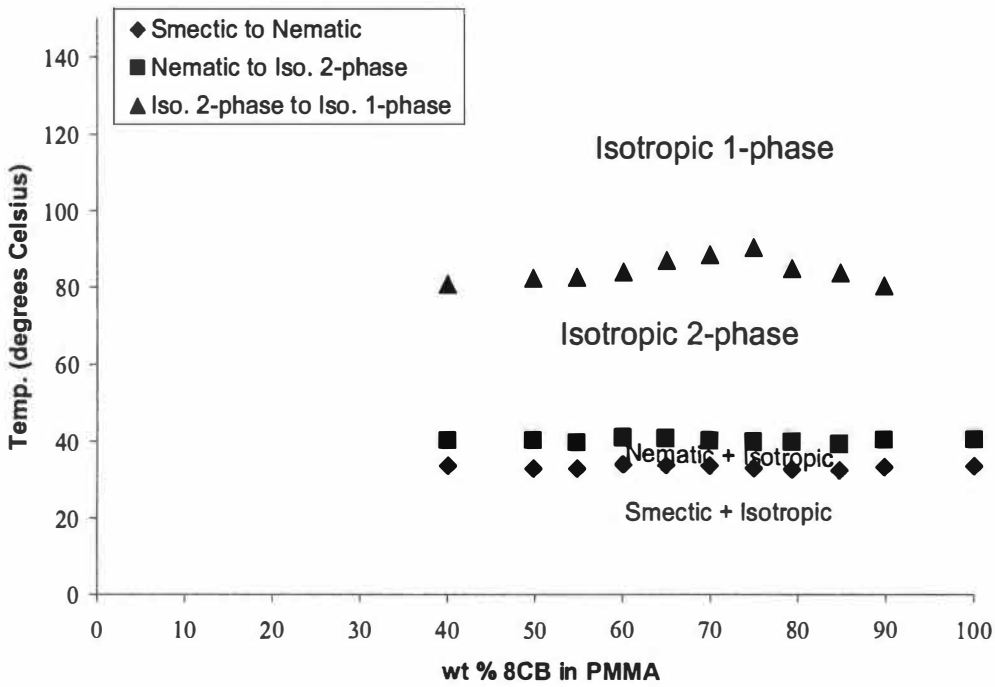


Figure 3.2 Typical phase diagram for PMMA/8CB blends, PMMA M_w = 90,000 g/mol; (◆) Smectic to nematic transition, (■) Nematic to isotropic transition, (▲) Isotropic mixing transition

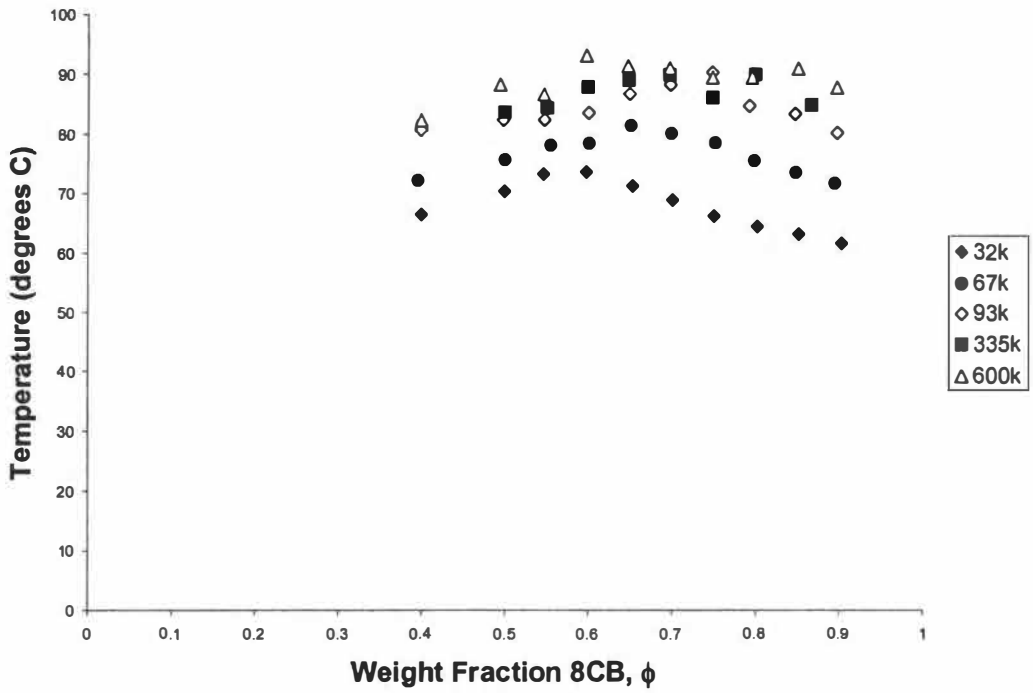


Figure 3.3 Microscopy data for isotropic mixing of PMMA with 8CB for all PMMA weight average molecular weights, (◆, lower) 32,200 g/mol, (●) 67,200 g/mol, (◆, upper) 90,000 g/mol, (■) 335,000 g/mol, (▲) 600,000 g/mol

Table 3.2 Values for the polymer segment lengths, N_2, critical fraction, ϕ_c, and the critical interaction parameter, χ_c, extracted from the microscopy data; Effective segment size for N_2 determination ca. 10,000 g/mol.

Molecular weight	N_2	ϕ_c	χ_c
32200	3	0.634	1.24
67200	6	0.710	0.992
92700	8	0.749	0.889
335400	33	0.852	0.689
614900	61	0.886	0.636

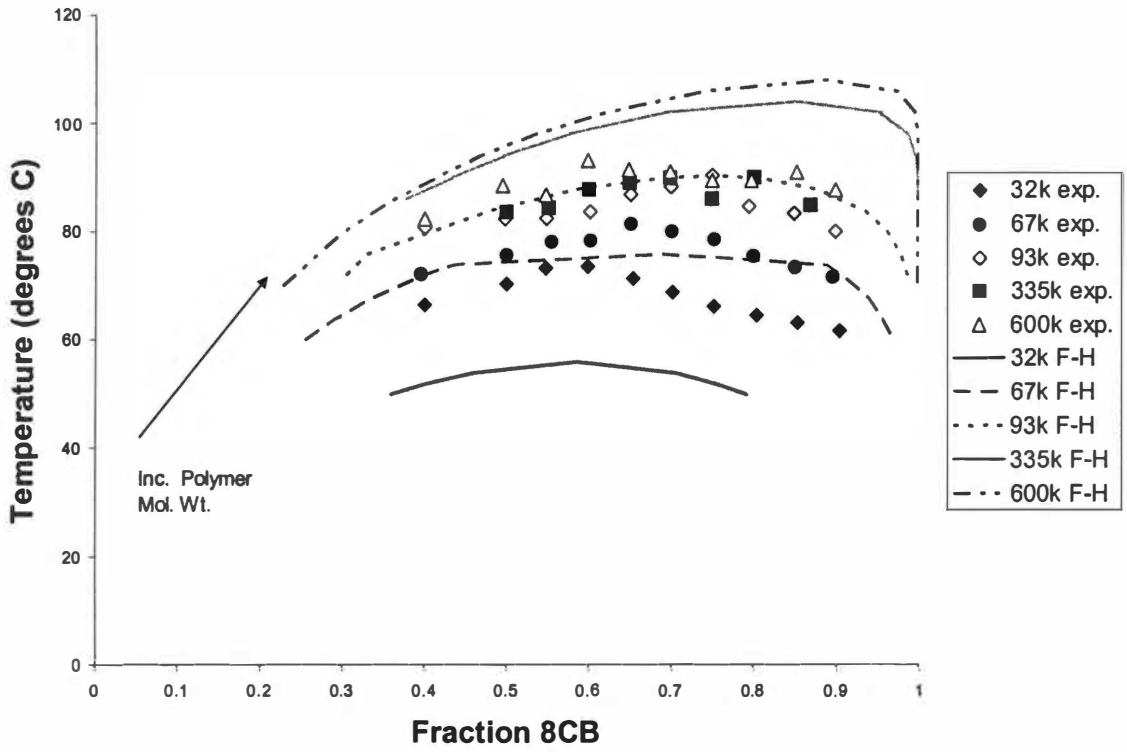


Figure 3.4 Initial fits of microscopy data for the isotropic mixing transition to F-H; χ has no molecular weight dependence; (◆, lower) 32,200 g/mol, (●) 67,200 g/mol, (◆, upper) 90,000 g/mol, (■) 335,000 g/mol, (▲) 600,000 g/mol

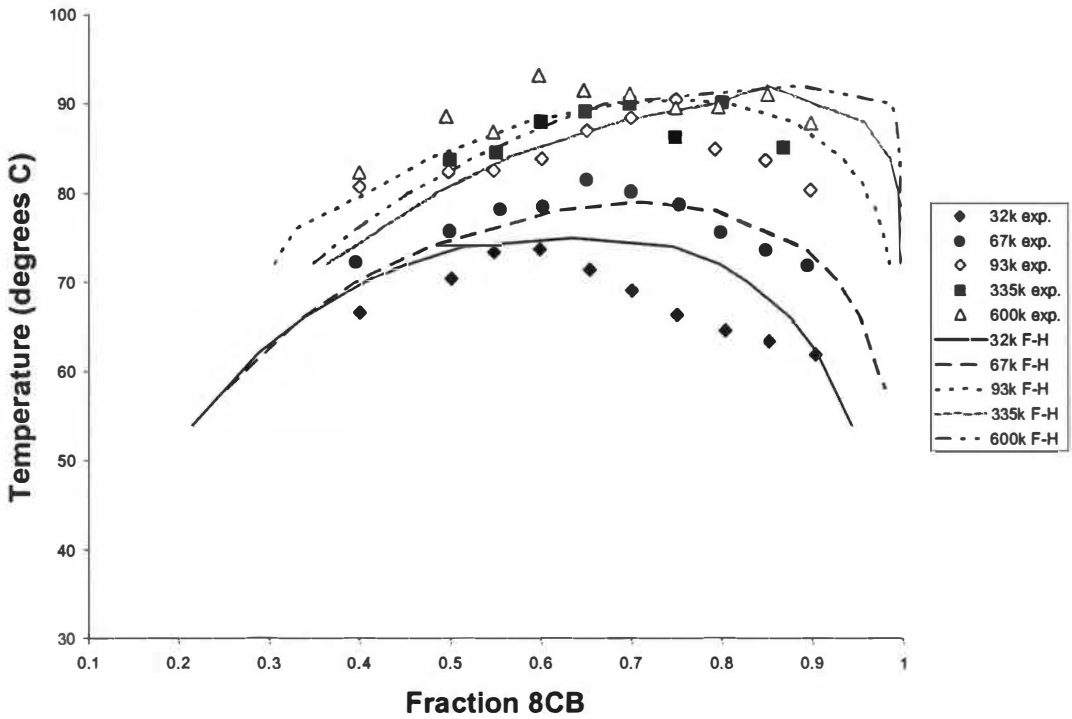


Figure 3.5 Fits of microscopy data for the isotropic mixing transitions to F-H, where χ scales with M_w; (◆, lower) 32,200 g/mol, (●) 67,200 g/mol, (◆, upper) 90,000 g/mol, (■) 335,000 g/mol, (▲) 600,000 g/mol

adopting the molecular weight dependence of χ in the fits is guided by the fact that there is experimental evidence of a molecular weight dependence of χ.[69,70] Moreover, by fitting the phase behavior data of each blend to Flory-Huggins and extracting values of χ, the effect of polymer molecular weight on the phase behavior can be quantified. This quantification is shown in Figure 3.6, which is a log-log plot is χ vs. molecular weight at 60 °C. The overall trend in the scaling of χ in Figure 3.6 indicates that $\chi \sim M_w^{-0.1}$ in this system. Moreover, when χ is allowed to depend on the molecular weight, the Flory-Huggins theory fits the experimental data very well for all PMMA molecular weights.

The solubility limits of 8CB in the polymers studied are determined by DSC and presented in Figures 3.7, 3.8, and 3.9. Figure 3.7 shows a typical set of DSC thermograms for the 90,000 molecular weight that are arranged top-to-bottom for pure 8CB to 40% 8CB. The smectic-nematic transition for 8CB is observed as a small endotherm between 31 and 32°C for the pure 8CB through 70% 8CB blend. The nematic-isotropic transition is shown as the large endotherm, enclosed by brackets, and shows a decreasing trend with 8CB content. Figure 3.8 shows typical data that quantifies the solubility limit, β, for the blends containing PMMA with 90,000 molecular weight. The x-intercept at $\Delta H_{N-I} = 0$ of these plots provides the solubility limit for 8CB in the PMMA matrix. The data in Figure 3.9 (the diamonds are from Benmouna et al for PS/8CB blends) [23] show the molecular weight dependence of β. This data indicates that β decreases with increase molecular weight up to ca. 100,000 and then plateaus to an LC fraction at approximately 0.4, and generally agrees with previously reported data.[23]

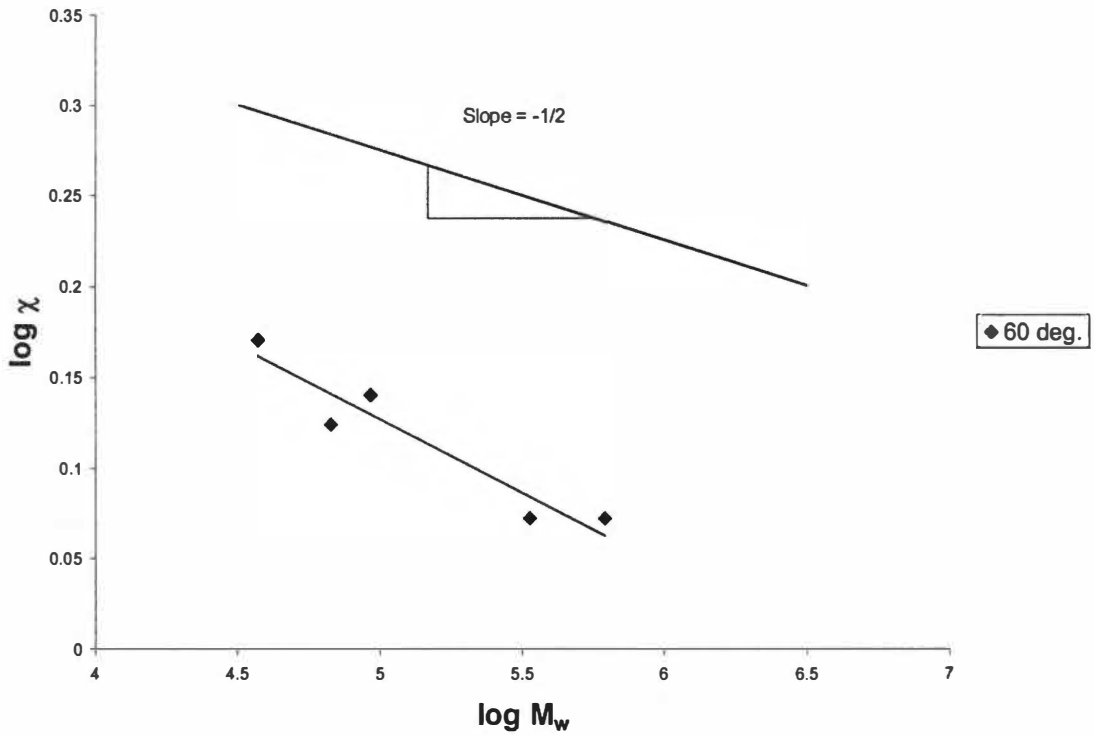


Figure 3.6 Comparison of the scaling of extracted χ values at 60°C to mean-field prediction of $\chi \sim M_w^{-0.5}$

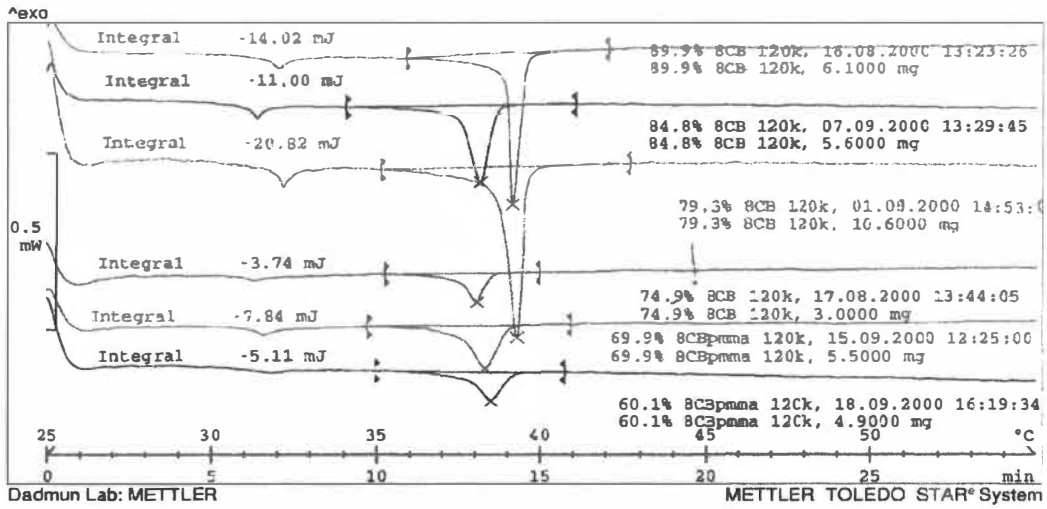


Figure 3.7 Typical set of DSC thermograms for 90,000 g/mol PMMA blend arranged in order of decreasing LC content. Portion in brackets is the nematic-isotropic transition of 8CB. Integration for each blend is the value on the far right.

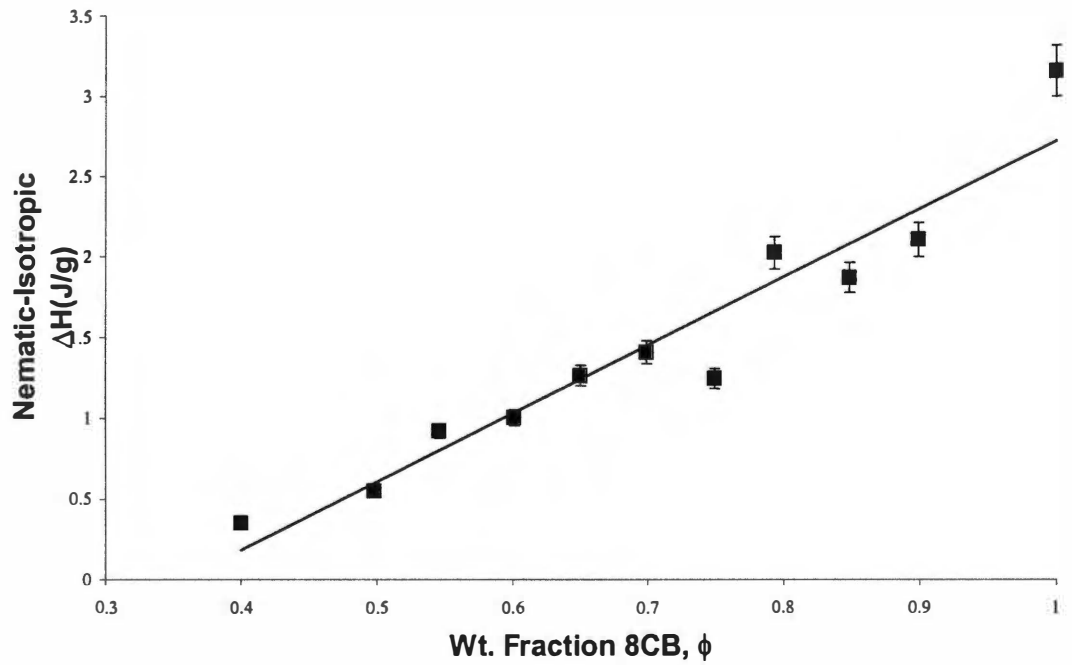


Figure 3.8 Typical DSC results for ΔH_{N-I} used to extrapolate β, PMMA M_w = 90,000 g/mol; x-intercept yields β, the solubility limit

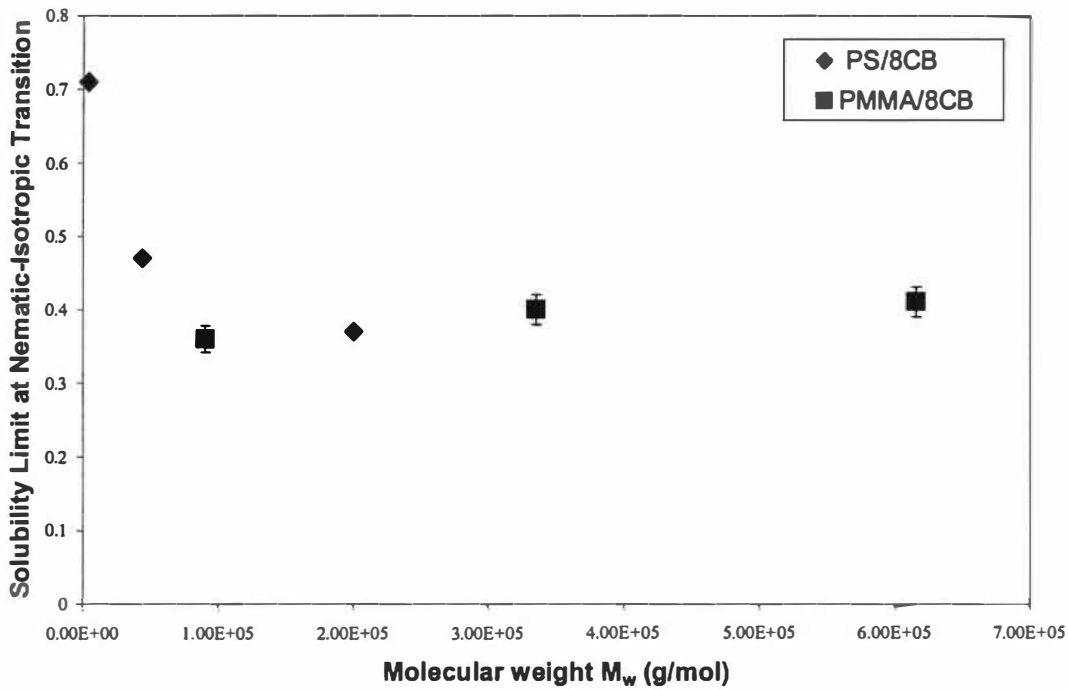


Figure 3.9 Comparison of solubility limits; (◆) from Benmouna et al for PS/8CB blends, (■) solubility limits from this study

3.4

Discussion

The data shows that as the chain length of a polymer increases, the miscibility of the polymer with a liquid crystal decreases as expected. However, when poly(methyl methacrylate) becomes larger than ~100,000, which corresponds to a degree of polymerization of approximately 1,000, an increase in polymer molecular weight does not significantly change the miscibility curve. This result is the first time such a limit has been observed experimentally for polymer/LC systems.

The extraction of χ from the microscopy data provides a method to quantify this limiting molecular weight behavior observed in the phase diagrams. χ can be expected to scale with molecular weight, which originates from corrections to F-H theory.[16,18,70-73] These corrections predict that $\chi \sim M_w^{-0.5}$. However, from Figure 3.7, the experimental data show scaling of $\chi \sim M_w^{-0.1}$. One possible explanation for this dependence is provided by theories that account for the volumetric differences of the LC molecules relative to the polymer segments.[68] The basic framework of F-H model assumes that each lattice site is represented by a uniform volume within the solution, no matter if the site is occupied by polymer segment or LC molecule. For this assumption to hold in our blends both the PMMA segments and the 8CB molecules would have to occupy similar volumes. However, given the rigidity of the 8CB molecule as compared to the more flexible PMMA segments such a condition is unlikely. An explanation of the observed scaling behavior must include a description that retains the essential features of the F-H approach but accounts for the deviations arising from structural asymmetry.

Recent studies by Dudowicz et al[75] explore the effect of molecular structure on the scaling behavior of such F-H parameters as critical temperature, T_c, and volume fraction, ϕ_c, by a simplified lattice cluster theory, or SLCT. The "simplification" in this case is performed by taking the regular lattice cluster theory, a description that corrects the F-H free energy of mixing for changes caused by different molecular structures, and imposing high-pressure conditions that remove compressibility contributions. In this way the authors are able to isolate the entropic changes arising from the intermolecular packing, as well as make comparisons of the scaling behavior from their SLCT calculations to the predictions of F-H.

The SLCT calculations result in four separate miscibility classes that exhibit different scaling behavior of the critical parameters, T_c and ϕ_c, with polymer molecular weight. In one of these miscibility classes, $T_c \sim N$, and ϕ_c follows the same relationship that is stated in the experimental section of this chapter. However, the authors find that, in changing the basic molecular shapes of the mixing components, ϕ_c shows an additional weak dependence on N, but T_c begins to show complex molecular weight dependencies that deviate dramatically from the corrections to F-H theory. Since the χ values extracted from our microscopy data derive from the critical temperature, it is obvious that this complex scaling of T_c with N will impact the dependence of χ on M_w and lead to scaling of χ with M_w that deviates from $\chi \sim M_w^{-0.5}$ due to structural dissimilarities of the mixing components. Unfortunately, it is beyond the scope of this work to derive the $\chi \sim M_w^{-0.1}$ scaling behavior using SCLT but is presented here as a basis for future work.

The second goal of our study is to determine the solubility limit, β, for PMMA/8CB blends with increasing polymer molecular weight as well as compare the results with the universal curve. Experimental results given in Figures 3.8 and 3.9 represent, to our knowledge, the first such study performed on PMMA/8CB blends. From the data obtained by DSC we see the leveling off of β with increasing PMMA molecular weight at ca. 0.40 8CB weight fractions. In Benmouna's study,[23] of PS/8CB blends the presence of this plateau is attributed to the formation of a strongly entangled physical network that prevents further separation of the LC from the polymer matrix. By extending the data to molecular weights beyond 100k the comparison of our data to the universal curve supports the limiting molecular weight hypothesis. Additionally, the similarity between β values of PS/8CB blends and our PMMA/8CB blends lend further support to independence of solubility limits to polymer composition.

3.5

Conclusions

The UCST of a blend of poly(methyl methacrylate) and 8CB increases significantly with polymer chain length if the degree of polymerization of the polymer is less than ca. 1,000. Above a DP of 1,000, the UCST barely increases with polymer chain length. This limiting molecular weight dependence is captured quantitatively by allowing the Flory-Huggins interaction parameter, χ, to scale with polymer molecular weight to the -0.1 power. This power law dependence may be explained in terms of the structural differences between the PMMA segments and 8CB molecules. This power law dependence and limiting molecular weight behavior has not been previously presented in

the literature for linear acrylate matrices and represent an important contribution to the understanding of the impact of polymer molecular weight on the phase behavior of PDLC's

The solubility limit, β, of the PMMA/8CB blends are also presented. As PMMA molecular weight increases, β reaches a plateau of 40% wt 8CB, an indication the polymer-rich phases are saturated with LC at high molecular weights. Comparison of the results with Benmouna's data[23] strengthens the argument that the solubility limit of an LC in a polymer matrix plateaus for high molecular weights as well as the universality of this behavior of LC and coiled, hydrocarbon polymer mixtures.

CHAPTER 4

The Consequence of Matrix Fluorination on Liquid Crystal Solubility in Polymer Dispersed Liquid Crystals

4.1

Introduction

Several factors affect the performance of PDLC devices, but three factors in particular, the solubility of the LC, the refractive index of the polymer matrix, and the anchoring of the LC[3-6] at the droplet interface are particularly important in the design and construction of PDLC devices. LC solubility, as stressed in Chapters 1 and 3, affects not only the final cost of the PDLC device but also its electro-optical properties by changing LC domain morphology. The refractive index affects the choice of the polymer matrix, since the transparent mode of PDLC's requires that the refractive indexes of both the LC and the polymer matrix match as closely as possible.[3-6] LC anchoring, a concept introduced in Chapter 1,[3,5,9-11] is caused by the alignment of the LC molecules along the droplet walls, formed by the polymer matrix, and is responsible for increased switching voltages.

A promising method to improve refractive index matching, LC phase separation, and LC anchoring is to incorporate fluorinated monomers into the matrix material.[76-78] The refractive index of transparent fluorinated polymers has long been known to be lower than those of protonated polymers and originates from the nature of the carbon-fluorine bond.[79] By lowering the refractive index, the transparency of the polymer matrix is increased, and can provide a mechanism for the refractive index to match the LC when the PDLC is in transparent mode. In addition to improved optical properties, the

presence of fluorinated moieties within polymers reduces the miscibility of the polymer and the LC, thus minimizing the LC that remains dispersed in the polymer matrix, i.e. the solubility limit of the LC in the polymer. As a result, PDLC's that are constructed with fluorinated polymer matrices should increase the amount of phase-separated LC. The use of fluorinated matrices also has the potential to reduce anchoring of the LC on the droplet wall because of repulsion between the fluorine–containing monomers and the polar "heads" of the LC molecules. This reduction in anchoring can potentially lower the switching voltages needed to induce changes in the LC and increase PDLC efficiency.

Despite the potential advantages of using fluorinated polymers in PDLC construction, the number of studies that use these polymers remains relatively few, and some fundamental questions still persist. The improvement of the electro-optical properties, such as the improved transmission of light and refractive index matching has been observed by Yamada et al.[80] In addition to the optical response, improved switching voltages have been observed, again, by Yamada et al as well as DeSarkar, Schulte, and others. As for the decrease in LC solubility, the presence of larger LC domains from scanning electron microscopy studies supports this argument.[76-78] However, since the studies that are mentioned here mainly focus on PDLC devices, the consequences of fluorinated polymer matrices on the phase behavior of PDLC's have yet to be addressed.

The goal of this chapter is to answer some of the fundamental questions regarding the impact of polymer matrix fluorination on LC solubility in PDLC's. In order to accomplish this goal, coploymers with controlled percentages of methyl methacrylate (MMA) and 2,2,2-trifluoroethyl methacrylate (TFEMA) are synthesized and blended with the LC, 8CB. By using copolymers with controlled, well-characterized

compositions, the changes in LC solubility, as determined form the phase behavior can be directly linked to the TFEMA content. Optical microscopy is used to study the phase behavior, and in a similar strategy to the one used in Chapter 3, the changes in solubility are quantified by Flory-Huggins interaction parameter χ that is obtained through the determination of theoretical phase diagrams by the Flory-Huggins theory for polymer solutions.

4.2

Experimental

Copolymer Synthesis

Copolymers of methyl methacrylate (MMA) and 2,2,2-trifluoroethyl methacrylate (TFEMA), see the chemical structures in Figure 4.1,[77] are synthesized via atom transfer radical polymerization, as discussed in Chapter 2. The initiator that is employed in this reactions is phenoxy benzene-4,4′-disulfonyl chloride, or PDSC. The transition metal complex used as the catalyst is Cu(I)chloride complexed with 2,2′-bipyridine (bpy). The molar ratios for a typical polymerization are 1 : 2 : 6 for PDSC : Cu(I) chloride : bpy[57] and 900 : 1 for the total monomer : PDSC ratio. All polymerizations are carried out in the bulk contained in a two-neck round-bottom flask.

The polymerizations, with the exception of the 19% TFEMA copolymer synthesized by C.P. O'Brien, are carried out in bulk with unfiltered MMA and TFEMA monomers, added simultaneously, in a 150 mL, 2-neck round-bottom flask, equipped with a magnetic stirrer and condenser, under a gentle flow of Ar gas. Before starting the reaction, the contents of the flask are de-gassed by freezing with liquid nitrogen and

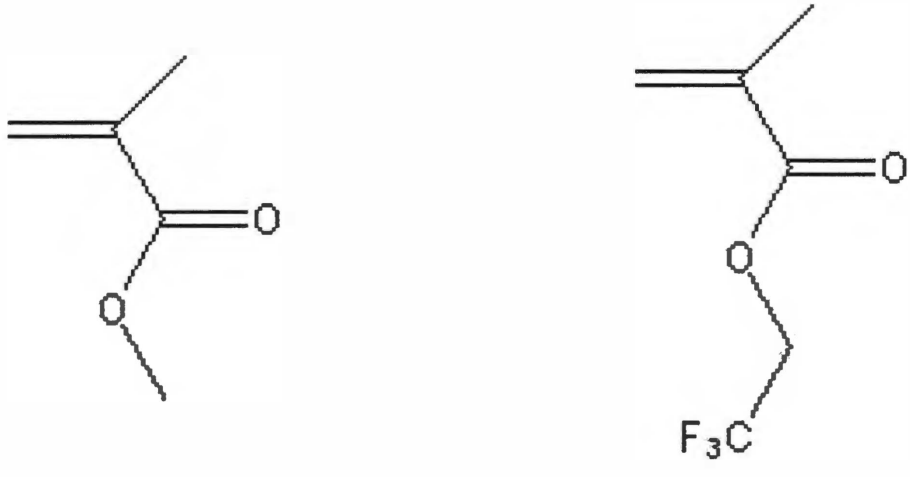


Figure 4.1 Chemical structures of monomers used in atom transfer radical polymerizations, (left to right) methyl methacrylate (MMA) and (2,2,2) trifluoroethyl methacrylate (TFEMA)

applying a vacuum. The contents are allowed to thaw under Ar flow, and the freezing/thawing process is repeated two more times. The reaction vessel is then placed in an oil bath that is heated to 95°C and allowed to react, with stirring, for eight hours. Over the course of the reaction, the contents of the flask undergo a color change, from green to brown, an indication that the catalyst is performing properly.[58] When the eight hour period has elapsed, the reaction is quenched by precipitating the contents of the flask into cold methanol. Copolymer compositions are determined by ^{1}H-NMR, and copolymer molecular weights are determined by GPC, see Table 2.1 in Chapter 2 for the results.

Optical Microscopy

The blends for this study are made by dissolving the desired weights of 8CB and P(MMA-co-TFEMA) in dichloromethane to give a 50 % by mass solution followed by casting onto a Teflon sheet. After drying for 24 hours at 60° C under vacuum slices from the films are used to make the microscopy samples.

Determination of the equilibrium phase diagrams was accomplished by optical microscopy with an Olympus BH-2 microscope. The microscope was equipped with a cross-polarizer for the LC transitions as well as phase-contrast mode to detect the isotropic mixing. The samples cut from the films are placed on clean glass slides with a Kapton spacer (~25μm) covered by a glass cover slip. Heating the samples takes place in a Mettler FP82HT heating stage controlled by a Mettler FP90 Central Processor at a rate of 1°C/min.

In order to apply the Flory-Huggins theory to the microscopy results, the technique that is employed in this work originates from Benmouna et al and their work

with PS/8CB blends.[23] The total free energy, f, see Equation (E 4.1), that describes the phase behavior of the blend is actually the sum of two contributions, the isotropic, f_i, and the anisotropic, f_a, free energies.

$$f = f_i + f_a \qquad \text{(E 4.1)}$$

The isotropic portion of the free energy, f_i, is determined from the Flory-Huggins (FH) theory for polymer solutions.[16-18] The expression for the F-H free energy of mixing along with its use in calculating phase diagrams for comparison to optical microscopy results has already been introduced in Chapter 3. The present chapter uses the same procedure, however, some changes have been made to the determination of the effective segment lengths as well as the Flory-Huggins interaction parameter, χ.

The effective segment lengths, N_1 and N_2, for both the LC and the copolymer are determined in a similar manner to the polymer molecular weight study given in the preceding chapter.[23,62] The segment length of the LC, N_1, is equal to 1 because the volume that is occupied by a single LC molecule defines the size of each lattice site. The determination of the copolymer segment length, N_2, differs from the earlier approach by using the microscopy results for each copolymer/LC blend, rather than obtaining a preliminary fit to F-H theory. The fraction of the LC that corresponds to maximum temperature from the phase diagram, ϕ_{max}, is equated to the critical LC fraction, $\phi_{critical}$. Estimation of N_2 for each copolymer is accomplished by using the relationship, $\phi_{critical} = N_2^{1/2}/(N_2^{1/2} + N_1^{1/2})$.

The current understanding regarding χ is defined in this work as an unknown contribution to the free energy of the mixture, rather than a purely enthalpic parameter.[16-18, 62-68] The expression for χ is shown in Equation (E 4.2) where A is the entropic

$$\chi = A + B/T \qquad \text{(E 4.2)}$$

portion, B is the enthalpic portion, and T is the absolute temperature. For binary solutions of homopolymers and LC's equation (E 4.2) is sufficient to define χ, however, the blends in this study use copolymers that are composed of monomers with significantly different chemical structures. As a result, the expression for χ needs to reflect the presence of not only 8CB-MMA interactions but also 8CB-TFEMA and MMA-TFEMA interactions.

The necessary modification to the expression for χ is derived from studies of Kambour and others on copolymer solutions.[81] These studies extend the mean-field framework of F-H theory to explain regions of miscibility that are present in copolymer blends but are absent in homopolymer blends. The authors conclude that repulsions between the copolymer segments, such as intra- /inter-chain interactions, can actually increase the miscibility of a copolymer in a blend relative to miscibility of a homopolymer blend. These interactions are accounted for by introducing an effective interaction parameter for the entire blend, χ_{total}, that is composed of multiple interaction parameters. For example, in a polymer blend where the components are a copolymer that is composed of A_x and B_{1-x} monomers mixed with a homopolymer of C monomers,[82-83] the effective interaction parameter is composed of three separate interaction parameters, χ_{AC}, χ_{BC}, and , χ_{AB}, see Equation (E 4.3). The contribution of each interaction parameter

$$\chi_{total} = (x)\chi_{AC} + (1-x)\chi_{BC} - (x)(1-x)\chi_{AB} \qquad \text{(E 4.3)}$$

is determined by the copolymer composition, that is, by the molar ratios, x and 1-x, of the A and B monomers in the copolymer. Using this expression for χ, the authors are able to successfully use F-H theory to describe the regions of miscibility observed in such copolymer blends. Subsequent studies by other researchers also show the utility of this multi-parameter χ in predicting the phase behavior of many different copolymer blends.[82-84]

The advantage of applying Kambour's expression for χ to the 8CB/P(MMA-co-TFEMA) blends is three-fold. First, the multi-parameter definition accounts for all of the interactions between the different monomers and the 8CB molecules, as shown in Equation (E 4.4). Second, the dependence of χ given in (E 4.4) on copolymer

$$\chi_{total} = (x)\chi_{8CB\text{-}MMA} + (1-x)\chi_{8CB\text{-}TFEMA} - (x)(1-x)\chi_{MMA\text{-}TFEMA} \qquad \text{(E 4.4)}$$

composition means that a single expression for χ can be used for all of the copolymers used in this study. Finally, since each term in the equation is an interaction parameter, the temperature dependence for χ that has already been established in (E 4.2) is applicable and provides a method to extract additional information about the consequence of TFEMA content on the phase behavior of the PDLC mixtures. The determination of a single function for χ that can be used for all of the copolymer compositions follows a four-step process. The first step requires the determination of the χ_{total}, along with its temperature dependence, for each mixture containing the five copolymer samples. Using the segment lengths for each copolymer and the LC, the critical interaction parameters, $\chi_{c,total}$, are calculated using Equation (E 4.10).[23, 81-84] The temperature dependence for

$$\chi_{c,total} = (N_1^{-1/2} + N_2^{-1/2})^2/2 \qquad \text{(E 4.10)}$$

$\chi_{c,total}$ is obtained from the phase diagram of a given copolymer/LC mixture using (E 4.10) and fitting the data to FH theory as in Chapter 3. Since the molecular weights of the copolymers are similar to those in Chapter 3, it is assumed that the entropic portion of $\chi_{c,total}$, A, has a value of -4.5, as was found for the 8CB/PMMA blends. The enthalpic portion of each $\chi_{c,total}$, B, is then calculated for each copolymer/LC blend by using the critical temperature, T_c, that is obtained from the maxima in the microscopy results.

The second step uses the experimentally determined χ's and Kambour's theory to extract individual interaction parameters between component pairs, using Equations (E 4.5 - 4.9) where χ_{total} is experimentally determined. This set of equations is solved simultaneously in order to determine $\chi_{8CB\text{-}MMA}$, $\chi_{8CB\text{-}TFEMA}$, and $\chi_{MMA\text{-}TFEMA}$.

$$\chi_{8\%,\,total} = (0.92)\chi_{8CB\text{-}MMA} + (0.08)\chi_{8CB\text{-}TFEMA} - (0.074)\chi_{MMA\text{-}TFEMA} \qquad \text{(E 4.5)}$$

$$\chi_{19\%,total} = (0.81)\chi_{8CB\text{-}MMA} + (0.19)\chi_{8CB\text{-}TFEMA} - (0.015)\chi_{MMA\text{-}TFEMA} \qquad \text{(E 4.6)}$$

$$\chi_{25\%,total} = (0.75)\chi_{8CB\text{-}MMA} + (0.25)\chi_{8CB\text{-}TFEMA} - (0.188)\chi_{MMA\text{-}TFEMA} \qquad \text{(E 4.7)}$$

$$\chi_{44\%,total} = (0.56)\chi_{8CB\text{-}MMA} + (0.44)\chi_{8CB\text{-}TFEMA} - (0.246)\chi_{MMA\text{-}TFEMA} \qquad \text{(E 4.8)}$$

$$\chi_{70\%,otal} = (0.30)\chi_{8CB\text{-}MMA} + (0.70)\chi_{8CB\text{-}TFEMA} - (0.210)\chi_{MMA\text{-}TFEMA} \qquad \text{(E 4.9)}$$

The third step in determining $\chi_{8CB\text{-}MMA}$, $\chi_{8CB\text{-}TFEMA}$, and $\chi_{MMA\text{-}TFEMA}$ is to solve the five equations, (E 4.5-4.9), simultaneously by successive elimination of the unknowns, or Gaussian elimination.[85] The solution of the equations is accomplished by using the temperature dependence of χ_{total} for each copolymer blend to calculate χ_{total} in each of the equations for three different temperatures, 50, 100, and 180°C. By solving the equations in this way, the values that are determined for $\chi_{8CB\text{-}MMA}$, $\chi_{8CB\text{-}TFEMA}$, and $\chi_{MMA\text{-}TFEMA}$ at

each temperature are used to establish the temperature dependence for each interaction parameter.

Since five equations must be solved simultaneously, multiple solutions are expected for each interaction parameter. As a result, the fourth step of this process is to set criteria that will reduce the number of solutions to a manageable amount. The first condition is to define the relative strength of each interaction parameter that is based on a physical picture. When considering the different interactions between the monomers and the LC, a reasonable assumption is that interactions involving TFEMA would result in stronger interactions. Therefore, in this study the hierarchy of the interaction parameters is expected to follow $\chi_{8CB\text{-}TFEMA} > \chi_{MMA\text{-}TFEMA} > \chi_{8CB\text{-}MMA}$. The second condition is to choose the set of χ's that give the most reasonable fit to the microscopy data when used in conjunction with FH theory.

4.3

Results and Discussion

A typical phase diagram that depicts the phase behavior of the blends made with the 8% TFEMA copolymer is shown in Figure 4.2. The smectic-nematic transition, shown by the triangles, occurs between 32-34 °C, and the nematic-isotropic transition, denoted by the diamonds, for 8CB is observed between 41-42 °C. The isotropic mixing transition is given by the upper set of data points, the squares. As the TFEMA content is increased, the liquid crystalline transitions remain unchanged, but the isotropic mixing transitions, shown in Figure 4.3, show a steady increase in temperature. These increases are especially dramatic (nearly 20°C) as the TFEMA content goes from 19-25% as well as from 44-70%. This optical microscopy data quantifies the change in the mixing

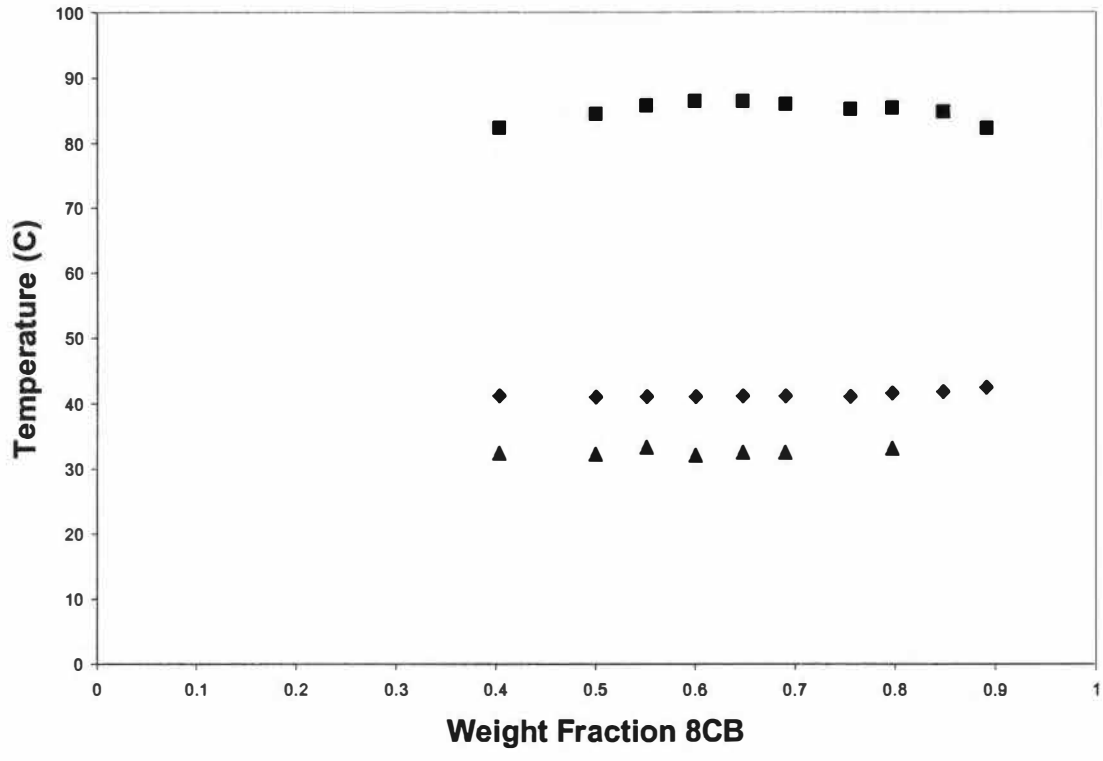


Figure 4.2 Typical phase diagram for 8CB/copolymer blends (8.3% TFEMA); (▲) Smectic to nematic transition, (◆) Nematic to isotropic transition, (■) Isotropic mixing transition

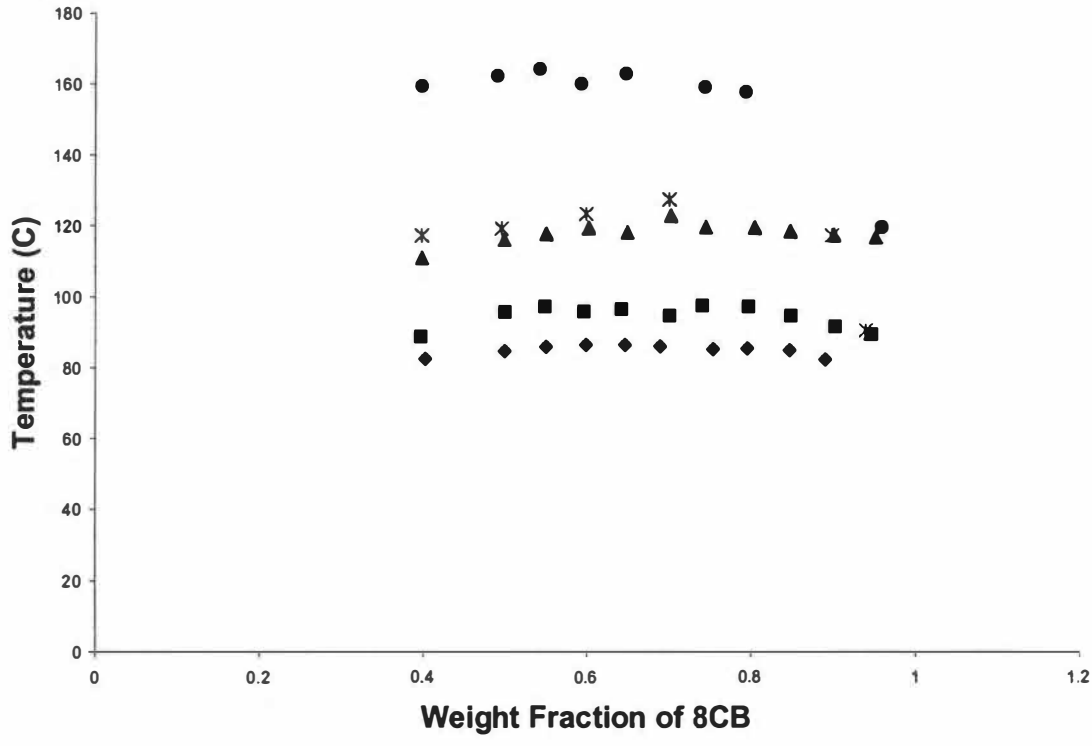


Figure 4.3 Comparison of isotropic mixing transitions for all 8CB/copolymer blends; (◆) 8.3 % TFEMA, (■) 19% TFEMA, (▲) 25% TFEMA, (∗) 44% TFEMA, (●) 70% TFEMA

behavior of methacrylates and cyanobiphenyls with the incorporation of fluorinated monomers into the acrylate matrix. In particular, the isotropic mixing curves show a continuous decrease in LC solubility with increasing TFEMA content, an observation that is important for two reasons. First, the dramatic increases in isotropic mixing temperatures show that even small changes in matrix fluorination, i.e. the almost twenty degree jump between copolymer matrices that contain 19 and 25% TFEMA, can dramatically change LC solubility. Second, the continuous decrease in LC solubility with increasing TFEMA content implies that LC solubility can be continuously "tuned" through controlled incorporation of TFEMA, and the data presented here provides the fundamental data necessary to design and predict the behavior of such PDLC mixtures. In order to quantify the effect of increasing TFEMA content on the phase behavior of PDLC mixtures, theoretical coexistence curves must be determined from FH theory and compared to the microscopy data. Before the theoretical fits can be made, though, a single, temperature-dependent function for χ_{total} is needed from the simultaneous solution of equations (E 4.5)-(E 4.9). The results for $\chi_{8CB\text{-}MMA}$, $\chi_{8CB\text{-}TFEMA}$, and $\chi_{MMA\text{-}TFEMA}$ at 50, 100, and 180°C that meet the condition $\chi_{8CB\text{-}TFEMA} > \chi_{MMA\text{-}TFEMA} > \chi_{8CB\text{-}MMA}$ are plotted versus the absolute temperature in Figure 4.4. Each interaction parameter shows a linear decrease with increasing temperature, as shown by the trend lines in the figure. This behavior agrees with the definition of χ from the experimental section. The linear behavior of the interaction parameters yields three temperature-dependent equations that are used to form the equation for the temperature dependence of χ_{total}, shown in

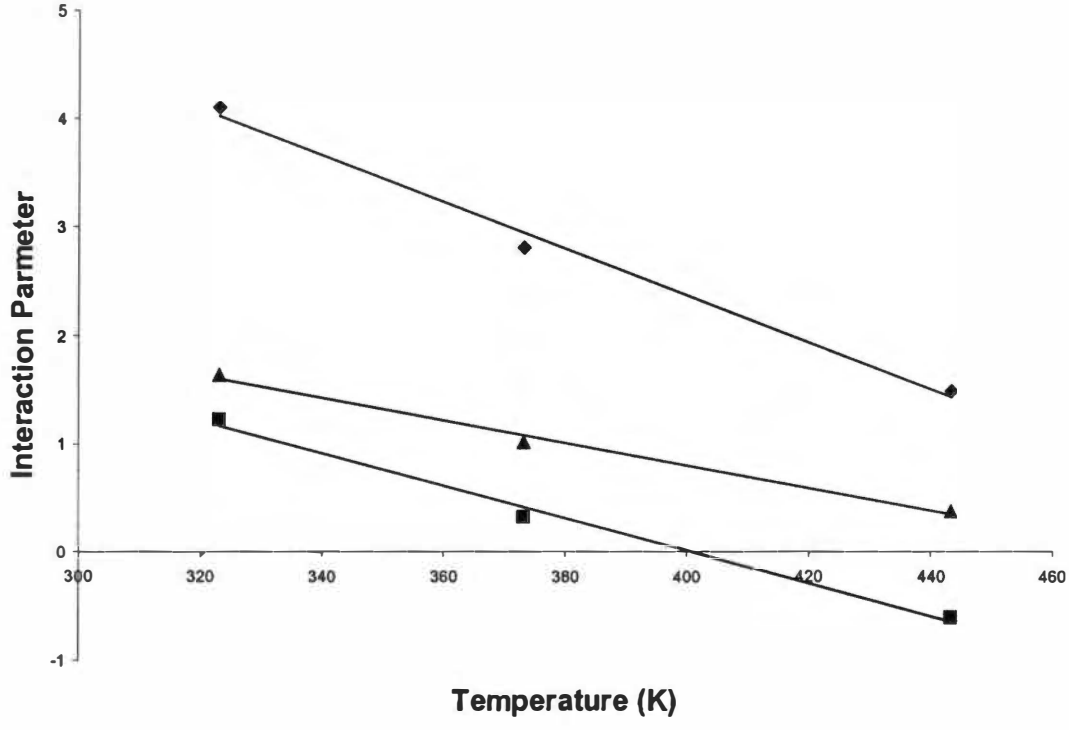


Figure 4.4 Interaction parameters that result in the best fit to the microscopy results, (◆)$\chi_{8CB\text{-}TFEMA}$, (▲)$\chi_{MMA\text{-}TFEMA}$, (■)$\chi_{8CB\text{-}MMA}$

equation (E 4.18). This equation for χ_{total} is then used to calculate the phase diagram of the mixtures of 8CB with any copolymer of MMA and TFEMA using FH theory, and this

$$\chi_{total} = (x)(-5.5 + 2170/T) + (1-x)(-5.5 + 3100/T) - (x)(1-x)(-3 + 1500/T) \quad \text{(E 4.18)}$$

result is compared to the microscopy data. Figure 4.5 shows these calculated phase diagrams and the experimental data.

There is very good agreement between the theoretical data and the microscopy results. Thus, this analysis provides a quantification of the impact of incorporating a fluorinated monomer into the matrix of a PDLC device. This impact is illustrated in Figure 4.6, which is a plot of χ_{total} versus TFEMA content in the copolymer at 80°C. From this plot, χ_{total} exhibits a continuous, linear increase with TFEMA content, as expected.

Thus far, the experimental results support the application of a single interaction parameter to the theoretical description of copolymer/LC blends, however, this analysis remains incomplete without discussing its limitation. In the coexistence curves determined from FH theory, the agreement between theory and experiment, while sufficient to support the application of χ_{total}, is not exact. A reasonable explanation for this deviation between theory and experiment is that the use of the theory to correlate χ_{total} to each individual interaction between monomer pairs assumes a statistically random distribution of the segments within the copolymer chains. In copolymers that are synthesized by free-radical polymerizations,[13,55] though, the monomers that make up the polymer segments may form blocks that can change the inter-/intra-segment interactions, and the effect of these "blocky" copolymers on the phase behavior is dependent on the

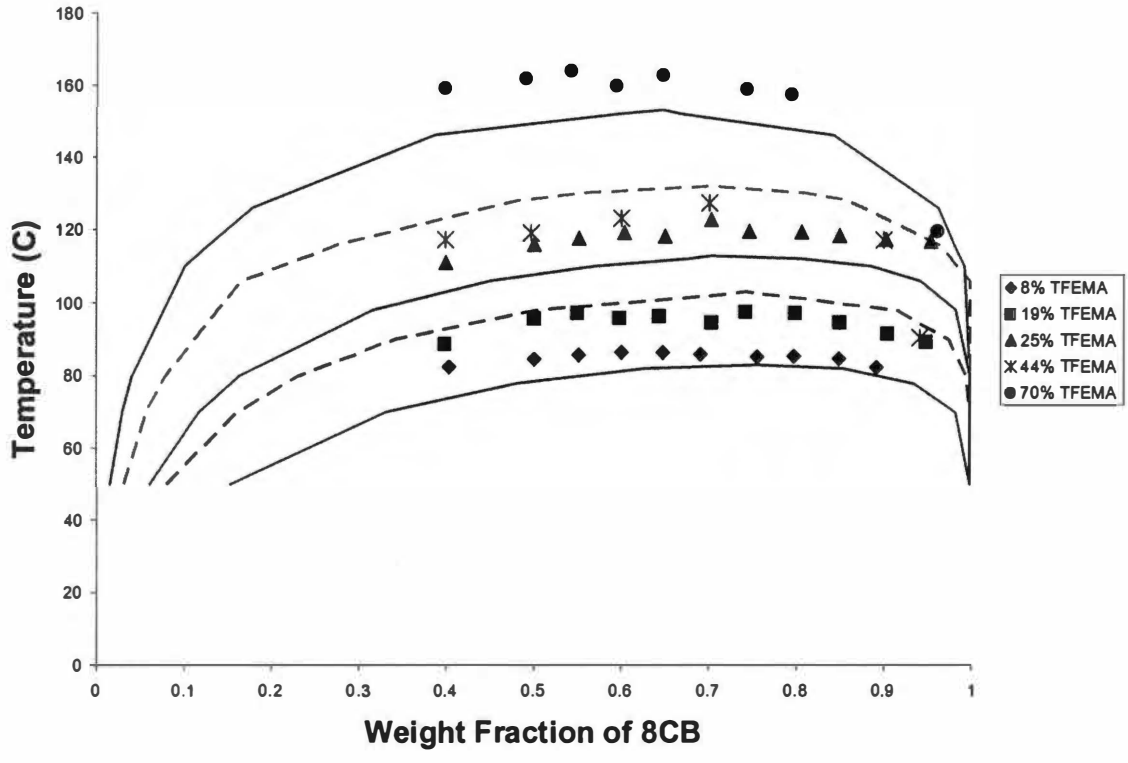


Figure 4.5 Isotropic mixing data with fits (solid and dashed lines) to Flory-Huggins theory

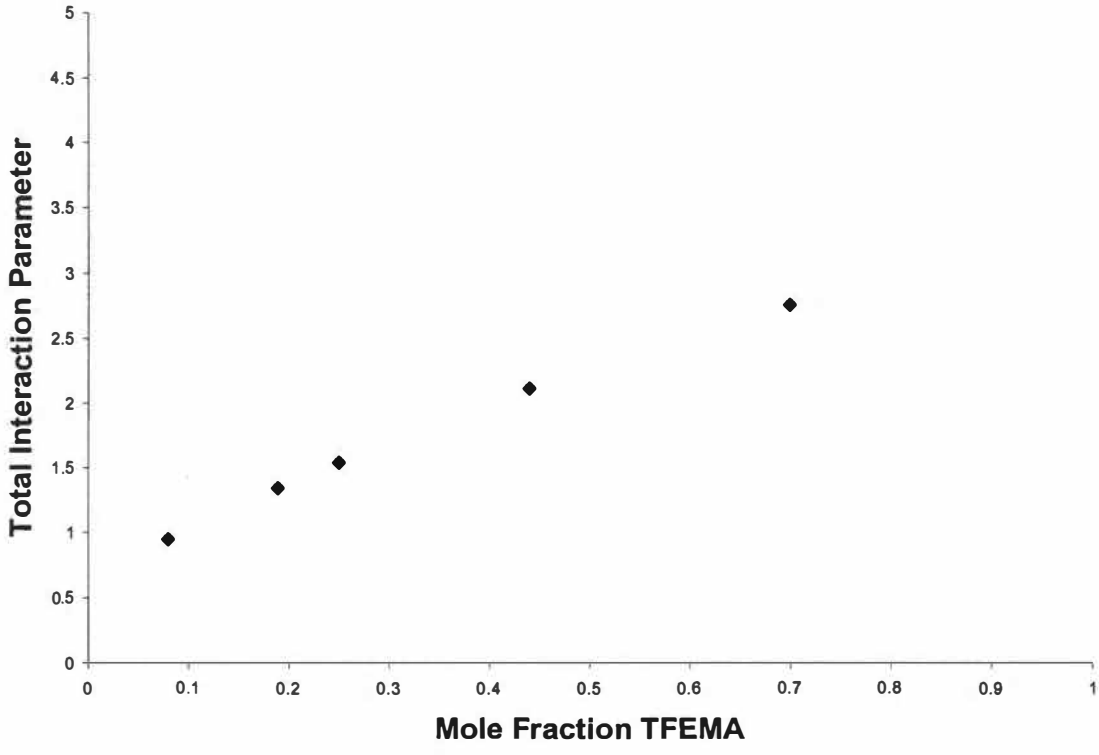


Figure 4.6 The total interaction parameters that are based on the Flory-Huggins fits to microscopy data plotted versus mole fraction of TFEMA in the copolymer calculated at 80°C

length and distribution of these blocks. Since the determination of block length effects on these blends is non-trivial, further refinements to the theoretical treatment presented in this work are required and should be the focus of future work.

4.4

Conclusions

Copolymers with controlled percentages of TFEMA and MMA have been used to successfully quantify the impact that the presence of a fluorinated monomer has on the thermodynamics of PDLC systems that include fluorinated monomers as a component in the polymer matrix. The phase diagrams determined by optical microscopy show a continuous, linear decrease in LC solubility with increasing fluorination content. Good agreement between the microscopy results and coexistence curves determined by Flory-Huggins theory is observed when the total FH interaction parameter, χ_{total}, accounts for the three separate interactions, $\chi_{8CB\text{-}MMA}$, $\chi_{8CB\text{-}TFEMA}$, and $\chi_{MMA\text{-}TFEMA}$, which quantifies all interaction parameters between component pairs. This quantification of all interaction parameters between component pairs provides all the fundamental information that is required to predict the thermodynamics of these PDLC. Moreover, the straightforward experimental procedure and analysis presented here can readily be applied to other polymer/liquid crystal mixtures where fluorinated monomers are incorporated into the matrix to control liquid crystal solubility and anchoring in the droplet. Thus, the quantification of the changes in LC/copolymer thermodynamics when fluorinated monomers are present can be quantified with this technique and provide the fundamental information needed to design optimal polymer-dispersed liquid crystal devices.

CHAPTER 5

Time-resolved Light Scattering of Phase Separation in PDLC's Formed by Photo-polymerization Induced Phase Separation

5.1

Introduction

From the discussion of PDLC construction in Chapter 1, an important method that is used to construct PDLC devices is photo-polymerization induced phase separation, or PIPS. The process starts with a homogeneous mixture of LC, multi-functional monomer, and photo-initiator. When polymerization begins, usually by free radical reaction, the rapid formation of a cross-linked polymer matrix thrusts the blend into thermodynamic instability, similar to a thermal quench. As the polymerization continues, the cross-linking of the polymer matrix halts the phase separation of the LC upon the complete gelation and subsequent vitrification of the matrix.

In order to optimize the electro-optical performance of PDLC devices, parameters that impact the final morphology of PDLC's that are produced by PIPS must be understood. Some of these factors include solubility of the LC in the matrix, LC content, monomer functionality, as well as the polymerization rate. LC solubility[3-5,9] in the resulting polymer matrix determines the percentage of the LC that is able to remain phase separated and, as a result, has been the subject of many studies.[4,6,15, 19,23,24,42,61,62,86] The LC content plays a vital role in PIPS by affecting not only the size of the domains but also the trajectory of the blend as it is moved through thermodynamic phase space by the polymerization. This factor has also been the subject of works by Serbutoveitz et al and more recently by Vaia and co-workers.[28,29,36] The choice of monomer, especially if it is

multi-functional, can drastically change the cross-link density within the PDLC, a condition that has been shown by Pogue et al[87] to alter the size, shape, and number of the LC domains. Factors that affect the polymerization rate, such as temperature, reaction chemistry, or, in the case of photo-polymerization, illumination intensity, are also vitally important because of their obvious effect on the formation of the polymer matrix itself. Studies have been carried out to determine the effects that temperature and different reaction chemistries have on PDLC morphology, however, work to determine the effect of the cure intensity on phase separation kinetics has been limited to UV-cured systems.[52]

In order to probe the complex phase separation process that occurs during PIPS, different experimental techniques have been employed. Optical microscopy (OM) has been a commonly used technique to observe the formation of the LC domains.[5,6] Complimentary to OM, differential scanning calorimetry is employed to monitor the polymerization reaction as well as the emergence of the LC domains, signified by the appearance of liquid crystalline transitions.[6] Scanning electron microscopy, or SEM, is employed in several studies to study the morphology of the polymer matrix but only after the LC is removed.[36,87] Scattering techniques, specifically light and x-ray, are used to observe morphological changes over the sample volume. Time-resolved light scattering (TRLS), in particular, offers a non-destructive method to continuously monitor phase separation on length scales from hundreds of nanometers to microns. However, the experiments that exploit this technique have been very limited in number.[52]

The goal of this chapter is to utilize TRLS to study the phase separation kinetics of PDLC systems developed by Bunning and co-workers. Two of the factors mentioned previously, LC content and cure intensity, are varied to determine the impact on the PIPS

process. The syrups that are studied contain 40 and 50% by weight of the LC E7, compositions that have been shown by Vaia et al[36] to yield different matrix morphologies. The role of cure intensity on PIPS is determined by curing both LC compositions at four different intensities; 0.069, 0.14, 0.21, and 0.69 mW/cm^2. This range of intensities should provide significant changes in the speed of matrix formation that, in turn, should yield different phase separation behavior.

5.2

Experimental

Materials and Polymerization Scheme

The samples of PDLC syrup are provided by T.J. Bunning and L.V. Natarajan at Wright-Patterson Air Force Base. The syrups consist of the liquid crystal E7 (40% and 50% by weight), dipentaerythritol dihydroxypentaacrylate monomer (38% and 48% by weight), co-initiator N-phenyl glycine (2% by weight), a Rose Bengal derivative for photo-initiation, and N-vinyl pyrrolidone (10% by weight) as a homogenizing agent. Chemical structures of the syrup components[87] can be found in Figure 5.1 with the exception of E7, a eutectic LC mixture that is made up of seven different cyano-biphenyls similar in structure to 8CB.

The polymerization of the monomer follows the same mechanism as in photo-initiated free radical polymerizations.[88] The reaction is initiated when a light source, such as the green laser used in the TRLS instrument, causes the excitation of the photo-sensitive dye, the Rose Bengal, see Figure 5.2. The excited dye, labeled RB* in the figure, transfers an electron to the co-initiator, N-phenyl glycine, and the fragmentation

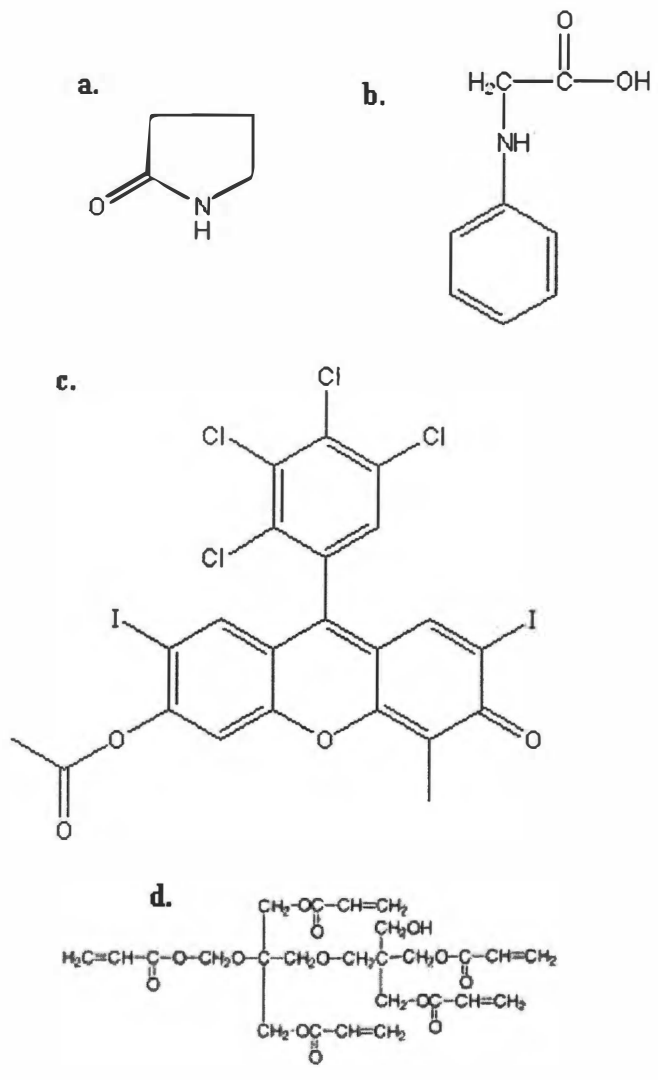


Figure 5.1 Components of syrups used to form PDLC's; a.) N-vinyl pyrrolidone, b.) N-phenyl glycine, c.) Rose Bengal acetate ester, d.) dipentaeryhtritol dihydroxy pentaacrylate

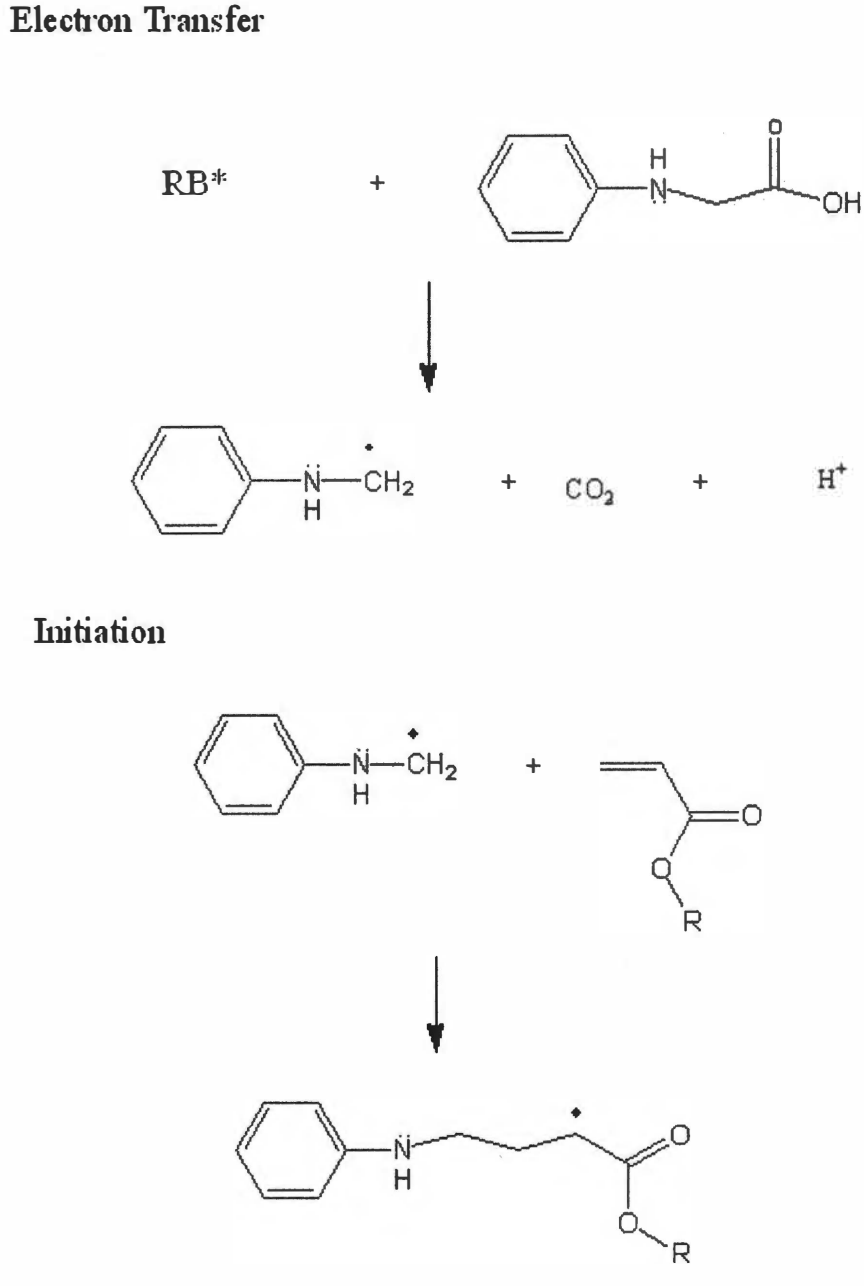


Figure 5.2 Reaction scheme for the photoinitiation of the acrylate monomer through the electron transfer from excited Rose Bengal (RB*) to the co-initiator N-phenyl glycine

of the initiator produces a methyl radical that reacts with the vinyl portion of the acrylate monomer.

Time-resolved Light Scattering

Time-resolved light scattering experiments are performed at ambient temperature (25 °C) using the instrument described in Chapter 2.[54] Samples from the syrups are prepared, under dark room conditions, by pipette onto quartz windows. Each window has a 0.01mm deep cup to ensure the sample is uniform in thickness. Curing of the samples is accomplished by using a green diode laser, also described in Chapter 2.

The time-resolved light scattering instrument records the cross-section of the scattered intensity, I, in arbitrary units, versus scattering angle, θ, between the angles of 0° to 32.37°. The scattering angle is related to the wave vector, q, in μm^{-1}, which provides a measurement of the size of the phase-separated domains.[46] The cross-section of the scattered intensity versus q defines the scattering profile and corresponds to the structure factor, S(q),[46] the function that links the intensity of the scattered light to the structure of the LC domains.

HRSEM

Samples for high resolution scanning electron microscopy, or HRSEM, are prepared by removing the E7 by soaking the fully cured films in methanol overnight. The films are dried *in vaccuo* overnight and shipped to Wright Patterson Air Force Base for HRSEM. The images are analyzed by Image J, the java-based version of the image analysis software NIH Image.

5.3

Results and Discussion

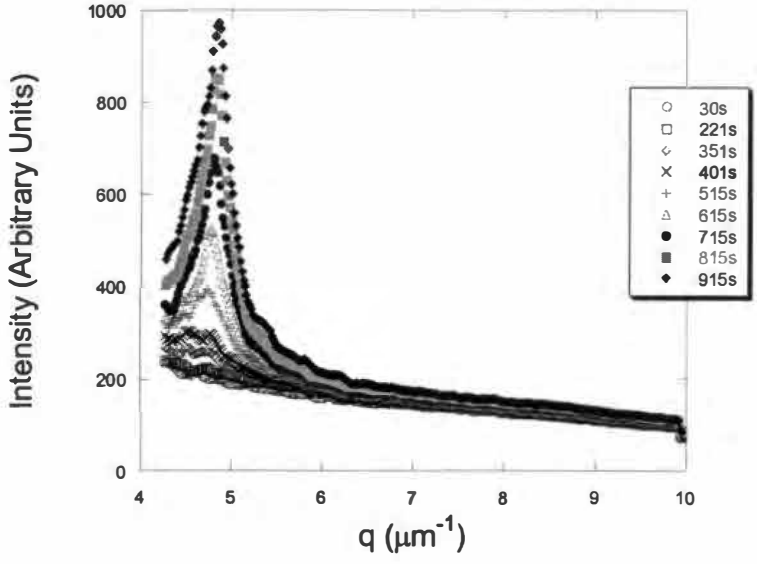
Samples Cured with 0.069 mW/cm^2 Beam

Representative light scattering profiles for both 40% and 50% E7 samples are given in Figure 5.3 a-d. These sets of scattering data are obtained from experiments carried out at the lowest cure beam intensity, 0.0693 mW/cm2, The plots consist of smoothed data obtained by subtracting the background from each spectrum.

Figure 5.3 a and b show data for the 40% E7 sample for experiment times of 30-3245s. The early stages of the experiment do not exhibit any change from the background until 221s when scattering profiles show the appearance of a distinct maximum at $q \sim 4.7\mu m^{-1}$. The maximum grows steadily in intensity at the same wave vector until the time reaches 1020s. The peak then undergoes a shift to lower q at 1120s and continues to grow with time. During the later stages of the experiment we observe the formation of multiple peaks for times greater than 1325s. The complex scattering profiles for these later times make the determination of a single maximum difficult. When the experiment reaches ~3000s, the growth of the scattering intensity slows until there is little change between the profile observed at 3195s and 3245s.

The scattering data that are given in Figure 5.3 c and d show the scattering data for the 50% E7 sample. No difference between the background and the measured intensity is observed for very early stages of the experiment. Around 107s the scattering becomes very broad and increases slowly in intensity through 511s. The maximum that appears during this stage is more difficult to discern than in the 40% E7 samples,

5.3 a.



5.3 b.

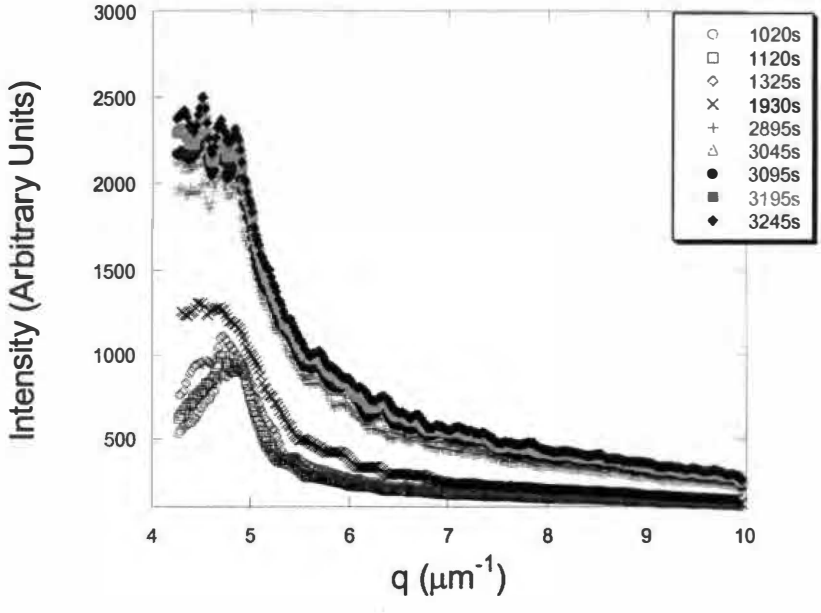
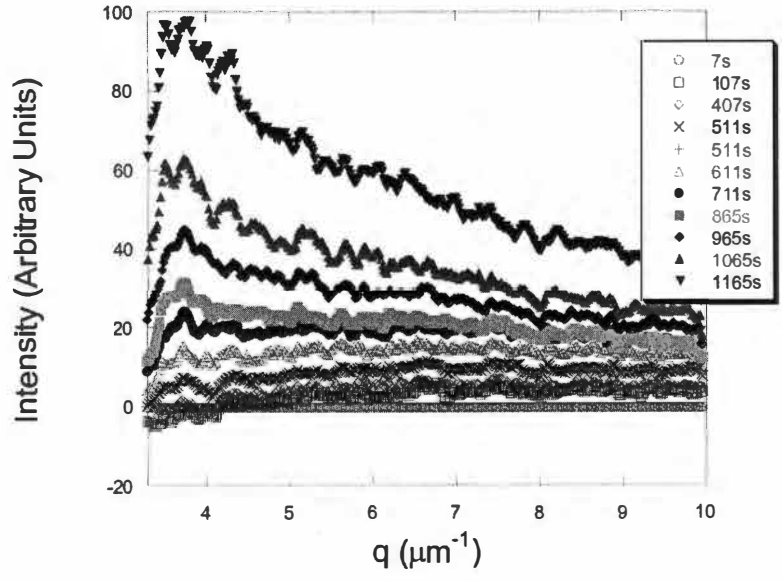


Figure 5.3 Scattering profiles for blends cured at 0.069 mW/cm2. a. 40% E7 30-915s; b. 40% E7 1020-3245s

5.3 c.



5.3 d.

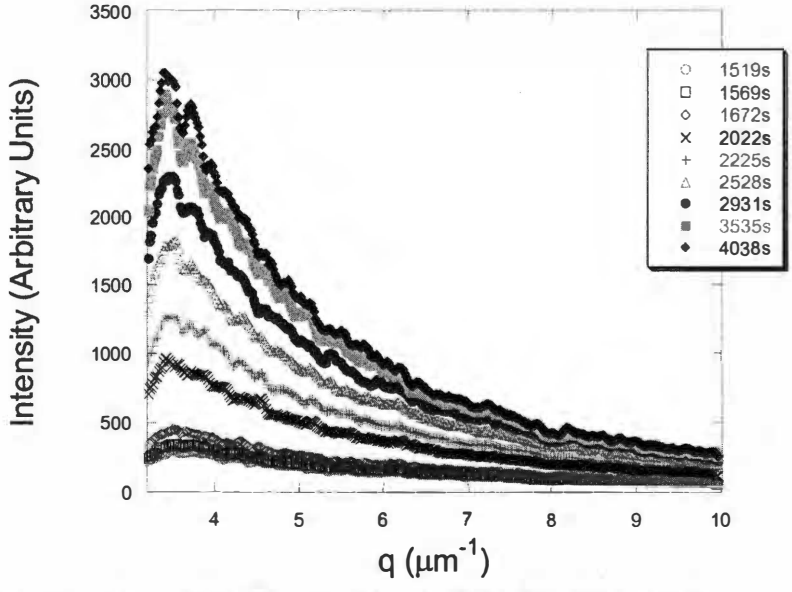


Figure 5.3 Continued. c. 50% E7 7-1165s; d. 50% E7 1519-4038s

however, we estimate the value to fall between q ~ 6.8 – 6.4μm^{-1}. The maximum in the scattering shows a shift to lower q-values, 5.6 to 3.7μm^{-1}, as the time progresses from 611 to 711s. Throughout the remainder of the experiment, 865 – 1165s in 5.3 c and all times in 5.3 d, the profile is dominated by a single maximum that remains between 3.7 – 3.4μm^{-1}. The peak intensity continues to grow with time until 4038s when there is no further change in the scattering.

From the scattering data in Figure 5.3 we observe features that are shared by both LC compositions studied at this cure intensity, and analysis of these curves reveal details regarding the phase separation mechanism. One common feature to both compositions is the delay in time between the start of the experiment and the appearance of an increase in the scattering.This gap, called the induction period,[30-34] is different for the two samples and corresponds to the delay in phase separation from the growth of the polymer matrix. In other words, for the system to favor phase separation of the blend into LC-rich and gel-rich domains, the polymerization must generate matrix material of sufficiently large molecular weight to induce thermodynamic instability. The second feature common to both blends has to do with the appearance of a single maximum in the scattering that not only grows in intensity but also changes in scattering vector with time. Similar behavior has been observed experimentally by Nwabunma et al[33] as well as in the numerical results of Maugey and co-workers[89] as strong support for phase separation by spinodal decomposition, or SD.[89-92] Lastly, when the scattering profiles no longer change, the phase separation process has been effectively arrested, an event that is attributed by Pogue et al[87] to the vitrification of the polymer matrix.

The hallmark of phase separation by SD is the presence of randomly distributed domains that possess a uniform average size and inter-domain spacing, Λ.[89] This SD structure appears in the scattering as a distinct maximum. In the experimental data, the scattering vector for the maximum, q_m, can be converted to Λ by Equation (E 5.1). The Λ results plotted versus time for both compositions can be found in Figure 5.4. For the 40% E7 syrup we see the Λ values show only small changes, from 1.32 to 1.33 μm, during the

$$q_m = 2\pi/\Lambda \qquad \text{(E 5.1)}$$

course of phase separation. In contrast, the 50% E7 sample begins with much smaller inter-domain distances, around 0.9μm, but undergoes a definite increase after 511s until, for the final stages of the experiment, Λ levels off to a value that is two times larger, ~1.8μm. The difference in the inter-domain distance for the two LC compositions also highlights the effect of increasing LC content on the phase separation process. In terms of the time needed for Λ to reach an average value, the 40% E7 sample reaches an equilibrium size roughly three times faster than the 50% E7 system. As for the size of the LC domains, the 50% E7 sample creates a system where the domains are twice as large as that of the 40% samples.

These observations are consistent with previous results by Vaia et al[36] who explain this result in terms of how the LC content changes PIPS process. First, when the LC content is increased, the monomer concentration is decreased, a condition that slows the formation of the polymer matrix. By slowing the polymerization of the monomers, the complete gelation of the matrix, which inhibits phase separation of the LC, is delayed, and the LC domains have more time to grow larger. Second, the greater LC content

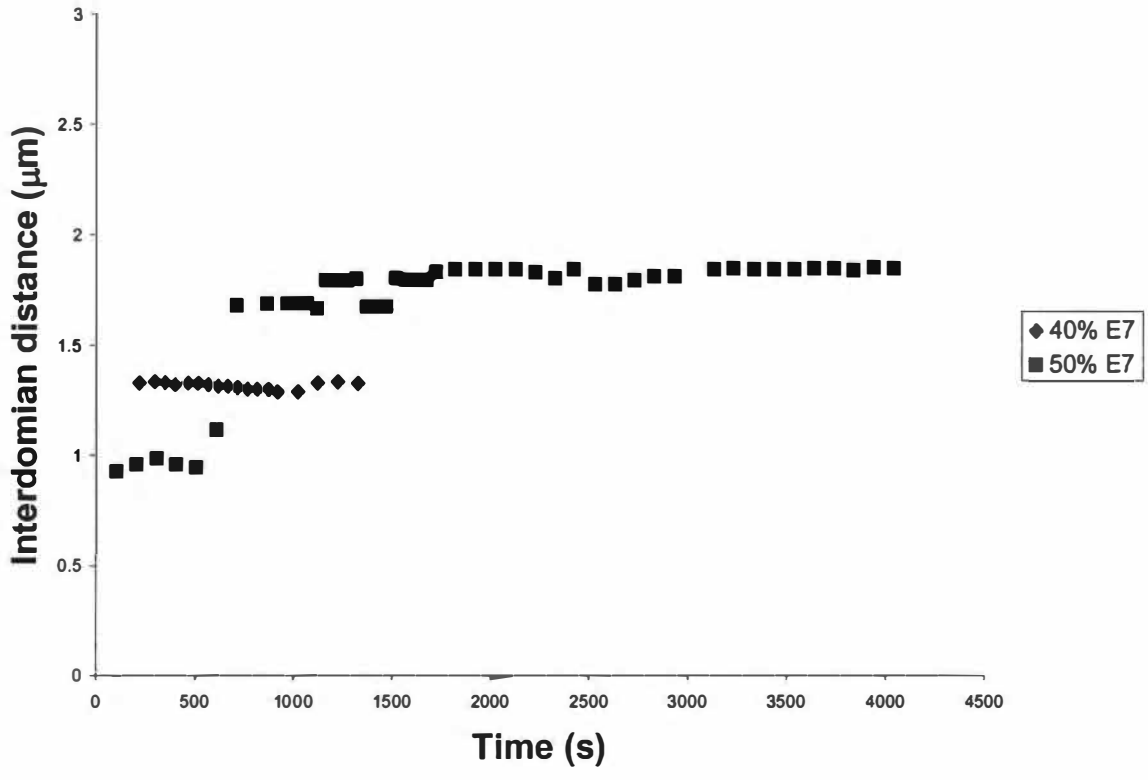


Figure 5.4 Plot of interdomain distance versus time for both LC compositions, (◆) 40% E7, (■) 50% E7

decreases the cross-link density of matrix which creates greater freedom for the LC to diffuse out of the matrix. These two factors mean that the 50% E7 sample has more time before gelation of the matrix halts phase separation in addition to greater freedom for phase separation which leads to larger interdomain distances.

During the early stages of SD,[90-93] the composition fluctuations exhibit a dominant length scale that results in a maximum in its scattering profile, and the morphology of the phase-separating components is characterized by an interconnected structure. At first, this lengthscale remains unchanged and the maximum remains at the same scattering vector and grows in intensity with time. The growth of the intensity as a function of q and time, I(q,t), during this period is effectively described by Cahn-Hilliard theory which predicts that I(q,t) grows exponentially with time, t, and at a rate, R(q), by the proportionality in Equation (E 5.2).[89] This exponential growth of I(q,t) is confirmed

$$I(q,t) \propto \exp[2R(q)t] \qquad \text{(E 5.2)}$$

for both the 40 and 50% samples by the semi-logarithmic plots of log I versus time shown in Figure 5.5 for the 40% sample. As shown in Figure 5.5, the log of the intensity, at early times, shows a linear increase for many different scattering vectors.

The growth rate of the scattered intensity, R(q), is directly proportional to the growth of the composition fluctuations and is defined by the equation in (E 5.3).[89]

$$R(q) = D_{app}\, q^2\, [1-(q^2/(2q_m{}^2))] \qquad \text{(E 5.3)}$$

The apparent mutual diffusion coefficient, D_{app},[89-92] in (E 5.3) denotes the rate of motion of the phase-separating components during phase separation, q is the scattering vector, and q_m is the wave vector of the scattering maximum. R(q) is determined from the slope

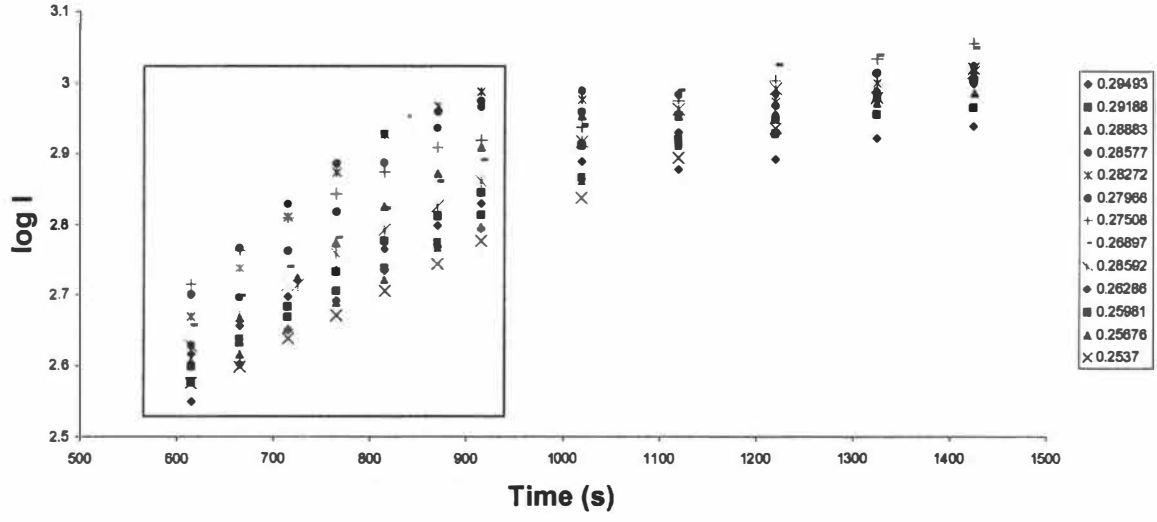


Figure 5.5 Semilogarithmic plot of intensity versus time for different scattering vectors. Slopes of data in highlighted section are used to determine the growth rate function, R(q).

of the linear portion of the semi-logarithmic plots for both LC compositions. When the values for R(q) are plotted as $R(q)/q^2$ vs q^2, D_{app} is determined from the y-intercept, and the D_{app} obtained from this analysis for both LC compositions can be found in Figure 5.6. This analysis indicates that the 40% sample has a D_{app} of 3×10^{-5} $\mu m/s^2$, while the 50% sample shows a D_{app} that is an order of magnitude higher, 2×10^{-4} $\mu m/s^2$.This analysis has assumed that spinodal decomposition is the process by which these samples are phase separating, but this has not been proven. In order to test the validity of using Equations (E 5.2) and (E 5.3) to analyze the data in Figure 5.5, the self-consistency of the D_{app} values is checked in the following way. Since D_{app} defines the rate of the movement of the phase separating components, it is independent of the scattering behavior. As a result, the D_{app} values from the analysis can be used to determine q_m from (E 5.3) that should agree with the maximum in the scattering data. For example, using $q = 4.8172$ μm^{-1}, $D_{app} = 3 \times 10^{-5}$ $\mu m/s^2$, and the growth rate $R(q) = 0.0004$, obtained from the 40% sample in Figure 5.3, yield $q_m = 4.43$ μm^{-1}. The two mutual diffusion coefficients are used in conjunction with Equation (E 5.3) to calculate a value of q_m for comparison to the scattering profiles,[90] see Table 5.1. The good agreement between the calculated and experimental q_m values supports the use of the spinodal decomposition analysis for these samples. The increase in D_{app} with LC content, though not surprising, quantifies the extent of change in the mobility of both the matrix material and the LC that results in the larger interdomain distances of the 50% sample.

As phase separation continues, the interconnected structure of the early stage of SD is expected to grow and eventually break up into discreet LC domains during the

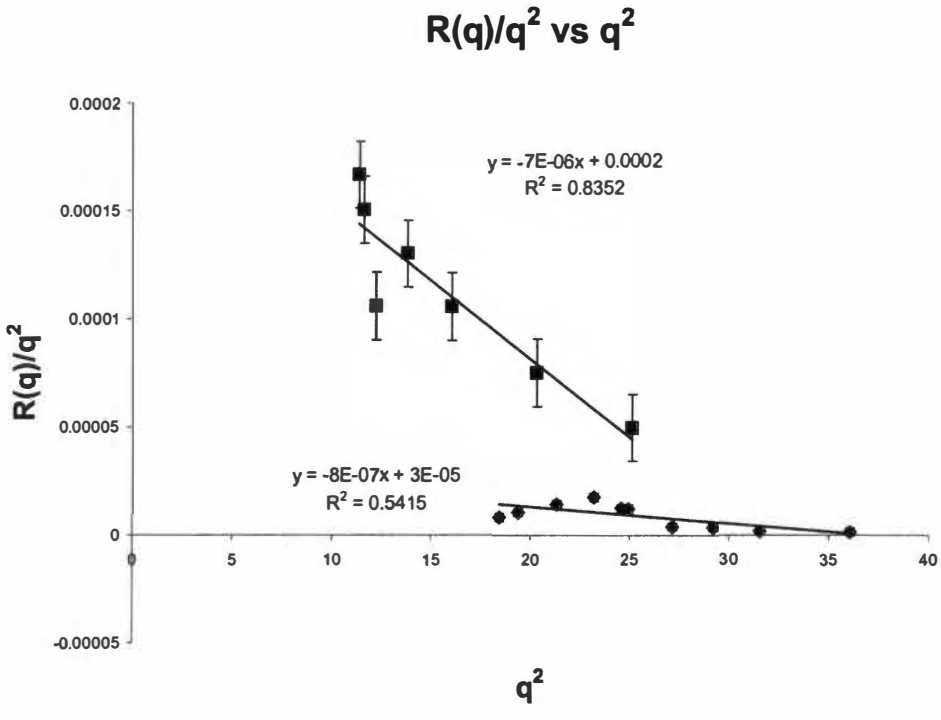


Figure 5.6 Growth rate divided by the square of the scattering vector versus the square of the scattering vector, (◆) 40% E7 and (■) 50% E7. Y-intercept gives the apparent mutual diffusion coefficient, D_{app}.

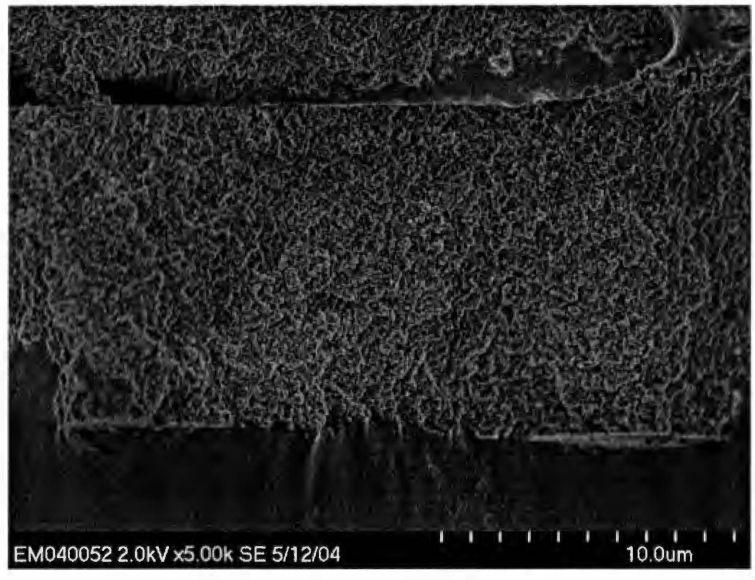
Table 5.1 Apparent diffusion coefficients, D_{app}, obtained from the analysis of the early stages of spinodal decomposition. Maximum scattering vectors, q_m, calculated from D_{app}, compared to experimental results.

% E7	Dapp ($\mu m/s^2$)	q_m, calculated(μm^{-1})	q_m, experimental (μm^{-1})
40	3.00E-05	4.08	4.33
50	2.00E-04	3.78	3.4

intermediate and late stages of SD.[90-93] This transition is usually characterized as a shift in the scattering maximum to lower q, an event that appears to occur during the time period of 912-1120s for the 40% sample and 407-965s for the 50%. At this transition the growth of the maximum intensity, I_m, as well as the shift in the maximum scattering vector, q_m, should scale exponentially with time, as described by the theories of Lifshitz and Slyozov.[94] Additionally, the domains form a self-similar structure during the late stage of SD that grows according to the scaling behavior theorized by Furukawa.[94] However, when the scaling analysis[90] is performed on the scattering maxima for both LC compositions, the results are inconclusive.

In order to determine if either system has actually undergone the transition from early SD to the intermediate/late stages, the LC is removed for the 50% sample, and the resulting film is sent to Wright Patterson Air Force Base for HRSEM. The HRSEM results, shown in Figure 5.7 a and b for a 50% E7 sample that is cured for over two hours, show the film at low magnification (5.7 a, 10 μm scale bar) and higher magnification (5.7 b, 1 μm scale bar). At low magnification the film appears to lack discreet LC domains, a result confirmed by the micrograph at higher magnification. Instead, the morphology still shows the presence of an interconnected structure, a structure more in keeping with the early stage of SD and is supported by Vaia et al[36] who observe an interconnected polymer bead morphology in PDLC's cured under much higher cure intensities. This result suggests that, even at low cure intensities, the break-up of the interconnected structure formed during the early stages of SD is never realized because of the fast gelation and subsequent vitrification of the polymer matrix inhibit further phase separation.[36]

5.7 a.



5.7 b.

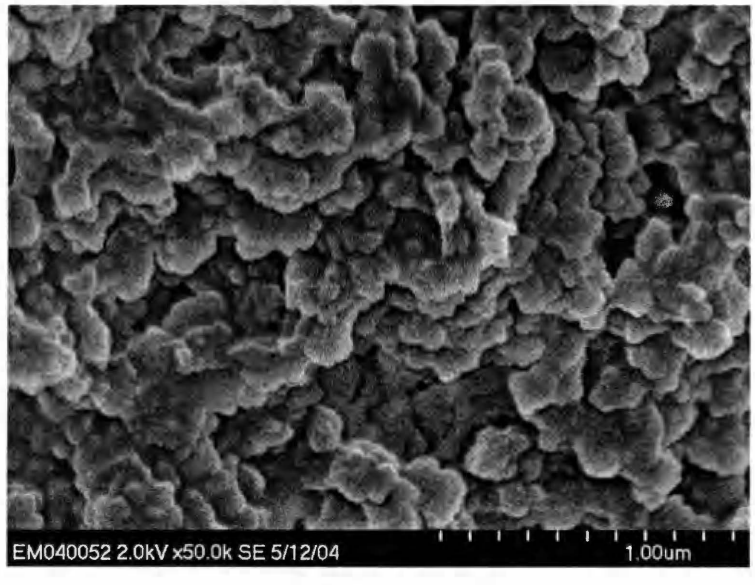


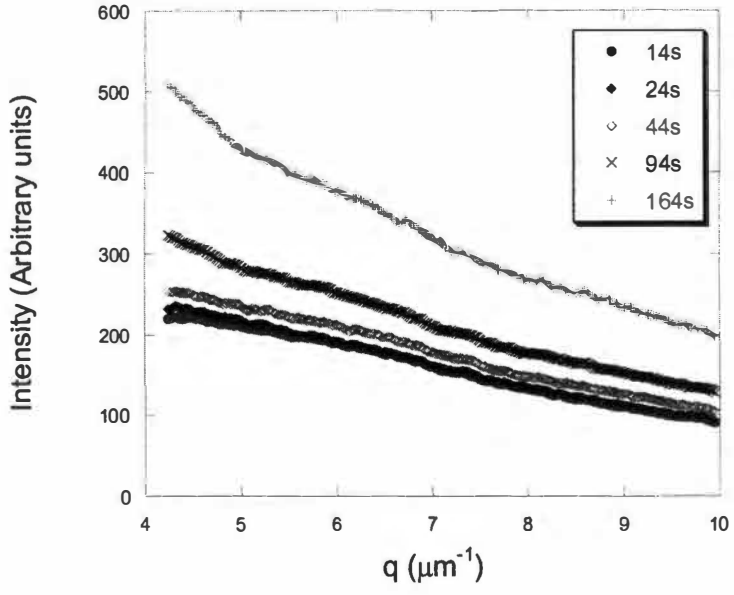
Figure 5.7 HRSEM micrographs of films from 50% E7 sample cured at 0.069mW/cm^2 for over 2hours; a) 10μm; (b) 1μm magnification

Higher Cure Beam Intensities

The scattering profiles for both E7 compositions cured at 0.14 mW/cm^2 can befound in Figure 5.8 a-d. For the 40% E7 sample, see Figure 5.8 a and b, the earliest recorded time, 14s, shows the presence of scattering, but no discernable maximum is observed. The total scattering intensity increases between 54 and 164s and exhibits a sharp upturn in the forward scattering for lower q-values. The total intensity continues to increase throughout the remainder of the experiment until 618s where little change between the scattering profiles is observed. The 50% E7 samples, Figure 5.8 c and d, also exhibit scattering at the earliest recorded time, 25s. For early times, 25-95s, there appears to be a maximum in the scattering, however, this feature rapidly disappears. As the experiment proceeds to later times, the total intensity increases with a similar upturn in the scattering at low q as for the scattering curves of the 40% sample.

Scattering profiles for the samples cured at 0.214 mW/cm^2 cure intensity are shown in Figure 5.9 a-c. As in the previous experiment the 40% E7 samples, Figure 5.9 a and b, exhibit scattering at the earliest stage of the experiment. In contrast to the samples cured at 0.14 mW/cm^2 cure intensity, though, the total scattered intensity increases much more rapidly with time. The growth of the scattered intensity continues until the profiles exhibit very little change at 618s. For the 50% sample, shown in Figure 5.9 c, the increased cure intensity results in rapid growth of the total scattered intensity, and at 103s the detector becomes saturated. The results for both LC compositions cured at the highest of the cure intensities, 0.693 mW/cm^2, can be found in Figure 5.10 a-b. The 40% sample, Fig. 5.10 a., shows much stronger scattering at the outset of the experiment at

5.8 a.



5.8 b.

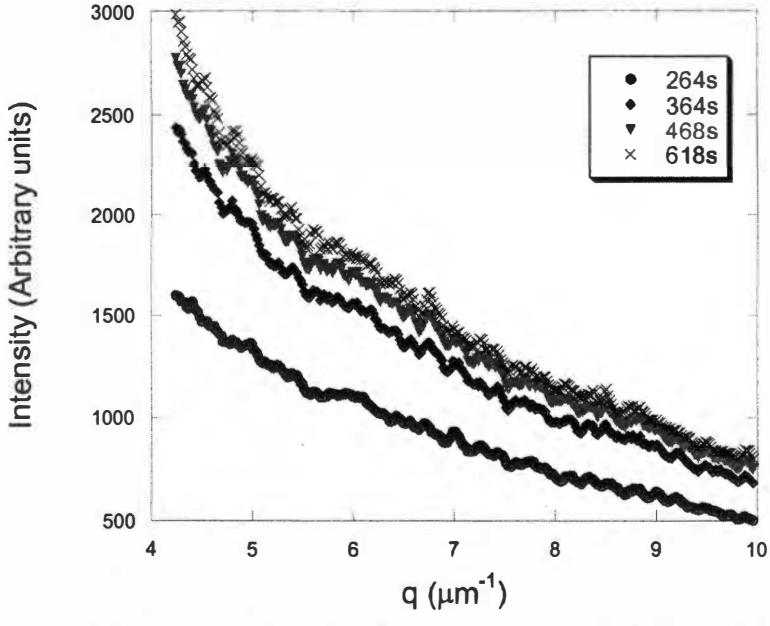
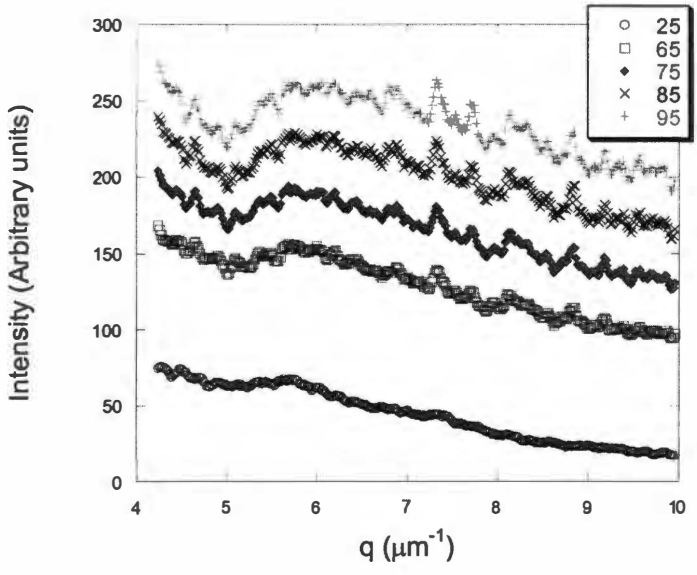


Figure 5.8 Scattering profiles for PDLC syrups cured at 0.14 mW/cm^2. a. 40% E7 14-164s; b. 40% E7 264-316s

5.8 c.



5.8 d.

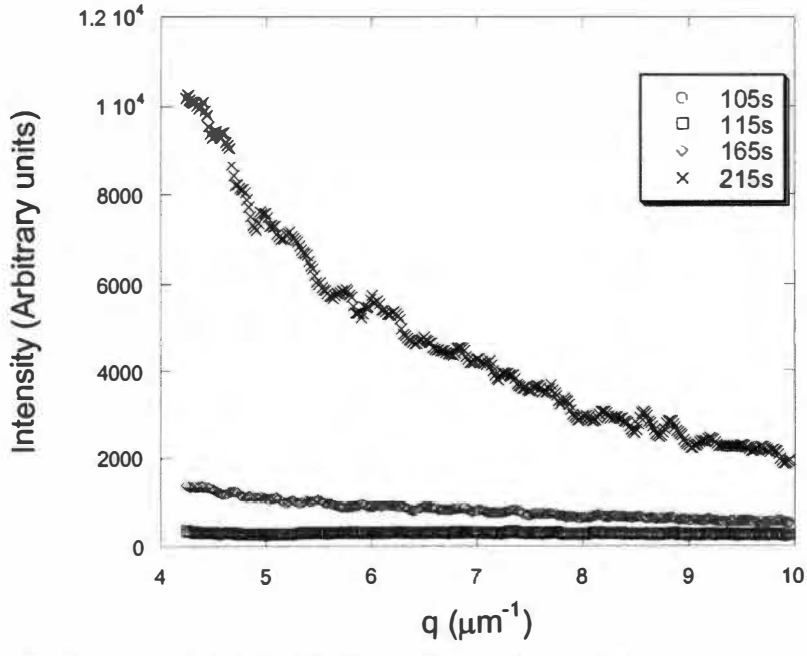
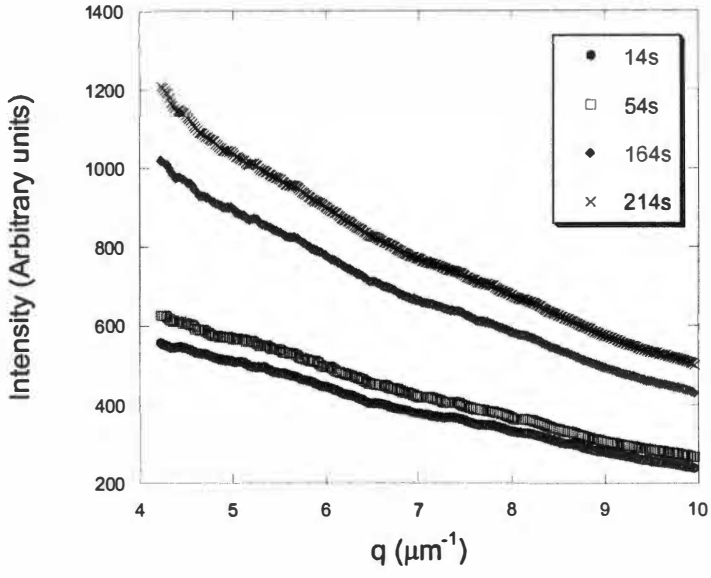


Figure 5.8 Continued. c. 50% E7 25-95s; d. 50% E7 105-215s

5.9 a.



5.9 b.

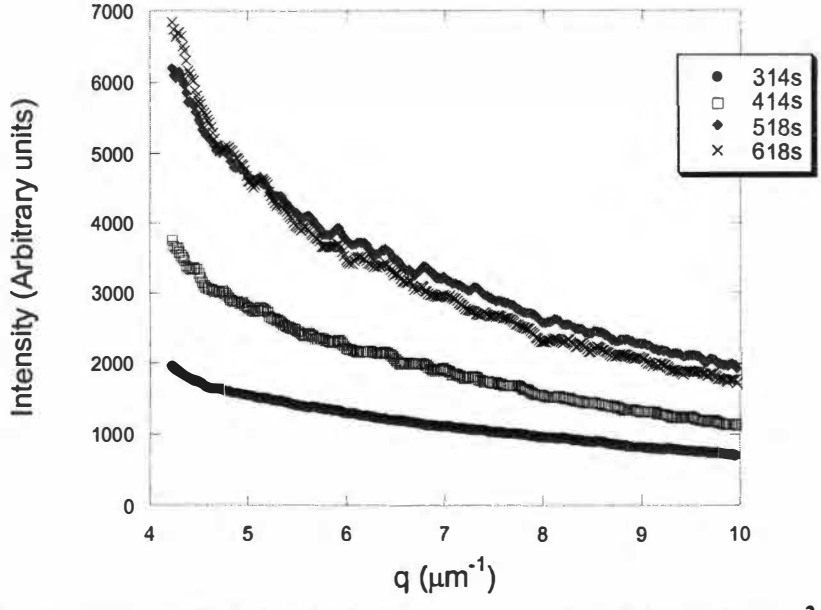


Figure 5.9 Scattering profiles for PDLC syrups cured at 0.214 mW/cm^2. a. 40% E7 14-214s; b. 40% E7 314-618s

5.9 c.

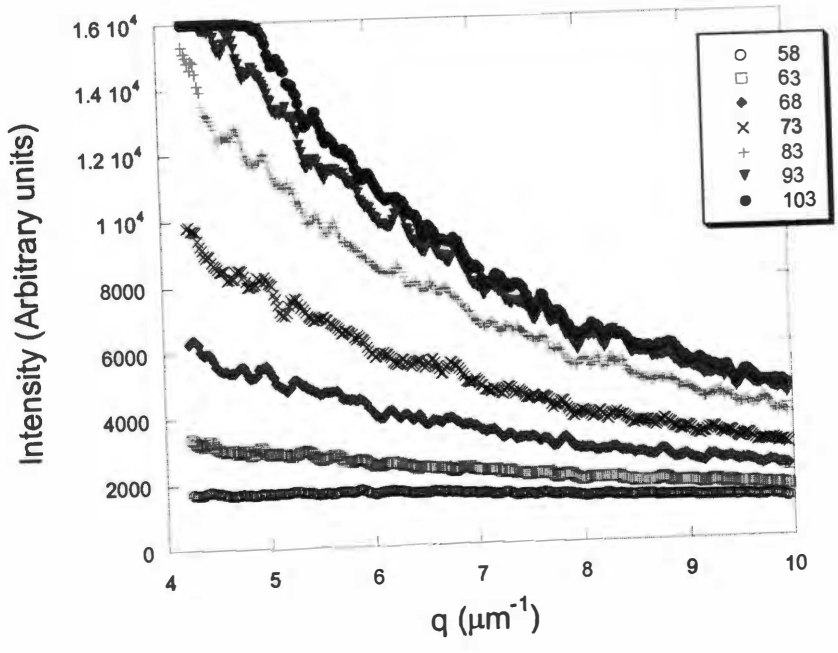
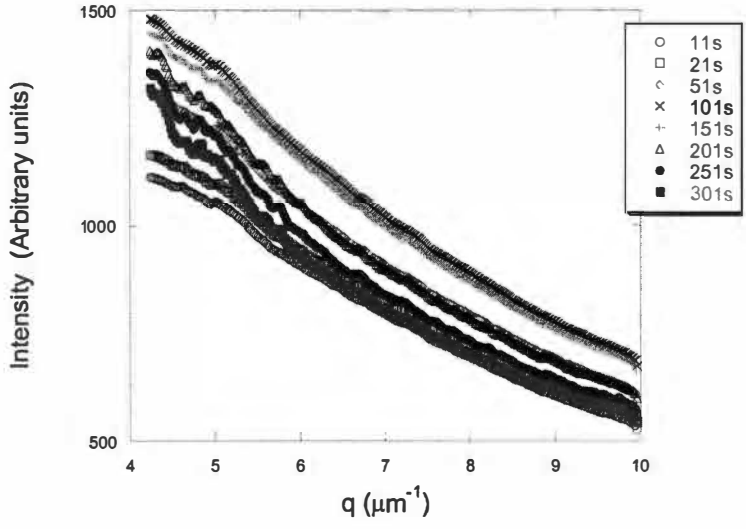


Figure 5.9 Continued. c. 50% E7 58-103s

5.10 a.



5.10 b.

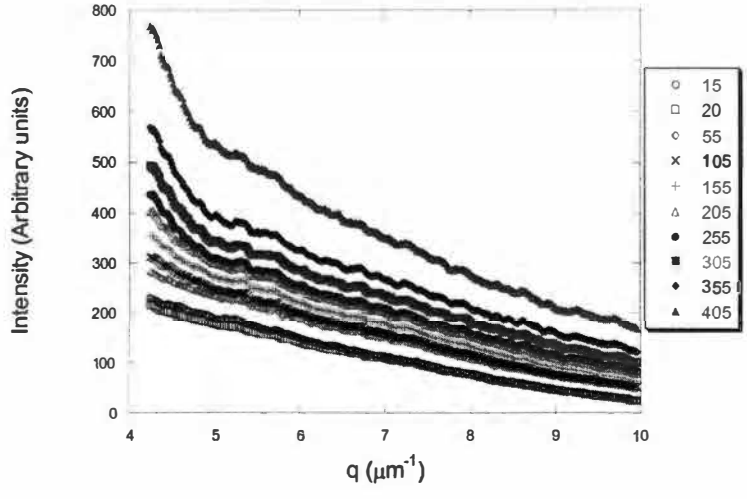


Figure 5.10 Scattering profiles for PDLC syrups cured at 0.693 mW/cm^2. a. 40% E7 11-301s; b. 50% E7 15-405s

11s. The upturn in scattering at lower q also appears at a much earlier time than either the 0.141 mW/cm^2 or 0.214 mW/cm^2 cure intensities. The scattered intensity for all scattering vectors increases with time until 101s after which time the intensity decreases, indicating increased opacity of the sample, until 301s where there is little further change in the scattering. The 50% sample, Fig. 5.10 b., like the 40% sample, exhibit scattering at the earliest stages of the experiment, 15s, as well as an upturn in the forward scattering at 105s. The total intensity continues to grow rapidly, but the scattering profile neither shows the decrease in intensity seen in the 40% sample nor reaches the magnitude in intensity observed in the 0.214 mW/cm^2 experiment.

Analysis of Scattering Profiles: 0.14-0.693 mW/cm^2

The scattering data from all three cure intensities possess common features that are independent of LC content or curing conditions. The first feature is the presence of broad scattering with no discernable maximum. Secondly, the absence of a maximum that grows in intensity and shifts towards lower scattering vectors means the phase separation mechanism can not be verified from these scattering profiles. Lastly, the scattering profiles show sharp upturns in the forward scattering that may indicate scattering from phase-separated LC-rich domains. The presence of broad, featureless scattering profiles implies the formation of a random structure and means that analysis of the data is model-dependent. Since previous studies of the structures of PDLC's that are derived from these syrups show randomly- correlated structures, two different models can be used to analyze the data. If the PDLC has LC domains that are large enough to cause scattering, the Debye-Bueche (DB)[36,95] equation, shown in Equation (E 5.4), describes the scattering behavior. On the other hand, if the phase separation of the LC is occurring

$$I(q) = I(0)/(1 + \xi^2 q^2)^2 \qquad \text{(E 5.4)}$$

but no discrete LC domains have been formed, the scattering originates from concentration fluctuations, and the Orenstein-Zernicke (OZ) equation,[87, 46] see Equation (E 5.5), is used. In both equations the scattered intensity as a function of scattering

$$I(q) = I(0)/(1 + \xi^2 q^2) \qquad \text{(E 5.5)}$$

vector, q,is I(q), I(0) is the scattered intensity at q = 0, and ξ is known as the correlation length of the scattering.

Although the OZ and DB equations seem similar, the scattering behavior that they describe originates from very different sources. The OZ equation is based on a correlation function that assumes the scattering at low q originates from concentration fluctuations typically found in single-phase systems.[46] The DB equation is also derived from a correlation function, but in this particular model, the low q scattering is due to the presence of concentration inhomogeneities[95] or, in the case of the PDLC, phase-separated LC domains. As a result of the different approaches in OZ and DB, the information that is gained from I(0) and ξ in each equation is also quite different. I(0) for the OZ equation is related to the frequency of the concentration fluctuations,[87,46] but in the DB model I(0) is proportional to the relative number of domains[96] that occupy the illuminated volume. Likewise, the correlation lengths give the size of the concentration fluctuations in OZ and that of the domains in DB.

In order to determine the proper analysis to use for the PDLC films, the TRLS experiments are repeated under similar cure conditions (0.11 and 0.29 mW/cm^2) for one of the E7 compositions, 50% in this case. Scattering profiles for the fully cured films are

obtained, and afterwards, the LC is removed from the polymer matrix by immersing the films in methanol. The scattering profiles for 50% E7 PDLC's that have been cured for 2 hours are given in Figure 5.11 along with fits of the data to both DB and OZ equations. From the figure it is evident that both equations provide good fits to the data, however, the two equations yield very different results for both I(0) and ξ. The results from the OZ analysis show that the final value for ξ is around 12 μm for both cure intensities, while the DB analysis yields 260nm for 0.11mW/cm^2 and 230nm for 0.29mW/cm^2. Thus electron microscopy is used to determine the average size of the heterogeneities in the samples to see which analysis is consistent with this direct observation of the resultant morphology.

The first set of HRSEM micrographs for the 0.11 and 0.29 mW/cm^2 experiments can be found in Figures 5.12 a-d and 5.13 a-d. The first micrograph, 5.12 a., shows a film with magnification where the scale bar is 10μm, and 5.12 b. shows the fast Fourier transform (FFT) of the image. The micrograph shows a film with the interconnected, polymer bead[36] morphology that has been shown to be typical in PDLC's formed by floodlit illumination at this LC concentration. The FFT of the micrograph exhibits a completely diffuse pattern that confirms the random distribution consistent with either OZ or DB analysis.[46,93] The next micrograph, 5.12 c., shows the same film at 1μm magnification. The presence of voids in the micrograph indicates that LC domains are being formed during the TRLS experiment. The average size of the voids is determined by taking a cross-section of the image, a typical example is shown in 5.12 d., and

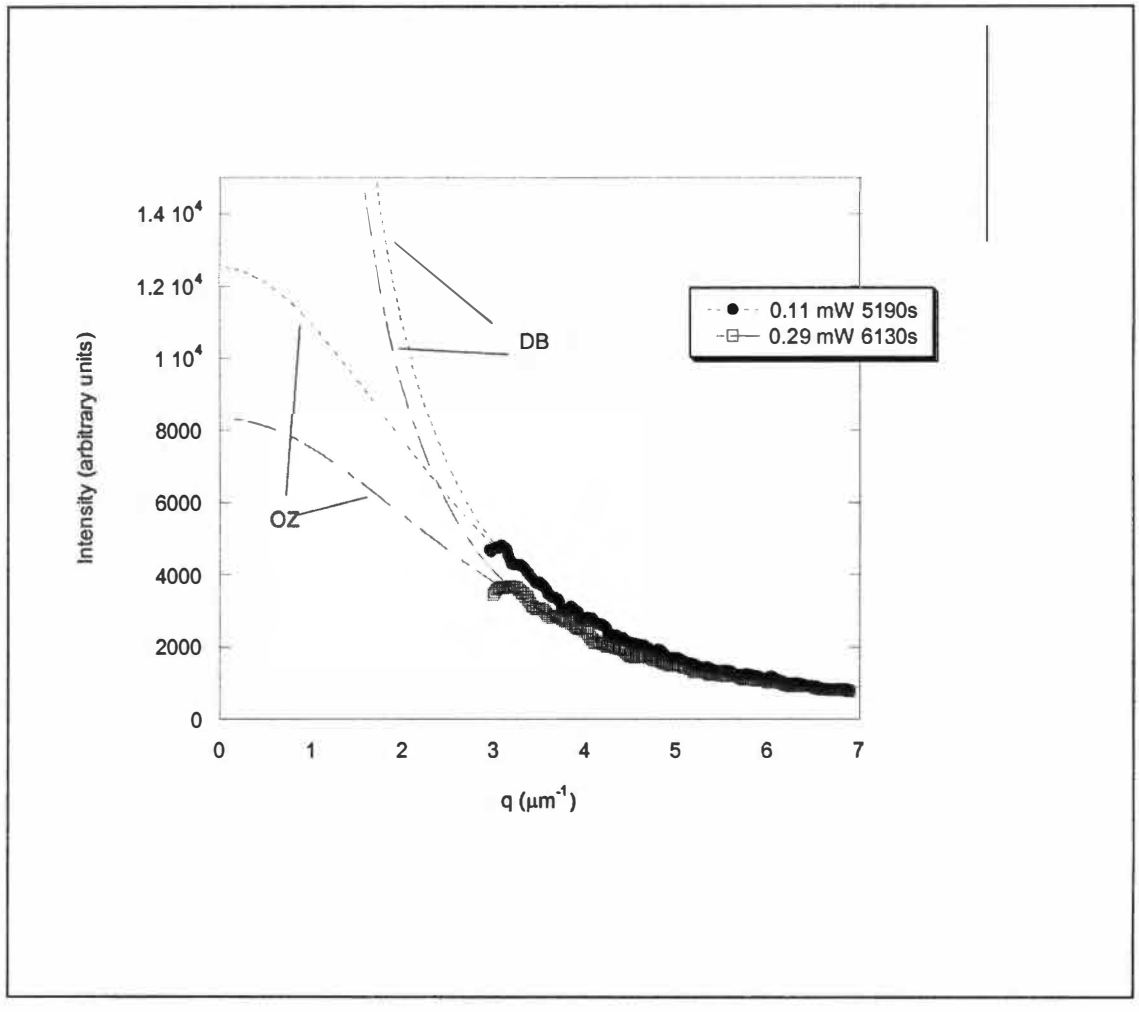
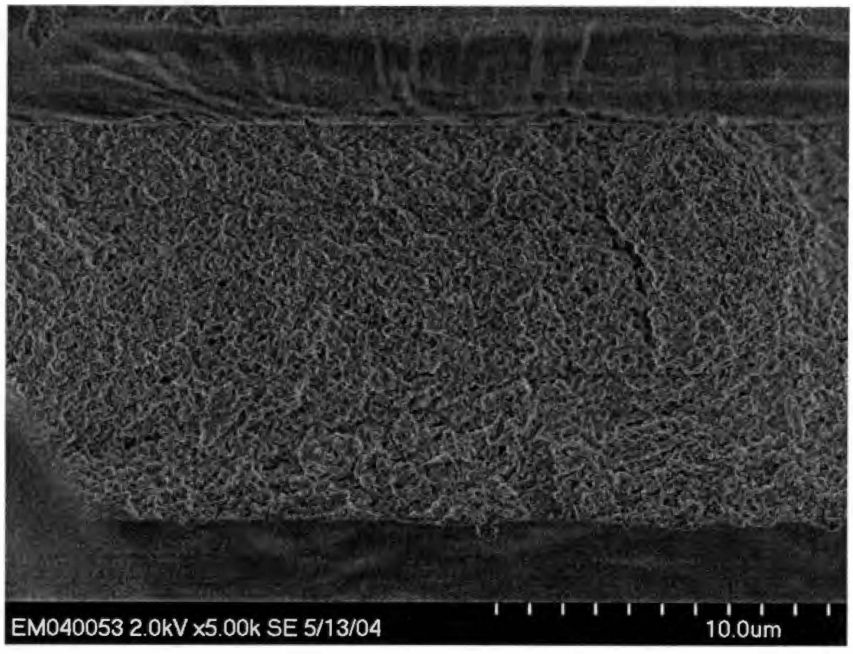


Figure 5.11 Scattering profiles for fully cured 50% E7 PDLC films before LC removal.

5.12 a.



5.12 b.

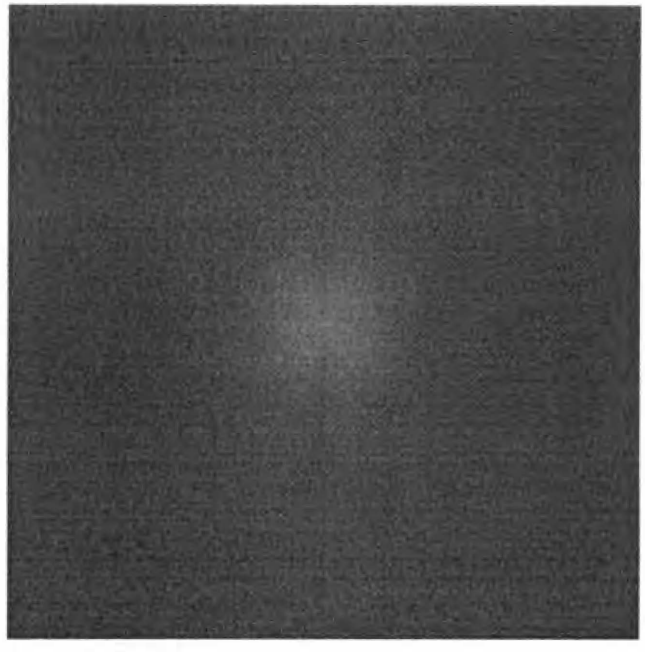
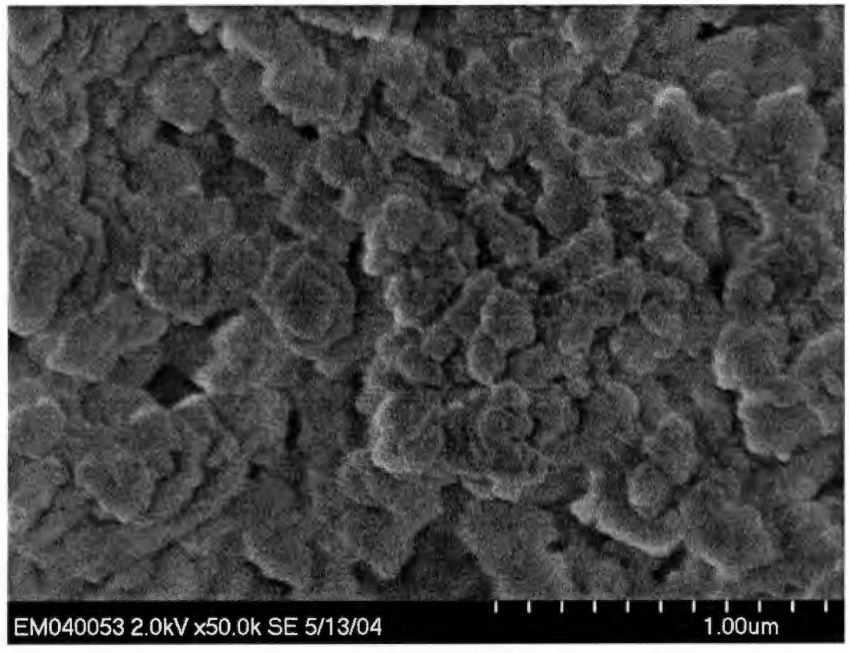


Figure 5.12 HRSEM image of PDLC film cured at 0.11 mW/cm^2 (LC has been removed); a. scale bar 10 μm b. FFT of image in a., indicative of a random network.

5.12 c.



5.12 d.

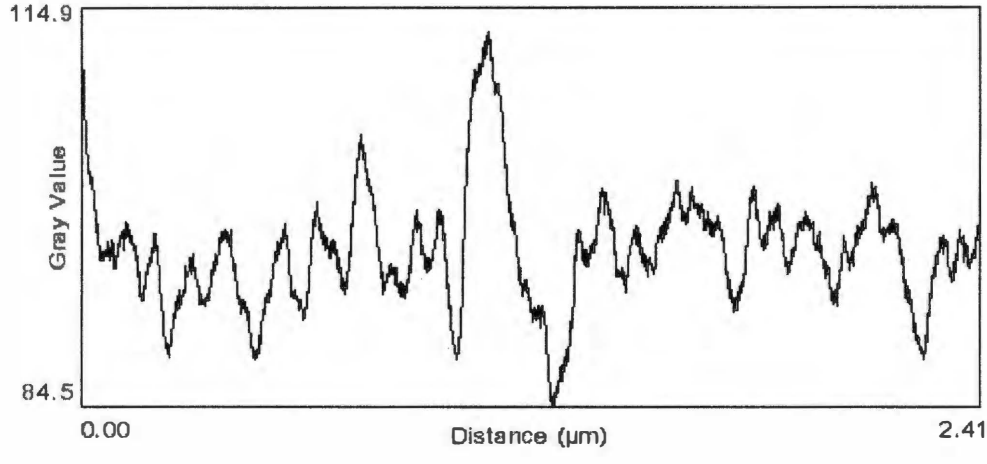
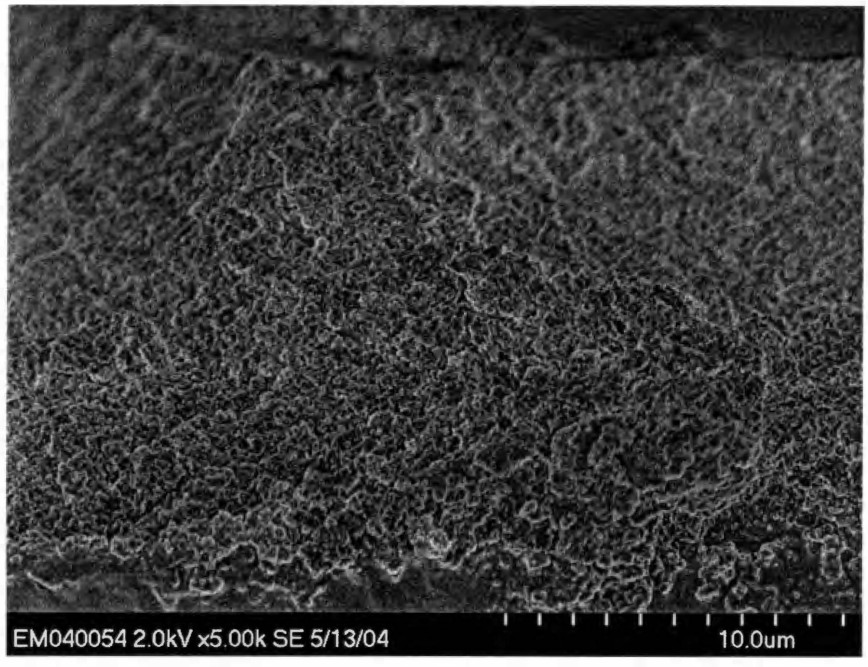


Figure 5.12 Continued. c. HRSEM image of PDLC film depicted in Figure 5.11 at 1µm length scale d. Typical plot profile of image in c., average size of the voids approximately 145 nm

5.13 a.



5.13 b.

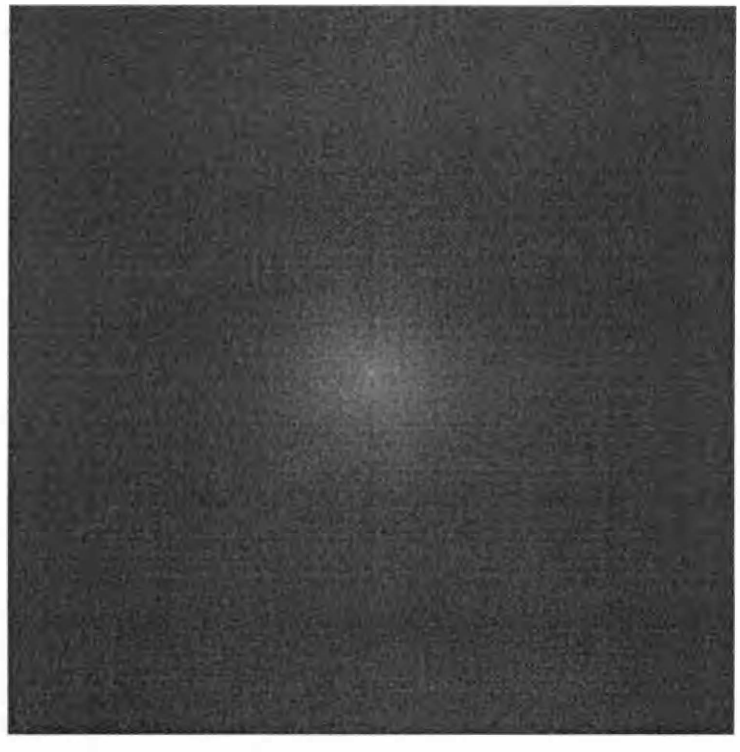
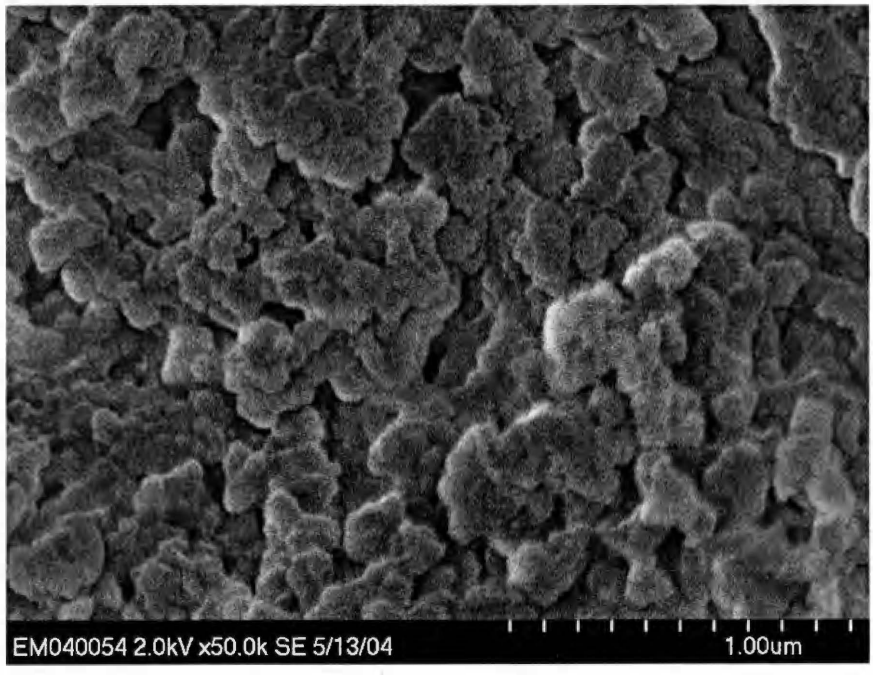


Figure 5.13 HRSEM image of PDLC film cured at 0.29 mW/cm^2 (LC has been removed), a.scale bar 10 μm b. FFT of image in (a.), indicative of a random network.

5.13 c.



5.13 d.

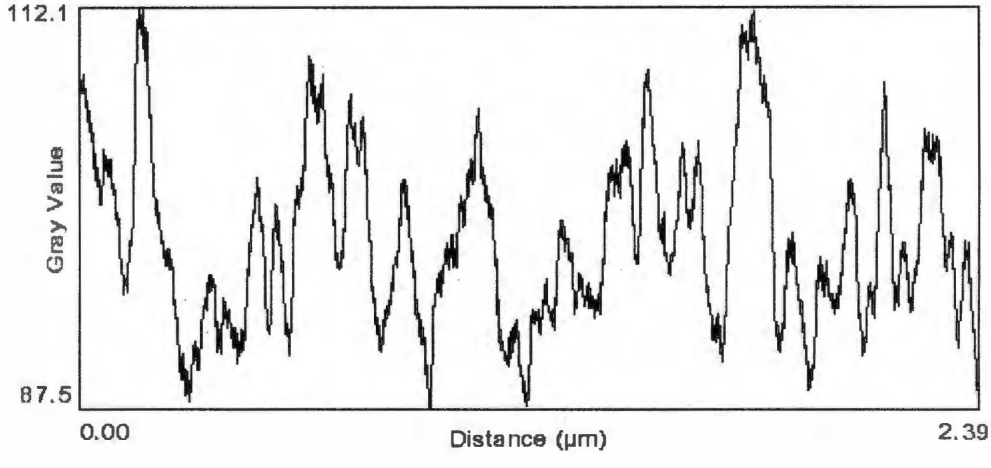


Figure 5.13 Continued. c. HRSEM image of PDLC film depicted in Figure 5.11 at 1µm length scale d. Typical plot profile of image in (c.), average size of the voids approximately 192 nm

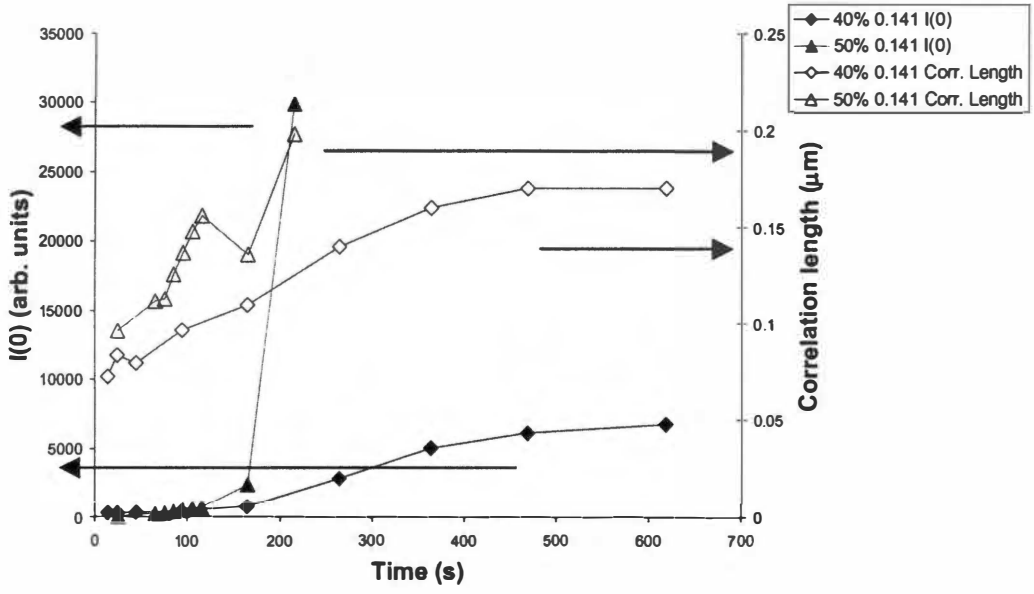
measuring the width of the larger voids, which are on the order of 100nm. The reason for setting the domain size limitation comes from the fact that the smallest length scale probed by the TRLS instrument is on the order of hundreds of nanometers. This process is repeated by taking profiles from different regions of the micrograph, and the average size of the voids is determined to be 145nm.

The HRSEM results for the film cured at 0.29mW/cm^2, 5.13 a-d, also shows the presence of voids, and like the previous set of micrographs, 5.13 a. shows a random, interconnected morphology that is confirmed by the FFT in 5.13 b. However, when the sample is viewed at higher magnification, see 5.13 c., the morphology shows polymer beads that are much rounder and smoother than the previous set of micrographs. This change in morphology suggests that the increased cure intensity produces higher polymer molecular weights at earlier illumination times than samples cured at 0.11mW/cm^2. The average size of the voids is determined by taking the cross-section of 5.13 c., as shown in 5.13 d. The average size of the voids for this experiment is approximately 192 nm. When the average void sizes are compared to the analysis of the scattering data, the DB analysis yields fluctuation sizes that are consistent with the HRSEM results. Therefore, the scattering data for both LC compositions is analyzed using the Debye-Bueche analysis.

The results of the DB analyses of the scattering curves for both LC compositions at all three of the cure intensities are shown in Figure 5.14 a-c. The value of I(0) obtained from the analysis, in arbitrary units on the left axis, and the correlation length, ξ, on the right axis, of the LC domains are plotted as a function of illumination time. The sample that was exposed to the 0.141 mW/cm^2 cure intensity is shown in Figure 5.14 a. for both

LC compositions. In this figure the 40% E7 sample exhibits a slow increase in I(0) with time until leveling off at 370s. The domain size for the 40% sample shows the same growth trend, growing slowly from 70 nm at the start of the experiment and leveling to 170 nm at 370s. For the 50% E7 sample, I(0) begins to grow slowly, but when thesample has been irradiated for 170s, I(0) rises steeply throughout the remainder of the experiment until reaching a final value that is nearly three times greater than the 40% sample. The domain size for the 50% sample at 25s is nearly 100nm and rises quickly to 156nm at 115s. Between 115s and the final time of the experiment, 215s, the size of the domains decreases to 136 nm before rising again to 198 nm. As the cure intensity is increased to 0.214 mW/cm^2, Figure 5.14 b, the 40% sample exhibits a smooth, steady increase in I(0) throughout the experiment that reaches a final intensity nearly three times larger than the result in 5.14 a. The 50% sample also shows a dramatic increase in I(0), attaining a value of almost 40,000 within the first 100s before the detector becomes saturated. The change in the domain sizes for this illumination show similar trends with the 40% steadily increasing from 100 to 200 nm and the 50% sample rapidly growing from 20 to 156 nm. For the highest cure intensity, 0.69 mW/cm^2 in 5.14 c, the DB analysis shows a much different trend from the behavior of the previous two cure intensities. I(0) for 40% shows a rapid increase within the first 100s but levels off quickly to values that are much lower than the previous two intensities. As for the 50% sample, I(0) shows, at first, a very slow increase until 150s followed by rapid growth, but the final intensity, similar to the 40% sample, never reaches the magnitude of the other experiments. Correlation lengths for the 40% sample at this illumination start slightly lower, approximately 70nm, and do not begin to increase until 150s, approaching a maximum of 120nm at full cure. ξ for the

5.14 a.



5.14 b.

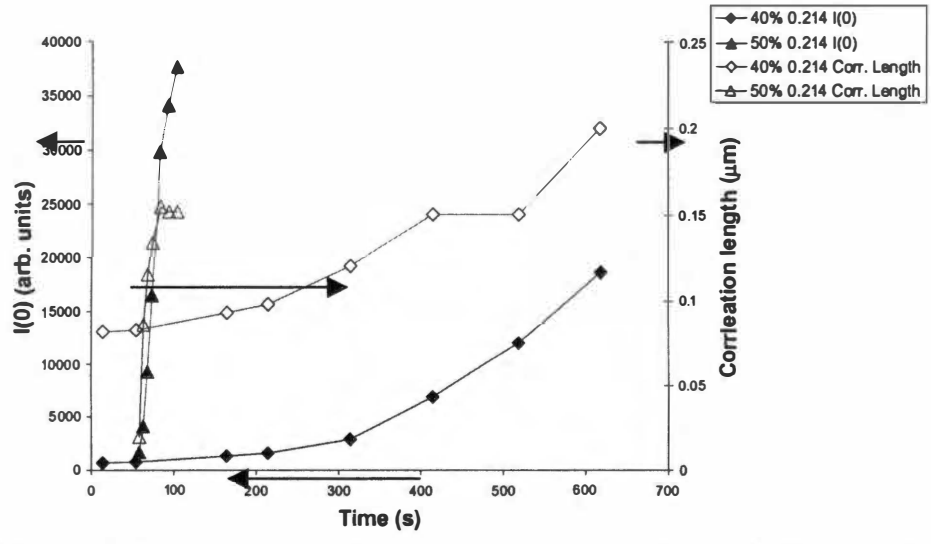


Figure 5.14 Debye-Bueche analysis of scattering data, (◆) 40% E7 I(0), (▲) 50% E7 I(0), (◇) 40% E7 correlation length, (△) 50% E7 correlation length. a. 0.14 mW/cm^2; b. 0.214 mW/cm^2

5.14 c.

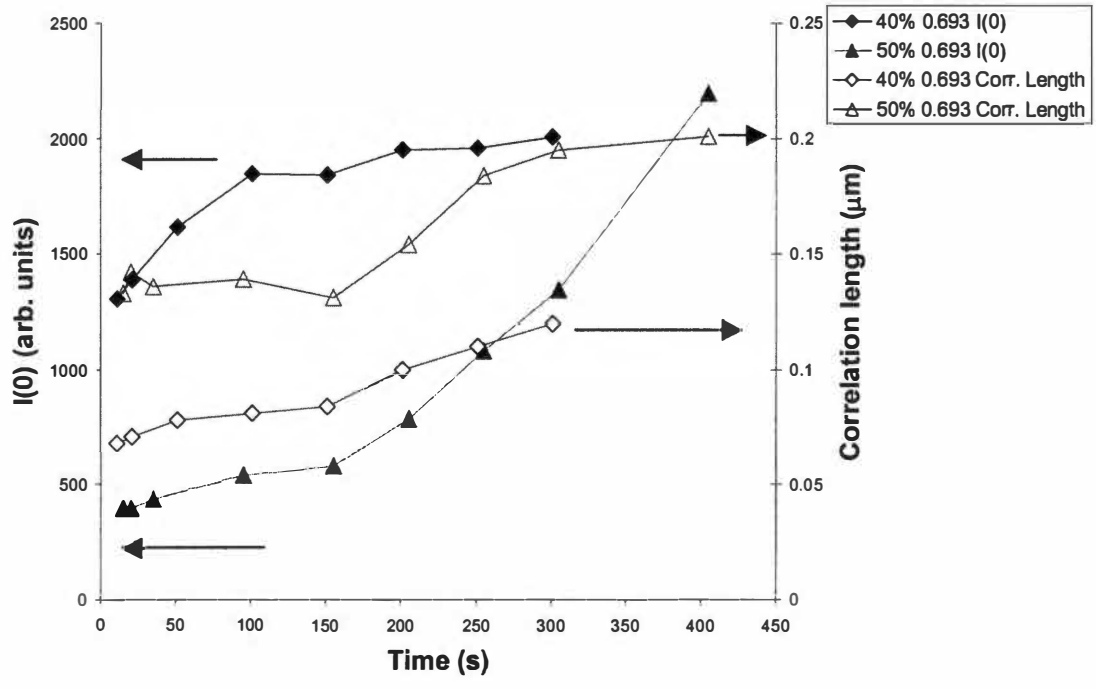


Figure 5.14 Continued. c. 0.693 mW/cm^2

50% E7 sample exhibit domain sizes on the order of 150nm from the start of the experiment until 150s when, like the I(0) for this LC composition, the size increases, and ξ levels off to a maximum value of 200nm.

As the cure intensity is nearly doubled from 0.14 to 0.214 mW/cm^2, the relative number of domains, embodied by I(0), show dramatic changes for both LC compositions. In the 40% sample the number of LC domains goes from the leveling behavior seen at lower illumination intensity to the steady increase seen in 5.14 b. Likewise, the 50% sample also shows an increase in the relative number of domains with an increase in cure intensity. However, as shown by the rapid rise in I(0) within the first 100s, the increase in the relative number of domains is much greater at 0.214 mW/cm^2 cure intensity. As a result, the analysis confirms that raising the cure intensity not only creates more LC droplets but also increases the rate of droplet formation as determined by the absence of the leveling of I(0) in the 40% sample and the rapid rise of I(0) in the 50% sample.

The effect of doubling the cure intensity from 0.14 to 0.214 mW/cm^2 on the growth of the LC domains can also be seen in the changes of the correlation lengths from the DB analysis. The growth rates of the LC domains are estimated by taking the slopes of linear portions of the DB plots in Figures 5.14 a-c. For the 40% sample cured at 0.14 mW/cm^2 intensity the correlation length grows at a rate of approximately 3×10^{-4} μm/s before ξ levels off at 170nm. When the cure intensity for the 40% sample is increased to 0.214 mW/cm^2, the growth rate of ξ during the first 200s, as estimated from the DB analysis in Fig. 5.14 b., is slower, ca. 8×10^{-5} μm/s, before reaching a similar growth rate, ca. 2×10^{-4} μm/s, to the 0.14 mW/cm^2 intensity cure. The similarities in the 40%

ξ growth rates for these two cure intensities are surprising since the increase in cure intensity is expected to increase the growth rate of the LC domains, however, under the 0.214 mW/cm^2 cure intensity, the growth of the domains suggests a continuous increase in the size of the LC domains instead of the leveling off of ξ that is observed in the DB analysis of the 40% samples cured at 0.141 mW/cm^2. The size of the LC domains in the 50% sample exhibit approximate growth rates of 5×10^{-4} μm/s when cured under 0.141 mW/cm^2 illumination and 2.4×10^{-3} μm/s for the 0.214 mW/cm^2 cure, as expected.

At this point a reasonable explanation for the changes in the phase separation kinetics can be found in the competition between the speed of polymer matrix formation and phase separation of the LC from the matrix.[36] Recall from the discussion of PIPS in Chapter1 that the growth of the polymer matrix thrusts the system into a thermodynamically unstable state. As a result, the speed of the polymer matrix formation controls how deeply the system is "quenched" into the unstable state.[96]

Under the lower cure intensity the polymer matrix is produced more slowly than the higher cure intensity, and the slower polymerization results in a shallower quench. In the 40% samples, the shallow quench starts the phase separation, as shown by the growth in the number and size of the LC domains. The shallowness of the quench occurs because the system is being moved more towards equilibrium by the continuously changing thermodynamics[28,29] that asymmetrically shifts the phase diagram, and the number as well as the size of the LC domains begins to level off. In the 50% samples the system remains in the unstable state because of the higher LC content, but the shallow

quench results in the slower growth of the LC domains as compared to the 0.214 mW/cm^2 cure intensity.

Under the higher cure intensity, the systems are thrust into thermodynamic instability more rapidly, and therefore, the system experiences a deeper quench which increases the driving force towards phase separation.[96] The 40% samples show the impact of the deeper quench by the continuous growth of both the number and size of the LC domains. The effect of the deeper quench is also shown by the increase in the relative number of domains in both LC compositions as well as higher growth rates in the 50% samples.

In contrast to the DB analysis for the first two cures, the number of domains for highest cure intensity does not produce the number of domains observed for the other experiments. Similarly, the growth of the LC domains is also slowed by the accelerated polymerization, as shown by the smaller domain sizes in the 40% sample and the early leveling in the 50% sample at this higher illumination. The increased polymerization rate causes a deeper "quench" that speeds up the formation of the LC droplets. However, the presence of fewer LC domains as well as the limits in domain growth indicates that the cross-linking of the polymer matrix quickly arrests phase separation.[30-34,87]

Summary of All Analyses

On a final note, the analyses of the scattering data for all four of the cure intensities illustrate the complex interplay between the movement of the system through phase space and the arresting influence of matrix gelation. For both of the LC compositions that are cured the lowest intensity, 0.0693 mW/cm^2, the formation of the polymer matrix is at its slowest. Under these conditions the quenching of the system into

the thermodynamically unstable state is deep enough to ensure phase separation by spinodal decomposition, but the matrix formation is slow enough that the cross-linking of the matrix does not quickly halt the phase separation of the LC. As the cure intensity is increased to 0.141 mW/cm^2, the system is quenched more rapidly and results in smaller domains than the 0.0693 mW/cm^2 cure. However, the increased polymerization rate pushes the system into a shallower quench. In the 40% samples this causes the leveling in the growth of the LC domains, but the higher LC content of the 50% samples means that the phase separation is not affected by the shift in phase space. As the cure intensity is doubled to 0.214 mW/cm^2, the increased rate of matrix formation results in a deeper initial quench for both LC compositions. The deeper quench increases the rate of LC droplet growth as well as the number of the LC domains in the 50% samples and results in continuous growth of the LC domains in the 40% samples. When the cure intensity is increased to 0.693 mW/cm^2, the quench for both LC compositions is even deeper, however, instead of exhibiting the expected increases in LC domain growth, the rapid cross-linking of the matrix at this stage halts the phase separation.

5.4

Conclusions

Time-resolved light scattering of the polymer dispersed liquid crystals has been successfully employed to study the effect of cure intensity and LC content on the phase separation kinetics of PDLC's formed by PIPS. Of the four cure intensities studied, only the lowest exhibits definite evidence of spinodal decomposition, or SD, as a phase separation mechanism. However, the SD process does not appear to reach the intermediate or late stage, rather, the interconnected structure of early SD is frozen in by

gelation/vitrification of the polymer matrix, as observed from HRSEM images. The effect of LC content on this SD process shows an increase in both the interdomain distance and the mobility of the phase-separating components with increasing LC fraction. Both of these observations are attributed to the diluting effects of the LC which slows the matrix formation and allows for more freedom of movement for both of the components within the system.

As the cure intensity is increased, the phase separation of the LC shows no signs of the spinodal decomposition mechanism, but Debye-Bueche analysis allows for the determination of the relative number and size of the LC domains. The analysis of the first two intermediate cure intensities, 0.14 and 0.21 mW/cm^2, shows rapid increases in the growth of the number and size of the domains for both LC compositions. At this point, these increases can be explained by the rapid "quench" that is caused by faster matrix formation as the cure intensity is increased. For the highest cure intensity, 0.693 mW/cm^2, however, neither the size nor the relative number of the domains ever reaches the magnitude found previously. This result is explained by the gelation/vitrification of the polymer matrix arresting the phase separation of the LC.

CHAPTER 6

Conclusions and Future Work

The work that has been presented in the preceding chapters addresses some of the fundamental questions concerning the phase behavior of PDLC's. Additionally, the results of these studies add valuable insights into the phase separation of LC's from polymer matrices as well as new methods to improve PDLC technologies.

The optical microscopy and DSC studies of 8CB/PMMA blends in Chapter 3 show a limit to the effect of polymer molecular weight on reducing the LC solubility in a hydrocarbon polymer matrix, a limit that is quantified by the Flory-Huggins interaction parameter, χ, as well as the LC solubility limit, β. In addition to these results, the χ-values for blends exhibit scaling behavior as $\chi \sim M_w^{-0.1}$, and the solubility limit results support previous conclusions that the limiting molecular weight behavior can be extended to blends of LC's with other hydrocarbon-based polymer matrices. The effect of these results on PDLC construction is to show that hydrocarbon-based polymers with molecular weights beyond 10^5 g/mol are of limited utility in further reducing the solubility of the LC.

The studies of the LC/copolymer blends have important implications for the control of LC solubility in PDLC's. Through the incorporation of the fluorinated monomer TFEMA, the LC solubility, as expected, is observed to decrease continuously with increasing TFEMA content. This observation is very valuable to the construction of PDLC's because the reduction in LC solubility reduces the loss of the LC, hence, reduces construction costs. In addition to improving the phase separation, the continuous reduction in LC solubility with increasing TFEMA content shows that this parameter can

be "tuned" through the controlled incorporation of fluorinated monomers into the polymer matrix. The change in LC solubility found in these 8CB/copolymer blends is quantified by a total interaction parameter, χ_{total}, which is a function of three separate parameters, $\chi_{8CB\text{-}MMA}$, $\chi_{8CB\text{-}TFEMA}$, and $\chi_{MMA\text{-}TFEMA}$. The successful quantification of the of the LC solubility changes by modified Flory-Huggins theory represents an important modification to the mean-field description of PDLC's and extends the application of this theoretical description to different copolymer/LC blends.

In Chapter 5, the effect of cure intensity and LC content on photo-polymerization induced phase separation, or PIPS, is determined by time-resolved light scattering studies. The result of these studies show evidence of phase separation by spinodal decomposition at the lowest cure intensity that is studied and, under higher illumination intensities, highlight the competition between the driving force for phase separation that is caused by the increasing molecular weight of the matrix during the polymerization process and the cross-linking of the matrix that halts phase separation at longer times. The results show that the size and relative number of the LC domains can be controlled by controlling the intensity of the cure illumination, however, special care should be taken during PDLC construction to balance the competing processes of phase separation and cross-linking of the polymer matrix.

Despite the value of these observations for the future optimization of PDLC devices, some important issues still remain to be addressed. The limiting molecular weight behavior observed in the microscopy results of Chapter 3 represents the first time that such behavior has been observed in PDLC's, and in order to confirm this behavior, similar studies using different hydrocarbon polymer matrices, such as poly(styrene),

should be performed. The scaling of χ as $M_w^{-0.1}$ in the 8CB/PMMA blends suggests that this scaling behavior is caused by packing differences due to differences in molecular structure. However, the confirmation of this scaling behavior is beyond the scope of the present work. One way to verify this is to perform SLCT calculations similar to those of Dudowicz and others, but rather than using the same approach that used to study polymer/polymer blends, the calculations must reflect both the rod-like structure of the LC molecules as well as the molecular structure of the MMA monomers. Another method to determine the exact scaling behavior of χ with molecular weight is to employ scattering techniques such as small-angle x-ray (SAXS) or neutron scattering (SANS). These experimental techniques are able to probe the equilibrium concentration fluctuations of polymer mixtures over very small length scales and, as a result, can be used to determine χ. Therefore, future scattering studies can use the same 8CB/PMMA blends that have been studied in this work to obtain experimentally the scaling behavior of χ, and the results can be compared to the SLCT calculations.

The effect of matrix fluorination on PDLC phase behavior, as studied in Chapter 4, also leaves some issues unaddressed. First, further work is required to determine the effect of the "blockiness" of the copolymers, or in other words, the length and distribution of the fluorinated segments. These studies require block copolymers with controlled sequences of TFEMA which can be synthesized by ATRP. The effect of the microstructure of the new copolymers on the PDLC phase behavior can then be determined using the same techniques as Chapter 4. Another important issue to address is the exact measurement of the individual interaction parameters in this system χ_{8CB-}

$_{MMA}$, $\chi_{8CB\text{-}TFEMA}$, and $\chi_{MMA\text{-}TFEMA}$. While the dependence of χ_{total} on $\chi_{8CB\text{-}MMA}$, $\chi_{8CB\text{-}TFEMA}$, and $\chi_{MMA\text{-}TFEMA}$ in the modified Flory-Huggins theory has been successful in describing the phase behavior as determined from optical microscopy, the interaction parameters, $\chi_{8CB\text{-}MMA}$, $\chi_{8CB\text{-}TFEMA}$, and $\chi_{MMA\text{-}TFEMA}$, that are derived from the experimental results are based on the assumption of $\chi_{8CB\text{-}TFEMA} > \chi_{MMA\text{-}TFEMA} > \chi_{8CB\text{-}MMA}$. Proving the assumption for the interaction parameters requires the experimental determination of each interaction parameter by SAXS or SANS studies.

The final recommendations for future work involve the phase separation kinetics studies in Chapter 5. One of the more recent applications for PDLC's is to construct electro-optical devices that possess LC domains with sizes smaller than 100nm. In order to control the size and distribution of the LC domains at these small length scales, more time-resolved studies are needed of the early stages of the PIPS process, when these small domains are being formed. However, the time-resolved light scattering instrument that is used in our investigation, while well-suited to study structures ranging from hundreds of nanometers to microns, is not capable of capturing the composition fluctuations during the earliest stages of PIPS. Time-resolved x-ray scattering offers a promising technique to study the phase separation behavior at these early times.

BIBLIOGRAPHY

1. http://dom.semi.org/web/wsemi.nsf/webdocs/95237A44B38F076588256A7F006F9F73

2. http://www.findarticles.com/cf_dls/m0FVP/2_262/89435577/p1/article.jhtml

3. Collings, P.J., Patel, J.S.; *Handbook of Liquid Crystal Research*, 1997, Oxford University Press, New York, NY

4. Drazic, P.S.; *Liquid Crystal Dispersions*, 1995, World Scientific Publishing Co., River Edge, NJ

5. Bunning, T.J., Natarajan, L.V., Tondiglia, V.P., Sutherland, R.L.; *Annual Review in Material Science*, **2000**, *30*, 83-115

6. Mucha, M.; *Progress in Polymer Science*, **2003**, *28*, 837-873

7. Jakubiak, R., Bunning, T.J., Vaia, R.A., Natarajan, L.V., Tondiglia, V.P.; *Advanced Materials*, **2003**, *15(3)*, 241-244

8. Klowsowicz, S.J., Zmija, J.; *Molecular Crystals and Liquid Crystals*, **1994**, *249*, 163-169

9. Collings, P.J., Hird, M.; *Introduction to Liquid Crystals: Chemistry and Physics*, 1997, Taylor and Francis Ltd., Bristol, PA

10. DeGennes, P. G. and Prost, J.; *The Physics of Liquid Crystals 2nd Ed.*, 1993, Oxford University Press, New York, NY

11. Collings, P. J.; *Liquid Crystals: Nature's Delicate Phase of Matter*, 1990, Princeton University Press, Princeton, NJ

12. Williams, E.L.; *Liquid Crystals for Electronic Devices*, 1975, Noyes Data Corporation, Park Ridge, NJ

13. Odian, G.; *Principles of Polymerization, 3rd Ed.*, 1991, John Wiley and Sons, Inc., New York, NY

14. Ballauff, M.; *Molecular Crystals and Liquid Crystals*, **1986**, *4(1)*, 15-22

15. Dorgan, J.R.; Soane, D.S.; *Molecular Crystals and Liquid Crystals*, **1990**, *188*, 129-146

16. Hiemenz, P. C.; *Polymer Chemistry: The Basic Concepts*, 1984, Marcel Dekker, Inc., New York, NY

17. Flory, P.J.; *Principles of Polymer Chemistry*, 1953, Cornell University Press, Ithaca, NY

18. Van Dijk, M.A., Wakker, A.; *Polymer Thermodynamics Library-Vol.2: Concepts of Polymer Thermodynamics*, 1997, ChemTec Publishing, Lancaster, PA

19. Ahn, W., Kim, C.Y., Kim, H., Kim,S.C.; *Macromolecules*, **1992**, *25*, 5002-5007

20. Smith, G.W.; Ventouris, G. M.; West, L.; *Molecular Crystals and Liquid Crystals*; **1992**, *213*, 11-30

21. Smith, G.W.; *Molecular Crystals and Liquid Crystals*; **1993**, *225*, 113-130

22. Smith, G.W.; *Molecular Crystals and Liquid Crystals*; **1994**, *241*, 32-53

23. Benmouna, F.; Daoudi, A.; Roussel, F.; Leclerq, L.; Busine, J.; Coqueret, X.; Benmouna, M.; Ewen, B.; Maschke, U.; *Macromolecules*, **2000**, *33*, 960-967

24. Roussel, F.; Buisine, J.; Maschke, U.; Coqueret, X.; Benmouna, F.; *Physical Review E*, Aug. **2000**, *62(2)*, 2310-2316

25. Nauman, E. B., He, D.Q.; *Chemical Engineering Science*, **2001**, *56*, 1999-2018

26. Kim, W.-K., Kyu, T.; *Molecular Crystals and Liquid Crystals*, **1994**, *250*, 131-141

27. Lin, J., Taylor, P.L.; *Molecular Crystals and Liquid Crystals*, **1993**, *237*, 25-31

28. Serbutoviez, C., Kloosterboer, J.G., Boots, H.M.J., Touwslager, F.J.; *Macromolecules*, **1996**, *29*, 7690-7698

29. Boots, H.M.J., Kloosterboer, J.G., Serbutoviez, C., Touwslager, F.J.; *Macromolecules*, **1996**, *29*, 7683-7689

30. Chan, P. K.; Rey, A.D.; *Macromolecules*, **1996**, *29*, 8934-8941

31. Chan, P. K.; Rey, A.D.; *Macromolecules*, **1997**, *30*, 2135-2143

32. Nwabunma, D., Kyu, T.; *Macromolecules*, **1999**, *32*, 664-674

33. Nwabunma, D., Chiu, H., Kyu, T.; *Journal of Chemical Physics*, **2000**, *113(15)*, 6429-6436

34. Kyu, T, Chiu, H.; *Polymer*, **2001**, *42*, 9173-9185

35. Gu, C., Xu, Y., Yisi, L., Pan, J.J., Zhou, F., He, H.; *Optical Materials*, **2003**, *23*, 219-227

36. Vaia, R.A., Tomlin, D.W., Schulte, M.D., Bunning, T.J.; *Polymer*, **2001**, *42*, 1055-1065

37. Nephew, J.B., Nihei, T.C., Carter, S.A.; *Physical Review Letters*, **1998**, *80(15)*, 3276-3279

38. Sawyer, L.C., Grubb, D.T.; *Polymer Microscopy*, **1987**, Chapman and Hall, New York, NY

39. http://www.microscopyu.com

40. http://www.olympusmicro.com/primer

41. Maschke, U., Benmouna, F., Roussel, F., Daoudi, A., Buisine, J.-M., Coqueret, X., Benmouna, M.; *Macromolecular Chemistry and Physics*, **2001**, *202*, 1100-1104

42. Gogibus, N.; Benmouna, F.; Ewen, B.; Pakula, T.; Coqueret, X.; Benmouna, M.; Maschke, U.; *Journal of Polymer Science Part B*, **41**, 39-43

43. http://rsb.info.nih.gov/nih-image/Default.html

44. Skoog, D.A., Holler, F.J., Nieman, T.A.; *Principles of Instrumental Analysis*, 5th Ed., 1998, Saunders College Publishing, Fort Worth, FL

45. Grouenwoud, W.M.; *Characterization of Polymers by Thermal Analysis*, 2001, Elsevier Science B.V., Amsterdam, The Netherlands

46. Brown, W.; Light Scattering: *Principles and Development*, 1996, Oxford University Press Inc., New York, NY

47. Berne, B.J., Pecora, R.; *Dynamic Light Scattering: With Applications to Chemistry, Biology, and Physics*, 1976, Dover Publications Inc., Mineola, NY

48. Maugey, J., Budtova, T., Navard, P.; *The Wiley Polymer Networks Group Review Series*, Vol. 1, **1998**, John Wiley and Sons, Ltd.

49. Kyu, T., Lee, J.-H.; *Physical Review Letters*, **1996**, *76(20)*, 3746-3749

50. Lee, J.C.; *Physical Review E*, **1999**, *60(2)*, 1930-1935

51. Nwabunma, D., Chiu, H., Kyu, T.; *Macromolecules*, **2000**, *33*, 1416-1424

52. Maugey, J., Navard, P.; *Polymer*, **2002**, *43*, 6829-6837

53. Graca, M., Wieczorek, S.A., Holyst, R.; *Macromolecules*, **2003**, *36*, 6903-6913

54. Sato, T., Han, C.C.; *Journal of Chemical Physics*, **1988**, *88(3)*, 2057-2065

55. Matyjaszewski, K.; *Controlled Radical Polymerization*, 1998, American Chemical Society, Washington, DC

56. Wang, J.-S., Matyjaszewski, K.; *Macromolecules*, **1995**, *28*, 7901-7910

57. Perec, V., Barboiu, B.; *Macromolecules*, **1995**, *28*, 7970-7972

58. Eastwood, E.A., Dadmun, M.D.; *Macromolecules*, **2001**, *34*, 740-747

59. Narita, T., Hagiwara, T., Hamana, H., Goto, M.; *Makromoleculaire Chemie*, **1986**, *187*, 731

60. Painter, P.C., Coleman, M.C.; *Fundamentals of Polymer Science*; 1997, Technomics, Lancaster, PA

61. Stroeks, A., Nies, E.; *Macromolecules*, **1990**, *23*, 4092

62. Benmouna, F., Maschke, U., Coqueret, X., Benmouna, M.; *Macromolecular Theory and Simulation*, **2000**, *9*, 215-229

63. Nishi, T.; J. *Macromolecular Science-Physics*, **1980**, *B17(3)*, 517-542

64. Konno, S.; Saeki, S.; Kuwahara, N.; Nakata, M.; Kaneko, M.; *Macromoecules.*, **1975**, *8(6)*, 799-804

65. Koningsveld, R.; Kleintjens, L.A.; *Macromoecules.*, **1971**, *4(5)*, 637-641

66. Beaucage, G.; Stein; R.S.; Koningsveld, R.; *Macromolecules.*, **1993**, *26*, 1603-1608

67. Petri, H.; Schuld, N.; Wolf, B.A.; *Macromolecules*, **1995**, *28*, 4975-4986

68. Schuld, N.; Wolf, B.A.; *Journal of Polymer Science PartB*, **2001**, *39*, 651-662

69. Nishi, T.; J. *Macromolecular Science-Physics*, **1980**, *B17(3)*, 517-542

70. Saeki, S.; Kuwahara, N.; Nakata, M.; Kaneko, M.; *Polymer*, **1975**, *16*, 445

71. Ghelson, M. D.; Rosdale, J. H.; Bates, F. S.; Wignall, G. D.; Hansen, L.; Almdal, K.; *Physical Review Letters*, **1992**, *68(16)*, 2452-2455

72. Sun, Z.; An, L.; Li, H.; Jiang, Z.; Wu, Z.; *Macromolecular Theory and Simulations*, **2001**, *10*, 692-699

73. Konno, S.; Saeki, S.; Kuwahara, N.; Nakata, M.; Kaneko, M.; *Macromoecules.*, **1975**, *8(6)*, 799-804

74. Freed, K.F.; Dudowicz, J.; *Journal of Chemical Physics*, **1992**, *97(3)*, 2105-2109

75. Dudowicz, J.; Freed, K.F.; Douglas, J.F.; *Journal of Chemical Physics*, **2002**, *116(22)*

76. Schulte, M.D.; Clarson, S.J.; Natarajan, L.V.; Tomlin, D.W.; Bunning, T.J.; *Liquid Crystals*, **2000**, *27(4)*, 467-475

77. Schulte, M.D.; Clarson, S. J.; Natarajan, L.V.; Tomlin, D.W.; Bunning, T.J.; *Molecular Crystals and Liquid Crystals*, **2002**, *373*, 155-180

78. DeSarkar, M.; Qi, J.; Crawford, G. P.; *Polymer*, **2002**, 7335-7344

79. Hiyama, T.; *Organofluorine Compounds: Chemistry and Applications*, 2000, Springer-Verlag, New York, NY

80. Yamada, N., Ohnishi, N., Kouzaki, S., Funada, F., Awane, K.; *Japan Display*, **1992**, 695-698

81. Kambour, R. P.; Bendler, J. T.; Bopp, R. P.; *Macromolecules*, **1983**, *16*, 753-757

82. ten Brinke, G.; Karasz, F. E.; MacKnight, W. J.; *Macromolecules*, **1983**, *16*,1827-1832

83. ten Brinke, G.; Karasz, F. E.; *Macromolecules*, **1984**, *17*, 815-820

84. Mugica, A.; Barral, M.; Pomposo, J. A.; Cortazar, M.; *Acta Polymerica*, **1999**, *50*, 304-311

85. Hamming, R.W.; *Numerical Methods for Scientists and Engineers, 2nd Ed.*, 1986, Dover Publications, Inc., Mineola, NY

86. Kyu, T.; Shen, C.; Chiu, H.-W.; *Molecular Crystals and Liquid Crystals*, **1996**, *287*, 27

87. Pogue, R.T., Natarajan, L.V., Siwecki, S.A., Tondiglia, V.P., Sutherland, R.L., Bunning, T.J.; *Polymer*, **2000**, *41*, 733-741

88. Mishra, M. K., Yagci, Y.; *Handbook of Radical Vinyl Polymerization*, 1998, Marcel Dekker, Inc., New York

89. Maugey, J., Van Nuland, T., Navard, P.; *Polymer*, **2001**, *42*, 4353-4366

90. Matsuyama, H., Kudari, S., Kiyofuji, H., Kitamura, Y.; *Journal of Applied Polymer Science*, **2000**, *76*, 1028-1036

91. Lauger, J., Lay, R., Maas, S., Gronski, W.; *Macromolecules*, **1995**, *28*, 7010-7015

92. Fujita, K., Kyu, T.; *Macromolecules*, **1996**, *29*, 91-96

93. Edel, V.; *Macromolecules*, **1995**, *28*, 6219-6228

94. Furukawa, H.; *Advances in Physics*, **1985**, *34(6)*, 703-750

95. Debye, P., Bueche, A.M.; *Journal of Applied Physics*, **1949**, *20*, 518-525

96. Brown, W.; Light Scattering: *Principles and Development*, 1996, Oxford University Press Inc., New York, NY

97. Alig, I., Rullmann, M., Holst, M., Xu, J.; *Macromolecular Symposia*, **2003**, *198*, 245-257

Vita

Nathan Joseph Crawford was born in Baldwyn, MS on October 4, 1974. He graduated from Booneville High School in 1993 and went on to study chemistry at Mississippi State University. After receiving his BS in 1998, he was accepted into the graduate program at the University of Tennessee where he pursued a doctorate in chemistry with an emphasis in polymer chemistry. He successfully defended his dissertation on July 1, 2005.

Nathan is currently engaged in post-doctoral work involving high-performance lubricants at the University of Tennessee. Afterwards, he hopes to establish either an active research program for undergraduates or a research and development role in industry.

4535 0545 14
11/09/05 MAB